Atomistic Mechanisms for Viscoelastic Damping in Inorganic Solids

by

Raghavan Ranganathan

A Thesis Submitted to the Graduate

Faculty of Rensselaer Polytechnic Institute
in Partial Fulfillment of the
Requirements for the degree of
DOCTOR OF PHILOSOPHY

Major Subject: Materials Science and Engineering

Approved by the Examining Committee:
Pawel Keblinski, Thesis Adviser
Rahmi Ozisik, Member
Yunfeng Shi, Member
Chang Ryu, Member

Rensselaer Polytechnic Institute Troy, New York

July, 2016 (For Graduation August 2016)

© Copyright 2016 by Raghavan Ranganathan All Rights Reserved

CONTENTS

LI	ST OF	TABL	ES	vi
LI	ST OF	FIGU	RES	vii
ΑC	CKNO	WLED	GMENT	xii
ΑF	BSTRA	ACT		xiii
1.	Introduction			
	1.1	Chara	cteristics of viscoelasticity	1
	1.2	Tradit	ional spring-dashpot models for viscoelasticity	3
	1.3	Freque	ency-dependent dynamic moduli	4
	1.4	Visco	elastic damping in materials: some perspectives	5
		1.4.1	Damping in hard materials	7
	1.5	Object	tives	8
2.	Characterizing viscoelasticity via oscillatory shear deformation: Overview of experiments and simulation methodology			
	2.1	Dynar	nic Mechanical Analysis experiments	9
	2.2	Simul	ation protocol: Atomistic mechanisms for viscoelasticity	10
		2.2.1	Molecular dynamics simulations	11
		2.2.2	Oscillatory shear deformation	11
		2.2.3	Simulation details	13
	2.3	Theore	etical considerations	14
		2.3.1	High-frequency damping: role of vibrational modes	14
		2.3.2	Heat dissipation during shear	15
3.	Visco	oelastic	damping in crystalline composites	17
	3.1	Introduction		
	3.2	Model structures and simulation details		
		3.2.1	Model structures	19
	3.3	Result	es and discussion	22

		3.3.1	Vibrational analysis	. 22
		3.3.2	Local strain distribution	. 23
		3.3.3	Role of composite microstructure and shear frequency on damping	. 24
		3.3.4	Viscoelastic damping in crystalline superlattice structures	. 32
	3.4	Summ	ary and conclusions	. 33
4.	Frequ	uency-d	lependent mechanisms for damping in alloys	. 35
	4.1	Introd	uction	. 35
	4.2	Model	structures and methodology	. 36
		4.2.1	MD Model and structures	. 36
		4.2.2	Methodology	. 37
	4.3	Charac	cterization of model structures	. 39
		4.3.1	Structural characterization of glass	. 39
		4.3.2	Melting points and glass transition temperature	. 40
		4.3.3	Elastic limit for the ordered, random and glassy alloys	. 41
	4.4	Result	s and discussion	. 42
		4.4.1	Frequency-dependence of damping	. 42
	4.5	Summ	ary	. 50
5.	Com	monalit	ies in frequency-dependent viscoelastic damping in glasses	. 52
	5.1	Introd	uction	. 52
	5.2	Simula	ation methodology and model structures	. 54
		5.2.1	Model structures	. 55
	5.3	Damp	ing in BMG	. 57
		5.3.1	Frequency-dependent loss moduli	. 57
		5.3.2	Dependence of damping on number of shear cycles	. 58
		5.3.3	Effect of shear amplitude	. 60
		5.3.4	Effect of shear temperature	. 61
	5.4	Comm	nonality in damping mechanisms in glasses	. 62

		5.4.1	Role of vibrational coupling in damping	64
		5.4.2	Low-frequency damping and structural relaxation	65
	5.5	Summ	ary and Conclusions	68
6.	Sum	mary, p	erspectives and future work	69
	6.1	Summ	ary	69
	6.2	Perspe	ectives and future work	71
		6.2.1	Stiffening in polymer nanocomposites	72
RE	EFERI	ENCES		76

LIST OF TABLES

Table 5.1: Simulation details and material properties for the glass models studied....... 56

LIST OF FIGURES

Figure 1.1: Schematic for stress (σ) – strain (ϵ) relation under the application of cyclic
deformation for (a) ideal elastic material and (b) viscoelastic material exhibiting
hysteresis
Figure 1.2: Spring-dashpot models for viscoelasticity. (a) Maxwell model, (b) Kelvin-
Voigt model and (c) standard linear solid model
Figure 1.3: Schematic for variation of viscoelastic characteristics (storage modulus (G') ,
loss modulus (G'') and $\tan \delta$ with respect to shear frequency (ω)). Figure adapted from
Ref. [22]5
Figure 1.4: Comparison of stiffness (Young's Modulus, E) and $tan \delta$ for a wide range of
materials with contrasting properties. Damping is maximized for materials with higher
stiffness and higher $\tan\delta$ as shown in top right corner for certain hard materials. Figure
adapted from Ref. [31]6
Figure 2.1: Schematic of the Dynamic Mechanical Analyzer. Right panel shows schematic
of phase lag between measured force and displacement (or alternately, between stress and
strain) [45]
Figure 2.2: Schematic showing deformation of a cubic box (initial) by the application of
a shear strain. The magnitude of strain is $\gamma = \Delta x/y$
Figure 2.3: Flowchart for computing the complex shear modulus from the stress-strain
profile
Figure 2.4: Sample result for relation between applied shear strain (shown by blue circles)
and the resultant shear stress (green) during oscillatory shear deformation of a crystalline
composite (shown in inset). Stress data have been averaged over 5 shear cycles 13
Figure 3.1: Snapshots of composite systems containing phases that have a stiffness
contrast. (a) Spherical inclusion of stiff phase. (b) Superlattice structure consisting of 5
layers of A - B superlattice layers. Red atoms correspond to the soft crystalline component
and blue, to the stiff component
Figure 3.2: Estimation of viscoelasticity from averaged stress-strain curves during
oscillatory shear deformation. Shear strain (γ_{xy}) is the input and shear stress (τ_{xy}) is the
output. Panels (a) and (c) are for homogeneous soft and stiff phases respectively that

exhibit negligible phase difference. Panel (b) is for a composite with the volume fraction
of stiff phase, $\varphi \sim 0.4$, exhibiting significant phase shift and thus, a large loss modulus.
Side views in panel (a) show the zero-strain and maximum strain configurations during
the shear cycle
Figure 3.3: Variation of mode-dependent Grüneisen parameters for various composites,
ranging from $\varphi = 0$ (fully soft) to $\varphi = 1$ (fully stiff) for a system size of $L = 7$ unit cells.
Figure 3.4: Spatial strain profiles for both the soft and stiff phases during one-quarter cycle
of shear (till maximum amplitude in sinusoidal shear is reached). System size is $L=25$
unit cells. The soft phase undergoes shear strains much larger than the stiff phase 24
Figure 3.5: Volume-fraction-sweep simulations showing variation of loss modulus as a
function of volume fraction of the spherical inclusion. The two sets of data represent the
arrangement of the phases (the inclusion being either soft or stiff). The shear frequency is
fixed at 0.33 THz. 26
Figure 3.6: Comparison of loss modulus (G'') calculated from MD simulations for LJ
composite with the upper (G_U) and lower (G_L) bounds from Hashin-Shtrikman theory.
System size is $L = 7$ unit cells and shear frequency is $f = 0.33$ THz. The microstructure at
maximum damping volume fraction is shown in inset
Figure 3.7: Variation of loss modulus with stiffness of the stiff phase. The relative stiffness
is represented as the ratio of ε_{stiff} to ε_{soft}
Figure 3.8: Frequency-sweep simulations for composite with volume fraction of stiff
phase, $\varphi \sim 0.5$ for the base composite of size $L=7$ unit cells (red circles) and the base
structure replicated twice ($L = 14$ unit cells) and thrice ($L = 21$ unit cells) along x, y and z
axes (green triangles). The atomic snapshots for these structures are shown as insets 30
Figure 3.9: (a) Frequency-sweep simulations depicting variation of loss modulus with
frequency for various system sizes from $L=7$ unit cells to $L=25$ unit cells, with the
volume fraction of stiff phase, $\varphi \sim 0.48$. The homogeneous phases ($\varphi = 0$ and $\varphi = 1$) which
exhibit negligible loss moduli are also shown for comparison. (b) Variation of peak loss
frequency with inverse of simulation cell length as outlined in panel (a)
Figure 3.10: (a) Frequency-sweep simulations for superlattice structures composed of soft
and stiff phases, for various widths of the superlattice spacing. (b) Variation of the two

peak loss frequencies (the high and low-frequency peaks) as obtained in panel (a), with
inverse of superlattice width
Figure 4.1: Averaged shear stress, τ_{xy} (solid, colored lines) and shear strain, γ_{xy} (dotted
line) profiles for shear at frequency, $f \sim 3.86$ THz for ordered, random and glassy
structures. Stress data for the three structures have been normalized to show the effect of
phase shift (indicated) clearly. (b) Atomistic snapshots of the side view of a small section
of system size (~3.6 nm cross-sectional length) for the three structures
Figure 4.2: Pair correlation function for the glass model used in this work. Nearly identical
plots at the beginning and end of a long NVE simulation ($t = 11 \text{ ns}$) indicate that the glass
is stable
Figure 4.3: (a) Variation of potential energy with temperature during slow melting of
ordered and random alloys. (b) Variation of volume with temperature during quenching
of melt. Glass transition temperature is estimated to be 990 K
Figure 4.4: Shear-stress-shear strain plots for ordered, random and glass structures to
determine the elastic limit
Figure 4.5: (a) Frequency-sweep simulations showing the variation of loss modulus for
ordered, random and glass structures. (b) Same data as in panel (a) but in a log-log scale,
depicting power-law scaling between loss modulus and frequency. Power-law scaling
holds for two decades of frequency for glass, and more than three decades in frequency
for random and ordered alloys. 42
Figure 4.6: (a) Mode-dependent shear Grüneisen parameter (γ_{I2}) for ordered, random and
glass computed for a system size of 864 atoms (box size $\sim\!24$ Å). Random alloy and glass
have γ_{12} that are two to four orders of magnitude larger than ordered structure, as seen
from the inset which shows the data plotted on a logarithmic scale. (b) Vibrational density
of states for the three structures
Figure 4.7: Evolution of cluster size distribution at the end of five cycles of shear of glass,
for three shear frequencies in the low frequency regime. Cluster size (y-axis) is the number
of atoms forming the soft-spot and the cluster number (x-axis) is just an index of each
cluster sorted by ascending order of cluster sizes. Also shown are snapshots of atomic
regions forming the clusters, color-coded according to their atomic displacement with

respect to the initial, undeformed state. Snapshots are generated using the OVITO
visualization tool [103]
Figure 4.8: Evolution of cluster sizes for oscillatory shear simulations run for a constant
time (about 11 ns) instead of constant number of cycles as shown in Figure 4.7. (a)
Distribution of cluster sizes for various frequencies for a single glass sample. (b) Variation
of average cluster size and percentage of atoms that contribute to irreversibly deformed
clusters with frequency. The corresponding average size and deformed volume for the "no
shear" case are indicated by dashed lines, with the range of error bars depicted by
transparent colored bands
Figure 4.9: Relaxation of normalized shear stress, τ_{xy} starting from an initially stressed
state, for the three systems considered (ordered, disordered and glass)
Figure 4.10: Variation of deformation volume as a function of time, for various strain rates
during constant-rate shear deformation. The maximum shear strain for each case is 0.1.
Also shown in black is the case for "no shear". The strain at which the four lowest
frequencies depart from the curve for "no shear" (indicated by red circles) are plotted in
the inset. Data are averaged over 5 independent samples
Figure 5.1: Typical stress-strain response for model Cu-Zr bulk-metallic glass at (a) $f = 2$
THz, showing a large phase difference, and correspondingly, high loss modulus, and (b) f
$= 0.02 \ \mathrm{THz}$, showing low phase difference and low loss modulus. The peak shear modulus
is also noted
Figure 5.2: Frequency-sweep simulations depicting the variation of loss modulus with
shear frequency for the Cu-Zr BMG system. Response for four different quench rates are
shown. The characteristic peak in the high-frequency regime overlap for all quench rates.
Low-frequency damping is affected by the quench rate, with larger quench rates resulting
in larger damping. Inset shows the portion of the low-frequency regime magnified 58
Figure 5.3: Effect of aging on the computed loss modulus for glasses quenched at various
rates. Aging in glass leads to estimated properties that are dependent on the number of
shear cycles; this is effect is probed by varying the number of shear cycles (N_{cycles}) for
each quench rate. Shown in (a) and (b) are data for two widely different shear frequencies
(f = 0.5 THz and f = 0.5 GHz respectively). Simulations performed under NVT conditions

at a temperature of 300 K. The quench rate used for the bulk of the analysis pertaining to
the BMG, namely $Q = 0.85$ K/ps shows fairly cycle-independent damping
Figure 5.4: Effect of shear strain amplitude on viscoelastic response in BMG. Loss
modulus is estimated for four different shear frequencies spanning four orders of
magnitude. Significant non-linearity in the response is observed at strain amplitudes, γ_{xy}
larger than about 0.04 (or 4%)
Figure 5.5: Frequency-sweep simulations to study the effect of shear temperature on
damping in BMG. The maximum temperature (800 K) is just below the T_g for the BMG,
which is ~815 K
Figure 5.6: Frequency-sweep simulations for the five glass structures considered in this
work. For each glass, we show the dependence of loss modulus (normalized by the
maximum in G'') as a function of shear frequency. All glasses show a characteristic peak
in the high-frequency regime and a nearly-invariant, finite damping in the low-frequency
regime (See inset for the magnified portion of the low-frequency regime). Stiffer glasses
such as a-Si and Silica exhibit larger absolute G'' in the high-frequency regime and a
smaller, albeit non-vanishing normalized G'' in the low-frequency regime
Figure 5.7: Correlation between the average frequency obtained from vibrational Density
of states (DOS) for each glass, and the peak position in the frequency-dependent loss
modulus as obtained in Figure 5.6.
Figure 5.8: Characterization of clusters ("soft spots") formed during constant-time
oscillatory shear simulations for various glasses, as a function of shear frequency. The
total simulation time at each frequency, for each glass is 50 ns. (a) Average cluster sizes
at the end of 50 ns of oscillatory shear. (b) The total volume fraction of irreversibly
deformed clusters at the end of shear. The general trend of increasing cluster size and
volume with decreasing frequency is evident
Figure 6.1: Variation of storage modulus with shear frequency for "collapsed" and
"stretched" states for the nanocomposite system. Also shown for reference, is the modulus
for the pure low- T_g polymer

ACKNOWLEDGMENT

This amazing journey of five years has been possible only with the continued support, guidance and motivation from a great number of individuals.

First and foremost, I would like to thank my advisor, Prof. Pawel Keblinski for being an incredible mentor, teacher and guide through all walks of my Ph.D. His keen and incisive insights, along with visionary guidance and constant motivation have helped me have an enriching research experience.

It has been a pleasure to work with Prof. Rahmi Ozisik and Prof. Yunfeng Shi who have provided several valuable suggestions on multiple projects in this thesis. I have enjoyed many stimulating discussions on multiple challenges along the way. I thank Prof. Chang Ryu for serving on my doctoral committee and for valuable suggestions.

I thank members of the Keblinski research group for all the help and guidance over the years. Dr. Kiran Sasikumar has been a great friend and guide especially in the initial years of my Ph.D. I have also benefitted tremendously from interactions with Dr. William Evans, Dr. Meng Shen, Dr. Zhi Liang, Wei Peng and Jihui Nie.

I have had the good fortune of spending two semesters working with Dr. Srujan Rokkam and Dr. Tapan Desai at Advanced Cooling Technologies, Inc (Pennsylvania) as part of the graduate co-op program. I have learnt a great deal both professionally and personally during my stint there, and they have been amazing mentors and friends!

The Materials Science Department at Rensselaer has been my second home during my exploits. I thank the numerous faculty members and staff for all their support, both academically and otherwise. I also acknowledge the financial support by U.S. Air Force Office of Scientific Research and the National Science Foundation.

Many special friends have been a constant source of motivation for me over the years. Special thanks to my roommates, Shravan, Sriram and Amar for all the fun times! I thank my close friends Satyavrata, Karthik, Karthikeyan, Aditya, Jayanth, Arun, and Sivaraman for many unforgettable memories. I thank Karthik, Karthikeyan Aditya and Shravan for valuable suggestions on the thesis.

The emotional support and love shown by my parents, grandparents and sister have been an invaluable source of inspiration to keep me going. I am forever indebted to them.

To my amazing parents, Latha and Ranganathan, I dedicate this thesis.

ABSTRACT

Viscoelasticity, a ubiquitous material property, can be tuned to engineer a wide range of fascinating applications such as mechanical dampers, artificial tissues, functional foams and optoelectronics, among others. Traditionally, soft matter such as polymers and polymer composites have been used extensively for viscoelastic damping applications, owing to the inherent viscous nature of interactions between polymer chains. Although this leads to good damping characteristics, the stiffness in these materials is low, which in turn leads to limitations. In this context, hard inorganic materials and composites are promising candidates for enhanced damping, owing to their large stiffness and, in some cases large loss modulus. Viscoelasticity in these materials has been relatively unexplored and atomistic mechanisms responsible for damping are not apparent. Therefore, the overarching goal of this work is to understand mechanisms for viscoelastic damping in various classes of inorganic composites and alloys at an atomistic level from molecular dynamics simulations.

We show that oscillatory shear deformation serves as a powerful probe to explain mechanisms for exceptional damping in hitherto unexplored systems. The first class of inorganic materials consists of crystalline phases of a stiff inclusion in a soft matrix. The two crystals within the composite, namely the soft and a stiff phase, individually show a highly elastic behavior and a very small loss modulus. On the other hand, a composite with the two phases is seen to exhibit damping that is about 20 times larger than predicted theoretical bounds. The primary reason for the damping is due to large anharmonicity in phonon-phonon coupling, resulting from the composite microstructure. A concomitant effect is the distribution of shear strain, which is observed to be highly inhomogeneous and mostly concentrated in the soft phase. Interestingly, the shear frequency at which the damping is greatest is observed to scale with the microstructural length-scale of the composite. The second class of materials consist of structurally heterogeneous binary alloys that are either ordered, random or glassy. Vastly different mechanisms for viscoelastic damping arise for the three structures – random alloy and glass are observed to exhibit significant damping owing to large anharmonicity in the coupling between vibrational modes, which is a direct consequence of the chemical heterogeneity. Additionally, at low

shear frequencies, glass exhibits significant long-time scale structural relaxation that results in persistent damping over a large range of frequencies. Finally, a critical analysis of various factors that affect damping in inorganic glasses is made. We show that damping in glasses exhibits a striking commonality – at high frequencies, vibrational anharmonicity leads to a peak in damping for all glasses commensurate with the range of vibrational frequencies of the glass; at intermediate and low frequencies, structural relaxation leads to persistent, nearly-constant damping.

The frequency-dependent damping mechanisms and structure-property relations observed with respect to damping are expected to enable the design of novel structures with favorable damping characteristics.

1. Introduction

The field of viscoelasticity has its origin in the development of the theory of elasticity propounded by Robert Hooke in the late 17th century and the study of shear forces in liquids by Newton published in his work *Principia* back in 1687 [1]. The term viscoelastic is a portmanteau of "viscous" and "elastic" meaning a material, under some form of deformation exhibits both viscous character that contributes to a "lossy" behavior, dissipating energy and an elastic character that stores energy as recoverable elastic energy.

Viscoelasticity, or rheology, of soft matter has been studied extensively for many decades [2]–[5]. Although these materials are inherently highly viscous in nature, the evergrowing need for high-performance materials for viscoelastic damping applications has mandated the use of hard inorganic solids which simultaneously show significant viscous and elastic character. The focus of this thesis is to establish structure-property relations and atomistic mechanisms for damping in various hard inorganic materials using molecular dynamics shear simulations. This knowledge is expected to pave the way for engineering novel materials with optimum damping characteristics.

This introductory chapter is organized as follows. In Section. 1.1, an overview of various characteristics of viscoelasticity is presented. In Sec. 1.2, traditional models to describe viscoelasticity are discussed briefly. Characterizing the frequency-dependent loss modulus, the most direct metric for damping is discussed in Sec. 1.3. In Sec. 1.4, several perspectives on damping in soft and hard materials is presented. Finally, Sec. 1.5 discusses the primary objectives of this thesis.

1.1 Characteristics of viscoelasticity

Three common phenomena are typically ascribed to viscoelastic behavior: (a) creep, (b) stress relaxation and (c) dynamic (cyclic) dissipative deformation. Creep leads to an

Portions of this chapter previously appeared as: (a) R. Ranganathan, R. Ozisik and P. Keblinski, "Viscoelastic damping in crystalline composites: A molecular dynamics study", Composites Part B 93, 273 (2016), and (b) R. Ranganathan, Y. Shi and P. Keblinski, "Commonalities in frequency-dependent viscoelastic damping in glasses", unpublished.

increase in the strain in the system as a function of time, at constant applied stress. Stress relaxation involves a continuous decrease in stress when the material is held at constant strain. The third phenomenon, namely dynamic or cyclic loading, leads to the damping phenomenon that is the focus of this work.

Viscoelastic materials, when deformed cyclically, lead to a hysteresis between the stress and strain, as opposed to an ideal elastic material, where this is absent (see Figure 1.1). The area under the stress-strain curve corresponds to the total energy that is dissipated as heat. This "lossy" or dissipative behavior exhibited by the viscous component of the material is an important property responsible for mechanical damping in a vast number of applications. Viscoelasticity can be exploited to synthesize materials with exceptional damping properties. Notably, polymer composites have been designed for damping and noise reduction in automobiles and airplanes [6], conferring structural stability during wind and earthquake induced vibrations [7], and mechanical damping in a number of applications [8]–[12]. Versatility in tuning viscoelastic properties from a purely viscous to a purely elastic behavior has enabled a wide range of engineering applications such as artificial tissues [13], functional foams [14], optoelectronics [15] among a slew of structural and mechanical applications [16].

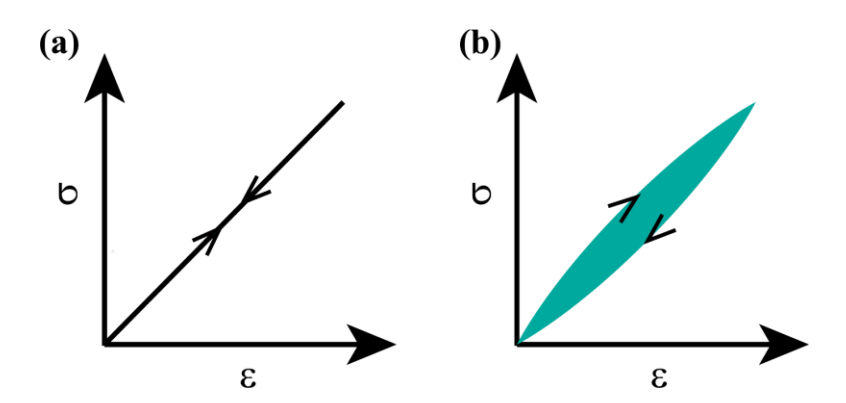


Figure 1.1: Schematic for stress (σ) – strain (ϵ) relation under the application of cyclic deformation for (a) ideal elastic material and (b) viscoelastic material exhibiting hysteresis.

1.2 Traditional spring-dashpot models for viscoelasticity

The earliest conceptual models for simplistic explanation of the elastic and viscous components contributing to viscoelasticity include arrangements of springs and dashpots in various configurations to mimic the elastic and viscous response respectively. Common arrangements are shown schematically in Figure 1.2 and include the Maxwell model (spring and dashpot in series), the Kelvin-Voigt model (spring and dashpot arranged in parallel) and the standard linear solid model (spring in parallel with the Maxwell element) [17]. These models are useful for qualitatively understanding viscoelastic phenomena such as stress-relaxation (Maxwell model), creep (Kelvin-Voigt model) or a combination of the two (standard linear model). Time-dependent stress-strain relations can be written by considering the distribution of stress and strain within the elements and with appropriate initial conditions. A large number of linear combinations of these elements can be considered in various configurations, as has been done in many studies to explain experimental data [18], [19]. However, these models cannot be used beyond their pedagogical relevance for atomistic mechanisms responsible for damping in complex materials; one has to use higher-level theories for the same.

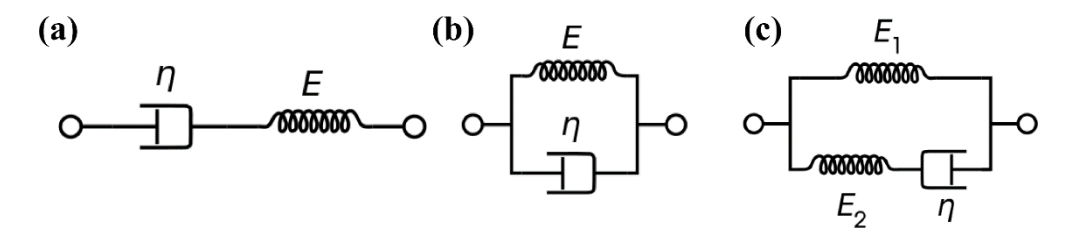


Figure 1.2: Spring-dashpot models for viscoelasticity. (a) Maxwell model, (b) Kelvin-Voigt model and (c) standard linear solid model.

1.3 Frequency-dependent dynamic moduli

The most common metric for characterizing viscoelastic damping in a material is the dynamic shear modulus (G^*). This is quantified by considering an oscillatory shear deformation where both shear strain (γ) with the shear stress (τ) vary sinusoidally and where the stress lags the strain by a phase difference (δ). G^* is then expressed as the complex sum of the "storage" and "loss" moduli, according to Eqn. (1.1).

$$G^* = G\cos(\delta) + iG\sin(\delta) \tag{1.1}$$

The quantity G here, represents the ratio of peak shear stress to strain. The storage modulus ($G' = G \cos(\delta)$) is the elastic component of the deformation that stores the recoverable elastic energy. The loss modulus ($G'' = G \sin(\delta)$), on the other hand corresponds to the viscous component of the modulus that leads to *lossy* behavior that typically manifests as heat dissipation during deformation. Another quantity relevant for damping is the so-called loss tangent, $tan(\delta)$ which is nothing but the ratio of loss to storage modulus. Both loss modulus and loss tangent represent the extent of damping in the material.

An important characteristic of the complex modulus is that it is strongly dependent on the rate of deformation (or, as in the case of oscillatory shear deformation, on the shear frequency). This frequency (or time) dependence is a consequence of the inherent viscous character of the material. A typical dependence of storage and loss modulus and loss tangent on the shear frequency is depicted in Figure 1.3.

This general frequency-dependent damping could be understood as follows. At very low frequencies, the deformation rate is low enough that stress can keep up with the driving strain or vice-versa, with the result that δ tends to zero and so do the loss tangent and loss modulus. Storage modulus on the other hand is finite owing to the small stress supported by the material. On the opposite spectrum of frequency, in the high-frequency limit, the deformation rate is so high that the material essentially behaves like a highly elastic glassy solid. This again, results in negligible δ , but the storage modulus increases drastically due to highly elastic behavior that supports large stresses. At intermediate

frequencies however, a characteristic peak in the loss tangent and loss modulus is observed. The reason for this is that, at these frequencies, the driving frequency is similar in magnitude to the frequency of the dissipative mechanism, leading to activation of the dissipative mechanism. For instance, a few mechanisms for dissipation include relaxation of chain segments in the case of polymers [20] or frequencies corresponding to phonon relaxation times at THz frequencies [21] in solids.

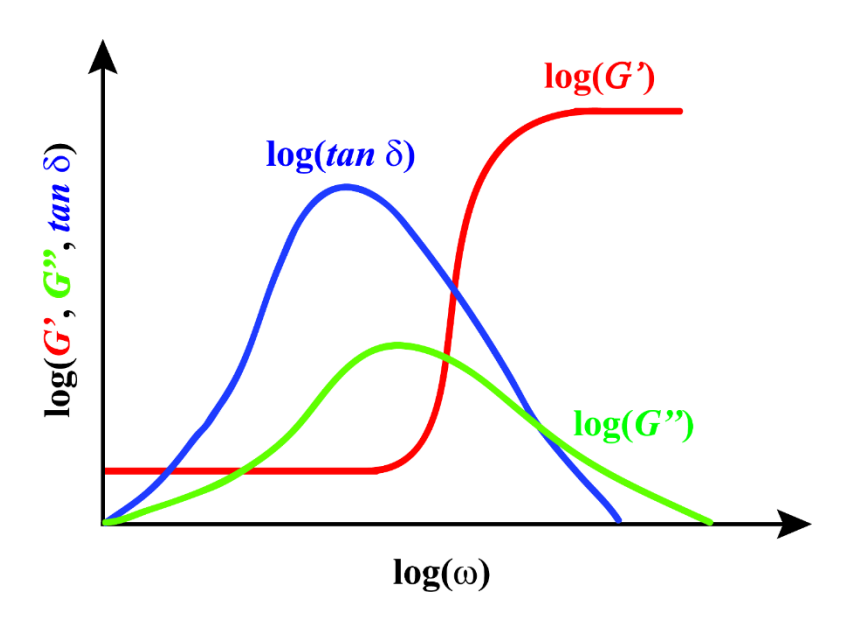


Figure 1.3: Schematic for variation of viscoelastic characteristics (storage modulus (G'), loss modulus (G'') and $\tan \delta$ with respect to shear frequency (ω)). Figure adapted from Ref. [22].

1.4 Viscoelastic damping in materials: some perspectives

A large body of work exists in the study of viscoelasticity of soft matter. The promise of polymer-based materials as materials suitable for significant viscosity has been well-recognized over the years and rheological studies on polymers have had a long history. Experimental characterization of viscoelasticity has seen numerous advancements with initial rheometers [23] coming a long way to state-of-the-art *dynamic mechanical analysis* equipment enabling accurate stress-strain measurements over multiple decades in frequency [24], [25]. Several complex phenomena that affect damping, including the effect

of semicrystallinity, effect of temperature all the way up to glass transition and microstructural features in polymer nanocomposites have been studied [5], [18], [26], [27]. Closely following experimental studies are several theoretical works in this field [20], [28]–[30].

The promise shown by soft matter is their inherently large loss tangent $(tan(\delta))$ values arising from the highly viscous nature of interaction between polymer chains. However, if one were interested in obtaining large damping properties (large loss moduli), equally important is the stiffness of the material (note that loss is contributed by the product of shear modulus and the sine of δ). In fact, if one were to plot the stiffness as a function of $tan(\delta)$ for various materials as shown in Figure 1.4 (here, Young's modulus, E is proportional to the shear modulus), we observe that traditional high-strength materials such as metals and alloys such as steel exhibit large stiffness, but low $tan(\delta)$. On the other hand, soft materials such as polymers show the opposite trend. To enhance damping, materials that simultaneously exhibit large stiffness and large $tan(\delta)$ are required, as observed for certain hard, composite materials in the upper right corner of Figure 1.4.

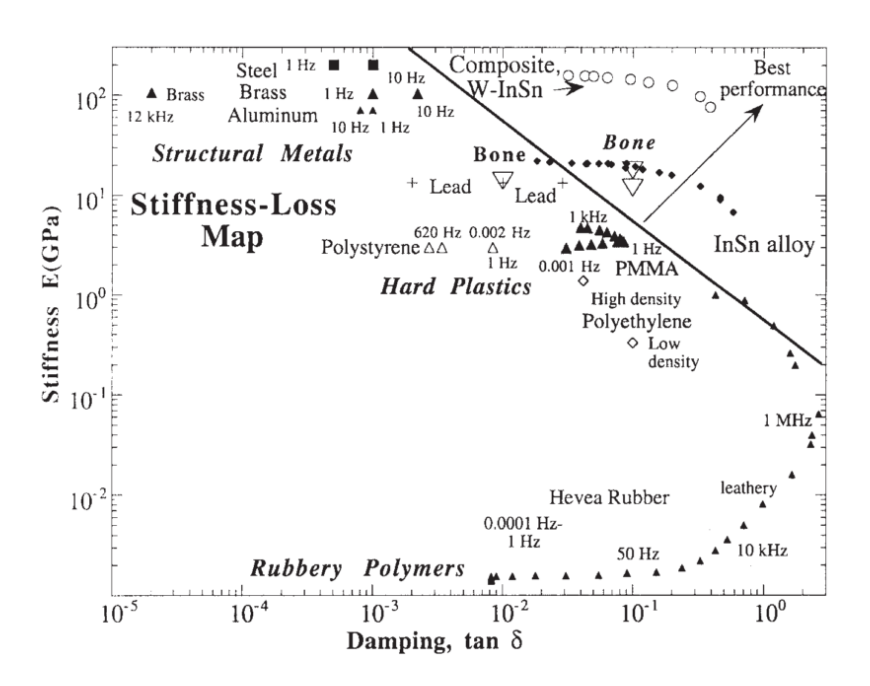


Figure 1.4: Comparison of stiffness (Young's Modulus, E) and $\tan \delta$ for a wide range of materials with contrasting properties. Damping is maximized for materials with higher stiffness and higher $\tan \delta$ as shown in top right corner for certain hard materials. Figure adapted from Ref. [31].

1.4.1 Damping in hard materials

Hard inorganic solids with high stiffness and potentially high loss tangent are ideal materials for damping applications and have only recently seen significant developments. A brief review of candidate materials that exhibit large damping is presented here.

Ma et al. [32] studied damping in multicomponent AlCoCrFeNi high entropy alloys and demonstrated significantly increased damping with increasing Al content. Schaller [12] studied the loss behavior in Mg-Si metal matrix composites and observed large viscous damping arising from successive pinning and unpinning of dislocations during cyclic shear loading. Muthusamy et al. [33] reported exceptional damping properties in cement-matrix graphite network composite with the loss factor approaching 0.8. Srikanth et al. [34] showed that by progressively adding more and more copper to a magnesium alloy, the damping capacity could be enhanced by about 100%.

Ferroelectrics are another class of materials that demonstrate high loss moduli arising from switching of domains in the presence of oscillating electric fields [35]. It has also been shown that presence of a negative stiffness phase (those that are pre-constrained by residual forces) in composites can give rise to very high damping [36]–[38] with a loss factor on the order of 1 to 4. However, these materials require a positive stiffness phase to maintain mechanical integrity.

In the context of damping in these hard materials, an important aspect is the ubiquitous frequency-dependence. Widely different mechanisms could potentially be at play with respect to the driving frequency. In glasses for instance, low-frequency deformation is known to result in long time-scale structural relaxation. Going up the frequency scale, devices such as micromechanical and nanomechanical resonators require large quality factors (low damping) [39]–[41], extending up to GHz frequencies. The upper end of frequency spectrum (THz range) is relevant for high-frequency damping properties in phononic interconnects [13], and attenuation of sound [42]–[44].

This thesis aims to address mechanisms for damping in a wide range of hard inorganic solids, as highlighted in the next section.

1.5 Objectives

In this thesis, we seek to understand atomistic mechanisms for viscoelastic damping in a wide range of hard, inorganic solids. We use non-equilibrium molecular dynamics (MD) simulations to perform oscillatory shear deformation, and uncover novel frequency-dependent mechanisms for damping. With a view to understanding structure-property relations in these materials that has far-reaching implications in tuning the damping capacity, we address mechanisms of damping in three classes of inorganic solids:

- 1. Crystalline composites: We construct crystalline composites composed of stiff, spherical crystalline inclusions embedded within a soft crystalline matrix. We describe the roles played by heterogeneous deformation, vibrational properties of the composite and microstructure on damping. We also draw parallels with damping characteristics in model superlattice structures.
- 2. Ordered, random and glassy alloys: We explore the role played by structure on frequency-dependence of damping. Described by the same interaction parameters, these three structures represent stark contrast in structure and as we show, lead to distinct frequency-dependent damping characteristics.
- 3. *Glasses*: Glasses are structurally rich materials and their metastability leads to many interesting properties. Broadly speaking, since glasses have the common trait of lack of long-range order, we address the question: "does damping in glasses exhibit certain universal characteristics?" In addition, various factors that affect damping in glasses are explored.

The organization of this thesis is as follows. In chapter 2, we present a detailed overview on characterization of viscoelasticity via the application of oscillatory shear deformation including experimental techniques and the MD simulation methodology employed in this work. Chapters 3 to 5 deal with damping mechanisms in the three classes of inorganic solids described in the previous paragraph. Finally, we summarize our findings, highlight some perspectives and discuss scope for future work in chapter 6.

2. Characterizing viscoelasticity via oscillatory shear deformation: Overview of experiments and simulation methodology

In this chapter, we present an overview of application of oscillatory shear deformation to characterize viscoelasticity. Experimental capabilities using oscillatory shear have advanced over the last several decades and serve as a power tool for characterizing viscoelasticity. Pertinent to this methodology is the direct analog of molecular-level simulations involving oscillatory shear. Specifically, advancement in both theory and computational speed have enabled molecular dynamics shear simulations to be used for simultaneously modeling viscoelastic properties and gather insights in to atomistic mechanisms for the observed properties. The chapter is organized as follows: Section. 2.1 gives an overview of experimental techniques for characterizing viscoelasticity. In Sec. 2.2, we describe the oscillatory shear deformation methodology used in this thesis. Finally, Sec. 2.3 describes a few theoretical considerations relevant for this work.

2.1 Dynamic Mechanical Analysis experiments

Experimentally, the most powerful setup for measuring viscoelastic response is using the Dynamic Mechanical Analysis (DMA) technique. Oscillatory deformation, either in the form of a torque (imparting shear deformation) or axial forces is applied on the sample, following which stress-strain data are accumulated. The phase difference between the two characterizes the frequency dependent storage and loss moduli and the loss tangent. A schematic for a typical DMA setup is shown in Figure 2.1 [45]. The sample is placed in between two parallel plates through which an axial or torsional force is applied by means of a force motor. Stress and strain (or alternately, force and displacement) are typically measured using force transducers and optical encoders [45]. DMA became popular in the field of soft matter rheology [5], [23] and has been used extensively for a variety of polymers and polymer composites [5], [26], [27], [45]. Routine applications of DMA include characterization of frequency and temperature dependence of elastic moduli both in linear and non-linear viscoelastic regimes [45].

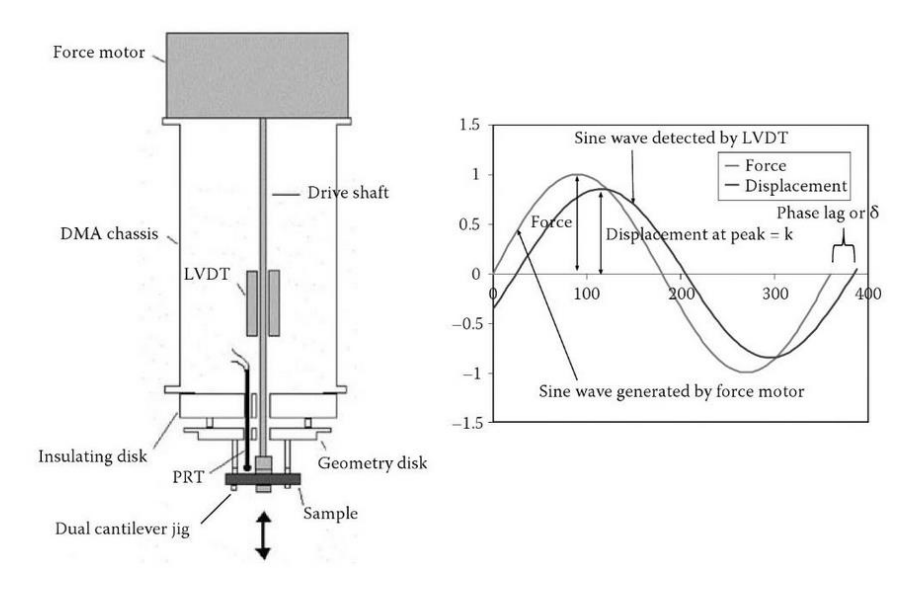


Figure 2.1: Schematic of the Dynamic Mechanical Analyzer. Right panel shows schematic of phase lag between measured force and displacement (or alternately, between stress and strain) [45].

In the field of hard materials, a variation of the DMA setup is employed, where, instead of application of forces via mechanical motors, electromagnetic impedance is used. Chen and Lakes [24] devised an experimental set up whereby an electromagnetic torque is applied to one end of the sample holder, that drives the oscillatory deformation. This technique and its variants have been used extensively to study viscoelastic damping in various hard alloys including tin-based alloys [46] [25], vanadium-tin composites [38] and ferroelectrics [35] over multiple decades in frequency.

2.2 Simulation protocol: Atomistic mechanisms for viscoelasticity

In this thesis, we use oscillatory shear deformation simulations under the purview of molecular dynamics (MD) to understand atomistic mechanisms for viscoelastic damping in hard inorganic materials. This technique is a direct analog of the experimental setup described in the previous section, and is explained in the following sections. A few theoretical considerations for our modeling protocol are also discussed in the next section.

2.2.1 Molecular dynamics simulations

A Molecular dynamics (MD) simulation involves solving Newton's equation of motion numerically, with forces between various particles (atoms/molecules) described by a well-defined force field [47]. MD is a very powerful technique for studying structure-property relations in a wide range of materials and has been extensively used for modeling atomistic phenomena responsible for mechanical properties, heat transport, phase transformations, among others [47], [48]. In particular, MD is well-suited for modeling mechanical properties under shear (which forms the basis of this work) and has been employed to study inorganic solids [49] and soft matter [20], [26].

2.2.2 Oscillatory shear deformation

Viscoelastic properties are studied using non-equilibrium oscillatory shear deformation simulations. We apply a homogeneous, sinusoidal shear strain, γ_{xy} , with a shear frequency (f) to the cubic simulation cell as described in Eqn. (2.1):

$$\gamma_{xy} = \gamma_o \sin(2\pi f t) \tag{2.1}$$

where γ_{xy} refers to strain applied within the xz-plane along the x-axis in a right-handed coordinate system, γ_o is the maximum shear strain imposed on the system and t is time. A schematic for the shear deformation via tilting of the simulation cell is shown in Figure 2.2. Using the molecular-level virial formula [50], we then calculate the resulting shear stress, τ_{xy} . Note that during this shear deformation, the simulation box volume remains constant while the shape of the simulation cell changes due to the applied shear strain.

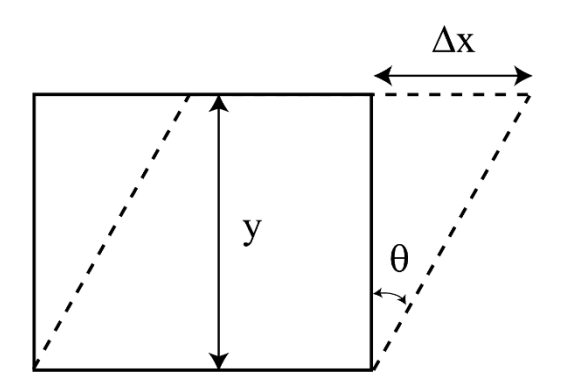


Figure 2.2: Schematic showing deformation of a cubic box (initial) by the application of a shear strain. The magnitude of strain is $\gamma = \Delta x/y$.

One expects τ_{xy} to follow the same sinusoidal profile as γ_{xy} and this is indeed seen to be the case in all our simulations. Therefore, the shear stress can be described by a sinusoidal function having a phase shift angle (δ) as described in Eqn. (2.2).

$$\tau_{xy} = \tau_0 \sin(2\pi f t + \delta) \tag{2.2}$$

The phase angle (δ) is a measure of the viscoelasticity of the material. Purely elastic materials have $\delta = 0^{\circ}$ and purely viscous materials have $\delta = 90^{\circ}$. In the current simulations, we accumulate τ_{xy} over multiple shear cycles to calculate the peak value of shear modulus (G), which is defined as the ratio of the maximum shear stress $(\tau_{xy,max})$ and the maximum shear strain $(\gamma_{xy,max})$. The complex shear modulus (G^*) is then expressed as the complex sum of the storage $(G' = G \cos(\delta))$ and loss $(G'' = G \sin(\delta))$ moduli as per Eqn. (2.3).

$$G^* = G\cos(\delta) + iG\sin(\delta); \text{ where, } G = \frac{\tau_{xy,max}}{\gamma_{xy,max}}$$
 (2.3)

Figure 2.3 shows the above procedure in a simple flowchart. The loss modulus governs the extent of mechanical damping under the given conditions (material properties, deformation conditions) and is used synonymously with damping throughout this work.

$$\gamma_{xy} = \gamma_o \sin(2\pi f t)$$
Apply sinusoidal strain
(Tilt simulation cell face)
$$\tau_{xy} = \tau_o \sin(2\pi f t + \delta)$$
Compute stress
(Fit to sine curve)
$$G = \frac{\tau_{xy,max}}{\gamma_{xy,max}}$$

$$G^* = G \cos(\delta) + iG \sin(\delta)$$
Compute complex modulus

Figure 2.3: Flowchart for computing the complex shear modulus from the stress-strain profile

We study viscoelasticity in a range of hard inorganic materials, with different interaction energies between constituent atom types. These would be described in the specific sections that explore damping for these cases (Chapters 3 to 5). Here, as an example for stress-strain relations, Figure 2.4 shows averaged shear stress and strain profiles for a specific case of a crystalline composite system (composed of a stiff inclusion in a soft matrix, as shown in the inset). The shear frequency is $f = 0.2 \text{ ps}^{-1}$. As seen from the figure, the significant phase shift of $\delta = 22^{\circ}$ results in an appreciable loss modulus, G'' = 1567 MPa.

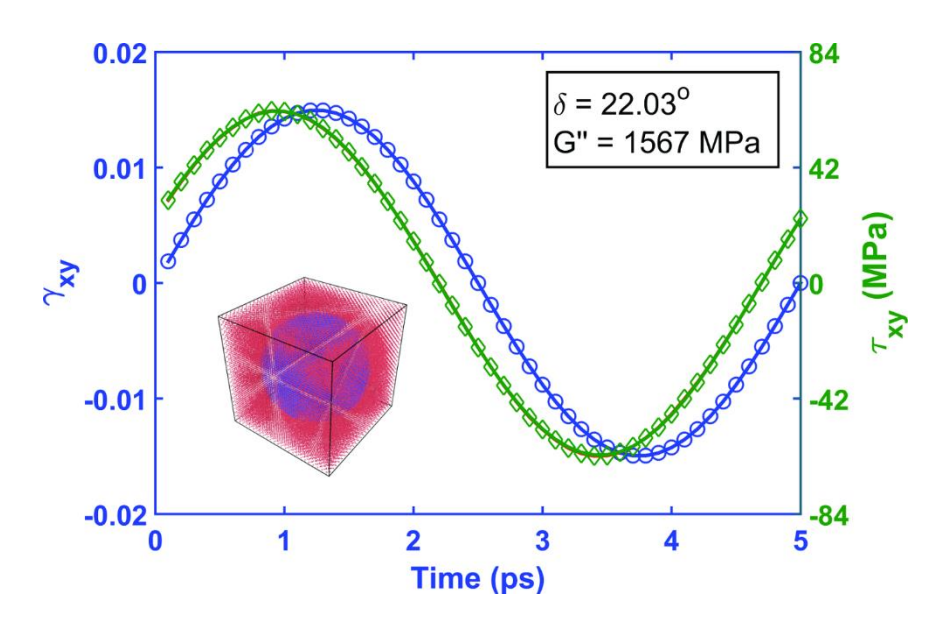


Figure 2.4: Sample result for relation between applied shear strain (shown by blue circles) and the resultant shear stress (green) during oscillatory shear deformation of a crystalline composite (shown in inset). Stress data have been averaged over 5 shear cycles.

2.2.3 Simulation details

Oscillatory shear deformation simulations are performed for a wide range of inorganic solids including crystalline composites, ordered and random alloys and various glasses. For each case, the force field used for the model and simulation conditions are presented in the respective chapters (chapters 3 to 5). Starting from well-equilibrated structures at

zero external pressure and temperature well below the melting point/glass transition temperature, shear deformation is carried out under the constant volume-constant energy (NVE) ensemble. This allows us to measure the energy dissipated during shear directly (refer to Sec. 2.3.2 below). Frequency-dependent loss moduli are computed over a wide range of frequencies (spanning 3 to 5 decades) ranging from MHz to THz. Stress-strain data are typically averaged over 5 cycles of oscillatory shear. Additionally, we also consider shear under constant volume-constant temperature (NVT) conditions for shear deformation of glasses, where we are interested in capturing long time-scale structural evolution. The coupling to a thermostat to maintain constant temperature is necessary to avoid unreasonable temperature rise at high frequencies, where we accumulate stress-strain data over 100,000 cycles (chapter 5). All MD simulations have been carried out using the LAMMPS simulation package [51].

2.3 Theoretical considerations

2.3.1 High-frequency damping: role of vibrational modes

Typically, experimental studies of viscoelasticity probe dynamic moduli over frequencies ranging from few thousandths of Hz to few KHz [46]. Computer simulations are inherently limited by the extent of time-scales that can be simulated, and currently can probe frequencies only down to a few MHz for reasonably large systems. On the upper limit of frequencies, MD simulations are ideally suited for THz frequencies. We note that the range of shear frequencies simulated in this work is from 10s of MHz to 10s of THz.

In the THz range, the dominant mechanism for viscoelastic damping in hard materials arises from anharmonic coupling of vibrational modes as will be described in detail in Chapters 3 to 5. To the best of our knowledge, this thesis is the first study to uncover this mechanism for a range of hard inorganic materials using MD simulations.

Vibrational eigenstates of the system were computed by the well-known method of diagonalization of the dynamical matrix [52], [53], with the normal mode solution [54] of the form:

$$u_{j\alpha\lambda} = \frac{1}{\sqrt{m_i}} \, \varepsilon_{j\alpha\lambda} \, e^{i\omega_{\lambda}t} \tag{2.4}$$

Here, m_j is the mass of atom j and ω_{λ} are the eigen frequencies. The eigenvector components, $\varepsilon_{ja\lambda}$ satisfy the following eigenvalue equation:

$$\omega_{\lambda}^{2} \, \varepsilon_{j\alpha\lambda} = \, \sum_{k\beta} \Phi_{j\alpha,k\beta} \, \, \varepsilon_{j\beta,\lambda} \tag{2.5}$$

The elements of the dynamical matrix, $\Phi_{j\alpha,k\beta}$ within the harmonic approximation is given by:

$$\Phi_{j\alpha,k\beta} = \frac{1}{\sqrt{m_j m_k}} \frac{\partial^2 V}{\partial u_{j\alpha} \partial u_{k\beta}}$$
 (2.6)

where, $u_{j\alpha}$ is the displacement of atom j in the α coordinate direction and V is the total potential energy. For structures considered in this work, vibrational frequencies were calculated by the diagonalization of the dynamical matrix [55] using the Xenoview software [56].

2.3.2 Heat dissipation during shear

It is well-known that during oscillatory shear deformation, the loss modulus component manifests as heat dissipated to overcome the damping mechanism [5]. In polymers, for instance, the mechanism involves dissipation due to viscous forces between the polymer chains [3], [5] and in hard materials, it could arise from local relaxation processes such as atomic diffusion and dislocation motion [16] or, at high shear frequencies approaching vibrational frequencies (order of few THz), it could arise from anharmonic coupling between vibrational modes [57].

In this section, we present a simple analytical approach to estimate the heat dissipated due to shear deformation based on deformation conditions and material properties. Using MD shear simulations, one can easily compute the increase in energy due to shear, under

NVE conditions. We corroborate the analytically computed heat dissipation with direct MD observation of energy increase and note that these values agree very well, with an error typically less than 5%.

We begin by assuming the heat dissipated is solely due to the work done by the applied shear force. This is given as:

$$W = \int F_{xy} \cdot dx \tag{2.7}$$

Noting that the shear force, F_{xy} is the product of shear stress (σ_{xy}) and the area over which the force acts (Eqn. (2.8)) and the displacement x and shear stress are sinusoidal with respect to time with a frequency, f (the latter with a phase shift δ with respect to displacement) according to Eqn. (2.9),

$$F_{xy} = \sigma_{xy} A_{xy} \tag{2.8}$$

$$x = x_o sin(ft); \sigma_{xy} = \sigma_o sin(ft + \delta)$$
 (2.9)

one obtains the work done over a single oscillatory cycle with time period, T_p as per Eqn. (2.10):

$$W = \sigma_o x_o \omega A_{xy} \int_0^{T_p} \sin n(ft + \delta) \cos(ft) dt$$
 (2.10)

Extending this for N cycles of shear and noting that $f = 2 * \pi/T_p$, the integral can be simplified to yield the following equation:

$$W = N\pi\sigma_o x_o A_{xy} \sin(\delta) \tag{2.11}$$

Here, both deformation conditions (σ_o, x_o) and the material property $(sin(\delta))$ determine the extent of heat dissipated (or extent of damping). We observe a very good agreement between the predicted value as per Eqn. (2.11) and direct observation of heat dissipated from MD simulations, for the entire spectrum of frequency studied (over 3 to 5 decades), for an extensive range of materials simulated (including hard composites and soft polymers and nanocomposites).

3. Viscoelastic damping in crystalline composites

In this chapter, we present a detailed analysis of viscoelastic damping in crystalline composites consisting of soft and stiff phases. The organization of the chapter is as follows: Section 3.1 introduces several studies on damping in hard, inorganic solids and strategies to enhance damping. Description of model structures is presented in Sec. 3.2. The key results and discussion on damping in composites consisting of spherical inclusions and superlattice structures are presented in Sec. 3.3. Finally, Sec. 3.4 contains the summary and conclusions.

3.1 Introduction

Versatility in tuning viscoelastic properties from a purely viscous to a purely elastic behavior has enabled a wide range of engineering applications such as artificial tissues [13], functional foams [14], optoelectronics [15] among a slew of structural and mechanical applications [16]. Viscoelasticity can be exploited to synthesize materials with exceptional damping properties. Notably, polymer composites have been designed for damping and noise reduction in automobiles and airplanes [6], conferring structural stability during wind and earthquake induced vibrations [7], and mechanical damping in a number of applications [8]–[12]. There exists a large body of work on experimental characterization of damping and its dependence on various variables like temperature, microstructure and shear deformation frequency for polymer and fiber composites [11], [58]–[61].

Recently, viscoelasticity in crystalline materials such as metals and alloys has garnered a lot of attention. The promise of these materials is to maintain high stiffness (high elastic modulus) while providing significant damping, i.e., relatively high loss modulus. For example, Ma et al. [32] studied damping in multicomponent AlCoCrFeNi high entropy alloys and demonstrated significantly increased damping with increasing Al content.

Portions of this chapter previously appeared as: R. Ranganathan, R. Ozisik and P. Keblinski, "Viscoelastic damping in crystalline composites: A molecular dynamics study", Composites Part B 93, 273 (2016).

Schaller [12] studied the loss behavior in Mg-Si metal matrix composites and observed large viscous damping arising from successive pinning and unpinning of dislocations during cyclic shear loading. Muthusamy et al. [33] reported exceptional damping properties in cement-matrix graphite network composite with the loss factor approaching 0.8. Srikanth et al. [34] showed that by progressively adding more and more copper to a magnesium alloy, the damping capacity could be enhanced by about 100%.

Ferroelectrics are another class of materials that demonstrate high loss moduli arising from switching of domains in the presence of oscillating electric fields [35]. It has also been shown that presence of a negative stiffness phase (those that are pre-constrained by residual forces) in composites can give rise to very high damping [36]–[38] with a loss factor on the order of 1 to 4. However, these materials require a positive stiffness phase to maintain mechanical integrity.

A large body of theoretical work in predicting upper and lower bounds for elastic and shear moduli for materials has been performed over the years. These are either based on the well-known variational theory propounded by Hashin and Shtrikman [62], [63]; continuum based methods [64]–[66] or multiscale modeling [67]. Also popular are techniques that couple homogenization theory to obtain bounds for elastic moduli and a structural optimization algorithm to model microstructures with tunable properties [68]. While these methods are valuable predictive tools for estimating composite viscoelastic properties, a deeper understanding of the underlying mechanisms is possible only using molecular level simulations.

Here, we employ non-equilibrium molecular dynamics shear simulations to study viscoelasticity of model crystalline composites with various microstructures as a function of shear rate. We limit ourselves to deformations where there are no defects such as dislocations formed, thus, damping arises purely from the anharmonic coupling between vibrational modes.

3.2 Model structures and simulation details

3.2.1 Model structures

Our model composites comprise "stiff" spherical inclusions embedded within a "soft" matrix. Both phases are crystalline, in a face centered cubic (FCC) lattice, and are modeled by the standard 12-6 Lennard Jones pair potential:

$$E = 4\varepsilon \left[\left(\frac{\sigma}{r} \right)^{12} - \left(\frac{\sigma}{r} \right)^{6} \right]$$
 (3.1)

where ε and σ are the energy and length scale parameters. For the soft phase, ε and σ are set as 0.01 eV and 3.405 Å, respectively, corresponding to parameters for FCC crystal of argon [69]. The ε for the stiff phase (denoted as atom type "A") is increased by four times that of the soft phase (denoted as atom type "B"). The σ values are the same for both soft and stiff crystals rendering the interface between them epitaxial and resulting in very low residual stresses. A common cutoff of 10 Å is used for truncating the potential interaction.

In addition to composites consisting of spherical inclusions of the stiff phase, we consider superlattice structures composed of similar stiff and soft crystalline components. Figure 3.1 shows the atomic snapshots of the two types of crystalline composites considered – in panel (a) is a composite with spherical inclusion of stiff phase (with volume fraction ~0.4) and in (b) is a superlattice structure with a superlattice width of 21.5 Å.

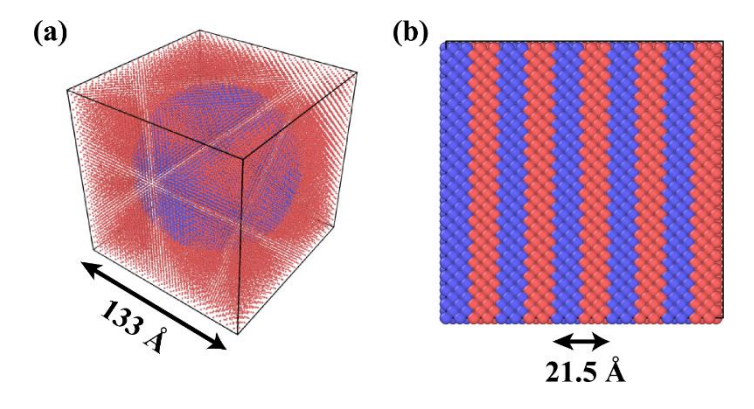


Figure 3.1: Snapshots of composite systems containing phases that have a stiffness contrast. (a) Spherical inclusion of stiff phase. (b) Superlattice structure consisting of 5 layers of *A-B* superlattice layers. Red atoms correspond to the soft crystalline component and blue, to the stiff component.

Estimation of viscoelasticity from averaged stress-strain curves during oscillatory shear deformation is depicted in Figure 3.2. The oscillatory shear strain (γ_{xy}) imposed on the system is shown in blue and the resulting shear stress (τ_{xy}) is shown in green. The stress-strain data are averaged over 40 shear cycles and the time period of oscillations is 5 ps ($f = 0.2 \text{ ps}^{-1}$). Panels (a), (b) and (c) in Figure 3.2 correspond to results obtained from homogeneous soft phase, a composite with volume fraction of stiff phase, $\phi \sim 0.4$ and, homogeneous stiff phase, respectively. The phase angle (δ) between stress and strain and the magnitude of shear modulus are also shown for all three cases. We observe that for homogeneous phases (both soft and stiff) as seen in Figure 3.2(a) and (c), δ is close to zero, resulting in a negligible loss modulus. On the other hand, the composite microstructure shows a large δ (\sim 22°) leading to significant loss modulus.

For all shear simulations, we first equilibrate the system at 40 K and zero pressure using a Nose-Hoover thermostat [70], [71] for 400 ps. The choice of temperature is to keep it well below the melting point of the soft phase (84 K) [72]. The damping time constants for the thermostat and barostat are 100 fs and 200 fs, respectively. This is followed by further equilibration at constant volume and constant temperature (NVT) ensemble for 400 ps.

The equilibrated structures are then subject to the oscillatory shear simulations at constant volume and constant energy (NVE) ensemble to characterize viscoelasticity. The thermostat is removed during shear in order not to artificially remove the heat dissipated during shear. Additionally, this allows us to monitor the rise in the system temperature (and energy) during shear, and thus, we ensure that the shear cycles are terminated well below the melting point of the soft phase. We note that the crystallinity of the composite is maintained during both equilibration and cyclic shear deformation stages, which were confirmed by negligible variation in the pair distribution function between the relaxed and strained structures and the coordination of all atoms, which was found to be equal to 12 (FCC).

For all simulations, the stress profiles were averaged over 3 to 5 cycles, ensuring that the system temperature does not exceed ~45 K. The simulation box size (L) ranged from 7 unit cells (~37 Å) to 25 unit cells (~133 Å) and the maximum shear strain imposed was

within 1.5%. All simulations were performed with the LAMMPS simulation package [51] with a timestep of 2 fs. Periodic boundary conditions were applied along all three axes.

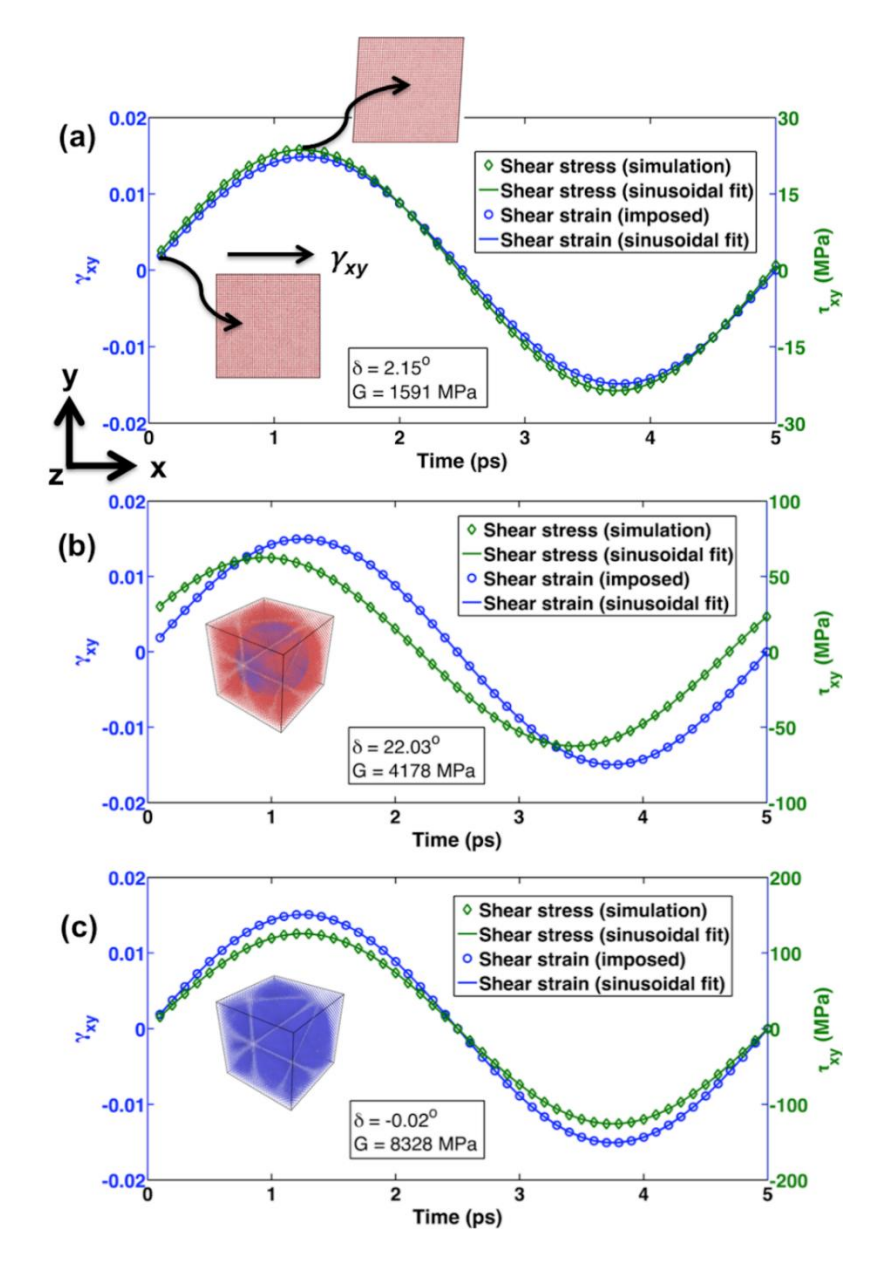


Figure 3.2: Estimation of viscoelasticity from averaged stress-strain curves during oscillatory shear deformation. Shear strain (γ_{xy}) is the input and shear stress (τ_{xy}) is the output. Panels (a) and (c) are for homogeneous soft and stiff phases respectively that exhibit negligible phase difference. Panel (b) is for a composite with the volume fraction of stiff phase, $\varphi \sim 0.4$, exhibiting significant phase shift and thus, a large loss modulus. Side views in panel (a) show the zero-strain and maximum strain configurations during the shear cycle.

3.3 Results and discussion

3.3.1 Vibrational analysis

The viscoelastic properties of a material are likely to be dictated by its vibrational properties in our simulations, as no defect formation or bond breaking are observed. During the oscillatory shear deformation, the energy dissipation occurs via the anharmonic coupling between the various phonon modes. The degree of anharmonic coupling between the phonon modes determines the extent of viscoelastic loss in such material. A direct measure of this is the mode-dependent Grüneisen parameter, γ [73], defined by Eq. (3.2). γ relates the shift in individual phonon frequencies (ω_i) to infinitesimal changes in system volume, V.

$$\gamma_i = -\frac{v}{\omega_i} \frac{\partial \omega_i}{\partial V} \tag{3.2}$$

where γ_i is the Grüneisen parameter of the i^{th} phonon mode. A larger γ implies greater energy dissipation (loss) due to larger anharmonic coupling.

We calculate γ for all the system frequencies using Eq. (3.2) upon deforming the simulation cell isotropically, during which the volume is changed by 1% about the equilibrium volume. For each volume, the phonon frequencies were calculated by the diagonalization of a dynamical matrix [55] using the Xenoview software [56] (Refer to Sec. 2.3.1 for additional details on the calculation method).

Shown in Figure 3.3 is the variation of γ_i for various composites ranging from $\phi = 0$ (fully soft) to $\phi = 1$ (fully stiff) for L = 7 unit cells. The homogeneous soft phase ($\phi = 0$) shows a maximum γ of about 8 at the low frequency end (~0.2 THz). The pure stiff phase ($\phi = 1$), has a maximum γ of about 5. The two intermediate volume fractions ($\phi = 0.27$ and $\phi = 0.47$) exhibit much larger γ (for example, at $\phi = 0.47$, ~2 and ~3 times larger than homogeneous soft and stiff phases, respectively) at lower frequencies (< 1.6 THz), which is due to a large strain concentration in narrow regions of the soft phase. Interestingly, at higher frequencies (modes contributed by the stiff phase), γ is suppressed for the composite, which is a consequence of the heterogeneity in deformation.

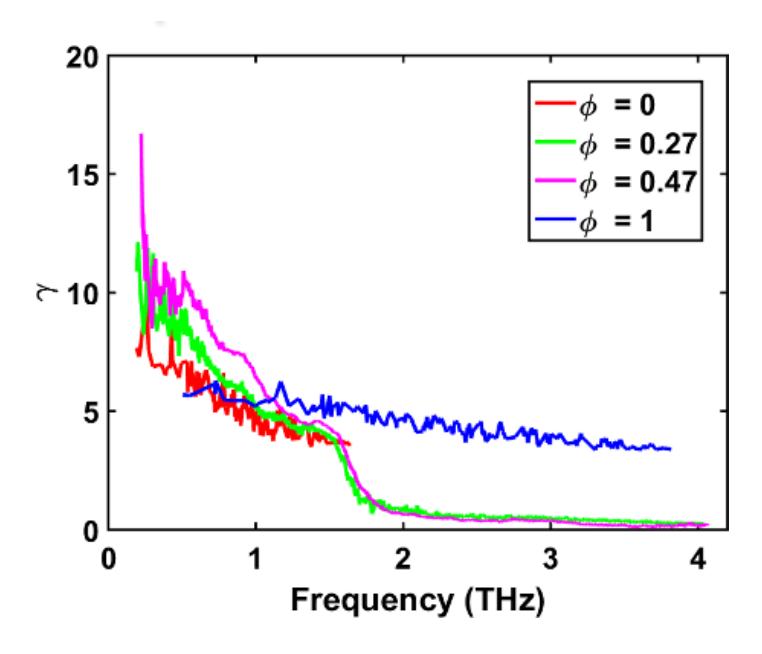


Figure 3.3: Variation of mode-dependent Grüneisen parameters for various composites, ranging from $\varphi = 0$ (fully soft) to $\varphi = 1$ (fully stiff) for a system size of L = 7 unit cells.

3.3.2 Local strain distribution

To quantify local deformation during shearing in our model composites, local shear strains were calculated along the radial direction, starting at the center of the stiff inclusion. We consider deformation over one quarter of shear cycle (until maximum shear strain is reached) for a total $\gamma_{xy} = 0.025$ with a shear strain rate of 1×10^{-3} /ps. Shown in Figure 3.4 are the radial shear strain profiles for stiff and soft phases during shear for L = 25 and $\phi = 0.4$. A spherical bin width of 5.3 Å was used in the calculations and the radial distance was normalized by the length of the simulation cell. The shear strain data are also temporally averaged over a small time window (1.6 ps) for good statistics. The local γ_{xy} values are computed by dividing the shear modulus of the homogeneous phase by the accumulated shear stress (τ_{xy}) within a bin, which is further normalized by the overall shear strain. Strain distributions for both the undeformed, "relaxed" state and the fully deformed, "strained" states for the stiff and soft phases are shown in the figure. As seen from Figure 3.4, the soft phase is seen to experience a much larger shear strain (2 to 10 times greater) compared to the stiff phase. In addition, γ_{xy} in the soft phase increases monotonically with

radial distance with the least strain present at the epitaxial interface. Confinement of a softer phase in a composite can thus potentially result in significant viscous damping via large local deformation.

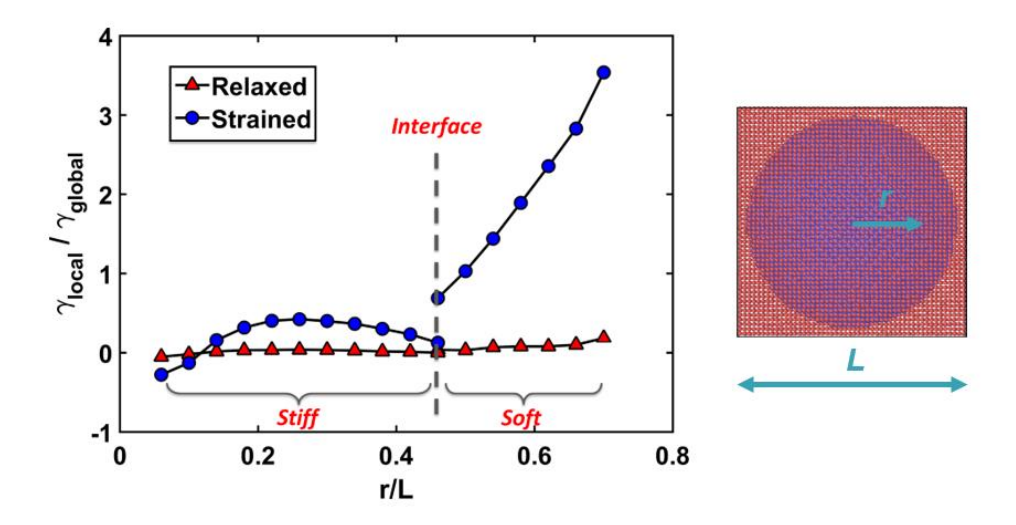


Figure 3.4: Spatial strain profiles for both the soft and stiff phases during one-quarter cycle of shear (till maximum amplitude in sinusoidal shear is reached). System size is L=25 unit cells. The soft phase undergoes shear strains much larger than the stiff phase.

3.3.3 Role of composite microstructure and shear frequency on damping

Viscous damping in materials is a complex phenomenon that depends on various factors. Among the most important are the structure of the material (i.e., the microstructure of crystalline composites) and the shear frequency. In this section, we study the effect of two important contributing factors to viscoelastic damping in composites, namely, the composite microstructure and shear frequency. The microstructural effect is studied in two ways. First, we fix the overall simulation cell size and vary the volume fraction of the stiff inclusion (denoted as "volume-fraction-sweep"). We then study the effect of shear frequency (denoted as "frequency-sweep") for various microstructural features. Here, the second kind of microstructural effect is realized by keeping the volume fraction of the

spherical inclusion fixed while varying the overall simulation cell size. Coupled with this are possible size effects that are also addressed.

At the nanoscale, microstructure is expected to play a very important role in damping due to a large interfacial effect. To understand the effect of microstructure on damping properties of crystalline composites, various simulations were performed where the volume fraction of the stiff phase (ϕ) is varied from 0 to 1 ("volume-fraction-sweep") while keeping the shear rate constant. It is also well known that viscous damping in materials is strongly affected by the shear rate [22]. At high shear rates, materials cannot respond to high rate of deformation, and consequently, behave like a glass with a high storage modulus and low viscous loss. In the low frequency regime, there is sufficient time for material to respond to shear deformation, which leads to elastic-like behavior and low viscous losses.

3.3.3.1 Effect of inclusion volume fraction

We study a range of microstructures by varying the volume fraction (ϕ) of the stiff inclusion. Shown in Figure 3.5 are the results for *volume-fraction-sweep* simulations for a fixed simulation box size of L=7 and at a constant shear frequency of 0.33 THz. Two possible arrangements of component phases were considered: (a) the inclusion being the stiff phase (shown by red circles) and (b) the inclusion being the soft phase (shown by green triangles). We observe that the loss modulus is close to zero for homogeneous compositions ($\phi=0$ and $\phi=1$). At intermediate fractions of the stiff phase (0.2 < ϕ_{stiff} < 0.6), there is significant viscoelastic damping and the maximum loss modulus of ~1500 MPa is approximately 25 times larger than that of the homogeneous soft phase. The loss modulus profiles of the two cases (soft versus stiff inclusion) are slightly different – the stiff inclusion case shows slightly enhanced damping. We suppose that this is due to the soft matrix experiencing the majority of the deformation and not transferring much of the deformation to the stiff inclusion.

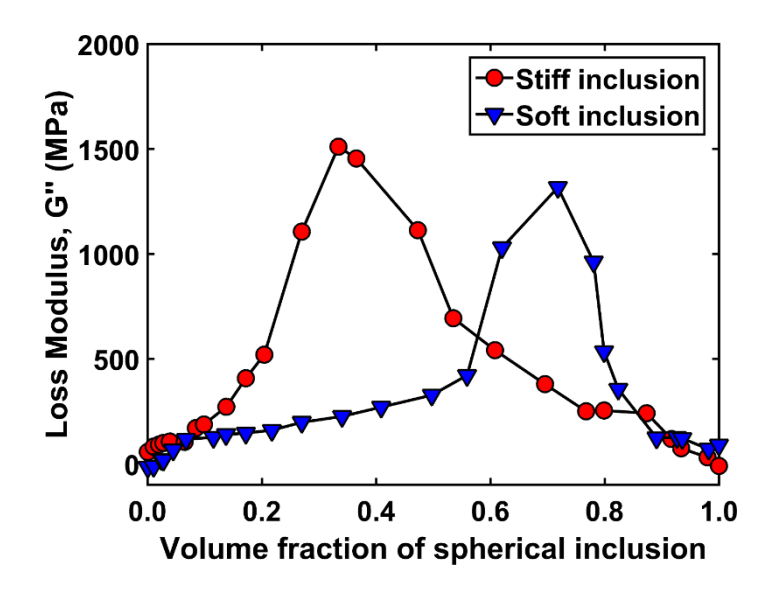


Figure 3.5: *Volume-fraction-sweep* simulations showing variation of loss modulus as a function of volume fraction of the spherical inclusion. The two sets of data represent the arrangement of the phases (the inclusion being either soft or stiff). The shear frequency is fixed at 0.33 THz.

3.3.3.2 Comparison with theoretical bounds for elastic moduli

Theories for several bounds for elastic moduli of composites exist in literature. Among these, the variational principle proposed by Hashin and Shtrikman [63] for elastic constants of composites has been used extensively for estimating the upper and lower bounds for the effective elastic moduli. These bounds (for bulk or shear modulus) of composites are described in terms of the volume fraction of individual phases and their respective elastic constants. By applying variational principles on the elastic polarization tensor, this formulation provides strict upper and lower bounds of the moduli attainable for any arbitrary phase geometry. For shear modulus, the bounds are given in terms of the volume fractions (ϕ) and the bulk (K) and shear moduli (G) of the two phases (indicated with subscripts "I" and "2") as follows:

$$G_L = G_2 + \frac{v_1}{\frac{1}{G_1 - G_2} + \frac{6(K_2 + 2G_2)\phi_2}{5(3K_2 + 4G_2)G_2}}$$
(3.3)

$$G_U = G_1 + \frac{v_2}{\frac{1}{G_2 - G_1} + \frac{6(K_1 + 2G_1)\phi_1}{5(3K_1 + 4G_1)G_1}}$$
(3.4)

where, the individual shear and bulk moduli, and the resultant upper and lower bounds for loss shear modulus are all complex quantities. We estimate these bounds for our model composites, where the phases I and 2 stand for homogeneous stiff and soft phases, respectively. The complex shear moduli for homogeneous phases are obtained directly from our shear simulations. The bulk moduli for the homogeneous phases were calculated by the formula K = -V * dP/dV upon small changes in volume and measuring the resulting total system pressure. We assume the same phase shift values (δ) for the bulk moduli as for the shear moduli.

Shown in Figure 3.6 is the comparison of loss modulus (G'') calculated from MD simulations as a function of volume fraction of the stiff phase, with the upper (G''_U) and lower (G''_L) bounds from Hashin-Shtrikman variational theory for a system with L=7 and f=0.33 THz. As seen from the figure, the maximum in the G'' values calculated from simulations is 20 times greater than the analytical upper bound predicted by the theory. Thus, at the nanoscale, we observe that huge strain concentrations in the soft phase can lead to loss moduli far greater than that predicted by macroscopic viscoelasticity theory.

The Hashin-Shtrikman theory assumes homogeneous deformation of component phases in a composite, and as a consequence, predicts the composite moduli bound by the inherent moduli of the component phases. In our model composites however, the selective deformation of the soft phase along with large Grüneisen parameters (as discussed in Sec 3.3.1) is responsible for this enhanced damping.

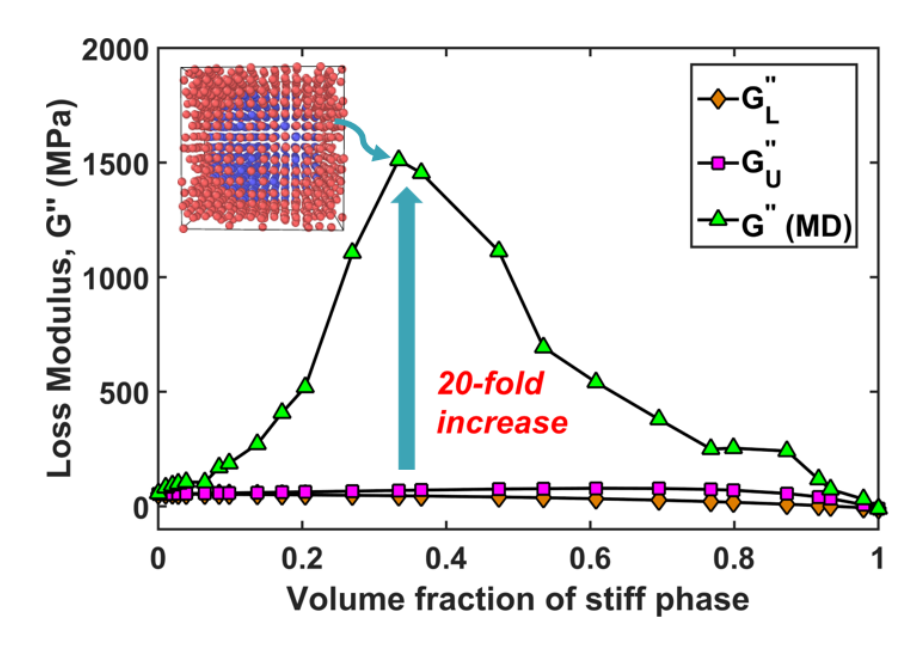


Figure 3.6: Comparison of loss modulus (G'') calculated from MD simulations for LJ composite with the upper (G''_U) and lower (G''_L) bounds from Hashin-Shtrikman theory. System size is L=7 unit cells and shear frequency is f=0.33 THz. The microstructure at maximum damping volume fraction is shown in inset.

3.3.3.3 Effect of inclusion stiffness

The stiffness of the inclusion phase should have a significant effect on damping; the bigger the contrast between the phases, the greater is the strain accommodated by the softer phase (the matrix). This is clearly seen in our simulations and is depicted Figure 3.7 for a composite with $\phi = 0.5$ and L = 7 at a shear frequency of 0.4 THz, which corresponds to the frequency of maximum loss modulus for this system. The relative stiffness (ε_{rel}) is represented as the ratio of ε_{stiff} to ε_{soft} . For a relative stiffness of one (homogeneous soft phase), we recover the negligible damping behavior of the homogeneous soft phase noted earlier in Figure 3.5. Loss modulus increases almost linearly with relative stiffness in the ε_{rel} range of 2 to 4 and begins to saturate for $\varepsilon_{rel} > 5$.

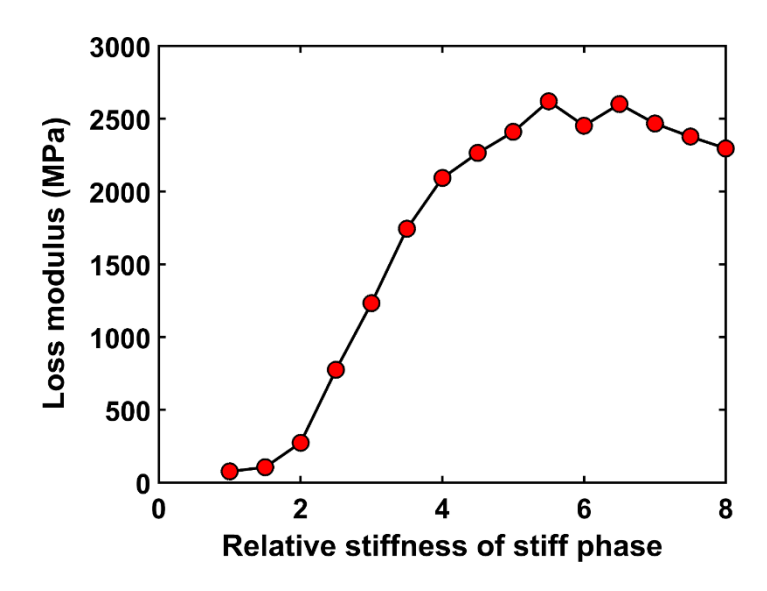


Figure 3.7: Variation of loss modulus with stiffness of the stiff phase. The relative stiffness is represented as the ratio of ε_{stiff} to ε_{soft} .

3.3.3.4 Effects of microstructure and simulation cell size

In this section, we first consider the possible size effect from the choice of simulation cell size on damping. Frequency-sweep simulations were performed for a composite with $\phi=0.5$ for three different structures. The first structure comprises of a single spherical inclusion with L=7 unit cells. The other two structures are obtained by replicating the base structure (L=7) two and three times in each axis to yield structures with L=14 and L=21 unit cells. These structures have eight and twenty-seven times the volume (and also number of inclusions) of the base structure respectively. Thus, here we merely study the effect of simulation cell size on damping, while preserving the same microstructure in all three structures. Shown in Figure 3.8 are the results of the frequency-sweep simulations for the three microstructures, with the maximum shear strain fixed at 1.5% for all cases. As seen from the figure, at either end of the shear frequency spectrum (low frequency end at $f \sim 0.01$ THz and the high frequency end at $f \sim 2$ THz), the loss modulus is negligibly small. At intermediate frequencies (0.3 < f < 1.5 THz), a large loss modulus results. This is because, at low frequencies, the system has ample time for the shear stress to respond to the strain. On the other hand, at high frequencies, the system is forced to follow the

extremely fast deformation, akin to a glassy behavior. For either case, the phase angle is close to zero. At intermediate shear frequencies that correspond to high Grüneisen parameters (refer to Figure 3.3), we observe significant damping, with the peak modulus value typically two orders of magnitude greater than that observed at the lowest frequency (0.01 THz). Thus, damping is greatly enhanced for composites near shear frequencies that correspond to the vibrational frequencies of the composite (as depicted earlier in Figure 3.3). Since we observe almost identical results for all three cases (which have identical microstructures), we conclude that there are no artifacts from the choice of the simulation cell size used in this work.

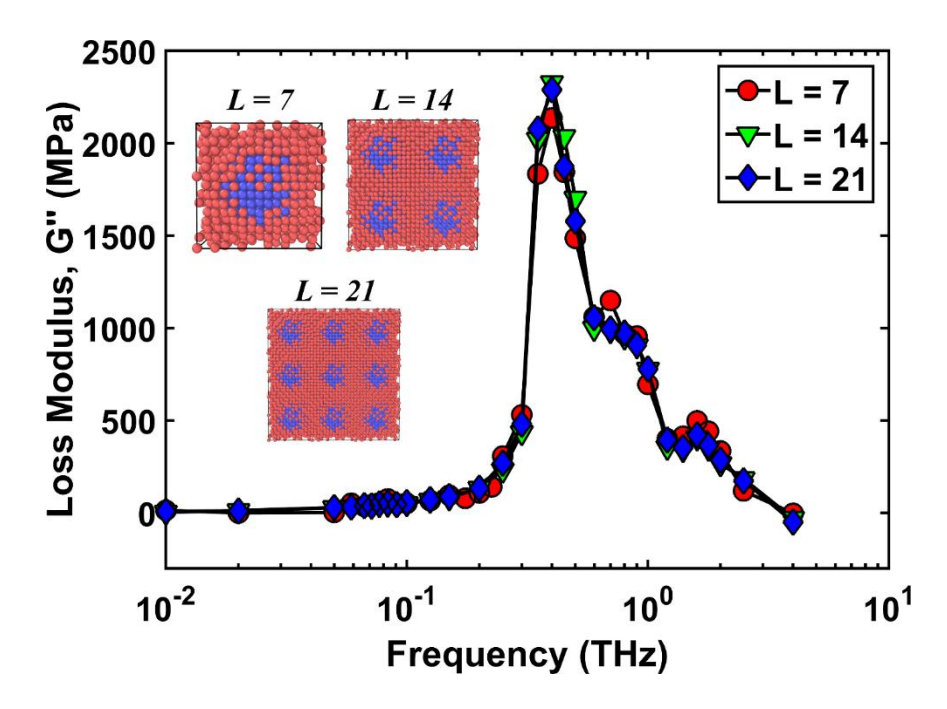


Figure 3.8: Frequency-sweep simulations for composite with volume fraction of stiff phase, $\varphi \sim 0.5$ for the base composite of size L=7 unit cells (red circles) and the base structure replicated twice (L=14 unit cells) and thrice (L=21 unit cells) along x, y and z axes (green triangles). The atomic snapshots for these structures are shown as insets.

Next, we explore the microstructural size effect by varying the simulation cell size while keeping the volume fraction of the stiff phase (ϕ) fixed. Shown in Figure 3.9(a) are the results of the *frequency-sweep* simulations depicting the variation of loss modulus with

frequency for various system sizes containing L=7, 10, 14, 20 and 25 unit cells in each direction at $\phi=0.48$. The maximum shear strain is fixed at 1.5% for all cases. The homogeneous phases (soft, $\phi=0$; and stiff, $\phi=1$), which exhibit negligible loss moduli at all frequencies, are shown for comparison. As seen from the figure, increasing system size results in the maximum G'' versus frequency curve to shift to lower frequency. Interestingly, the frequency at which loss modulus shows a peak, when plotted against the inverse of simulation cell length gives rise to a straight line with a positive slope of about 1475 m/s as shown in Figure 3.9(b). This value should be related to the speed of sound wave (c') due to propagation of shear waves in the composite. The speed of sound due to shear in the composite with $\phi=0.48$ was also computed from MD determined elastic properties using the relation $c=\sqrt{G/\rho}$ [74] was found to be 1270.1 m/s.

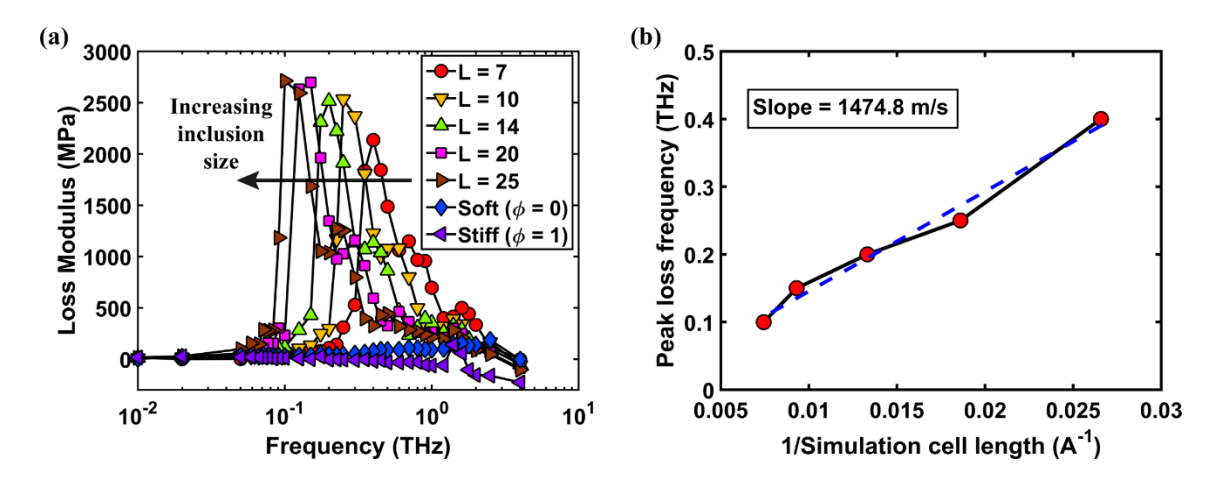


Figure 3.9: (a) Frequency-sweep simulations depicting variation of loss modulus with frequency for various system sizes from L=7 unit cells to L=25 unit cells, with the volume fraction of stiff phase, $\varphi \sim 0.48$. The homogeneous phases ($\varphi=0$ and $\varphi=1$) which exhibit negligible loss moduli are also shown for comparison. (b) Variation of peak loss frequency with inverse of simulation cell length as outlined in panel (a).

The similar values of the speed of sound and the slope calculated from maximum damping frequency versus inverse size suggests that the maximum damping corresponds approximately to the frequency of the largest wavelength sound wave representing microstructure periodicity.

3.3.4 Viscoelastic damping in crystalline superlattice structures

Superlattice or laminated structures, where usually two dissimilar materials with different mechanical properties are sandwiched together, lead to many interesting properties [75]. Skirlo et al. [76] studied viscoelasticity in model Cu-Nb superlattice structures with stepped interfaces and found that the interfacial shear modulus increases monotonically with the step density. With this motivation, we also explore damping in superlattice with alternate layers of the two components (soft and stiff) having the same thickness and equal volume fractions. Akin to our analysis with regards to the size and shear frequency effects on damping in spherical inclusion composites, we observe that superlattice structures exhibit a similar damping behavior. Figure 3.10(a) shows the *frequency-sweep* simulations for superlattice structures with varying sizes, plotted as a function of superlattice period. The sizes are such that the period of the superlattice feature (width of one layer of soft and stiff phase) is varied from L = 4 unit cells (10.8 Å) to L = 24 unit cells (64.5 Å). A snapshot of the superlattice structure with a period of 8 unit cells (21.5 Å) is shown in the inset.

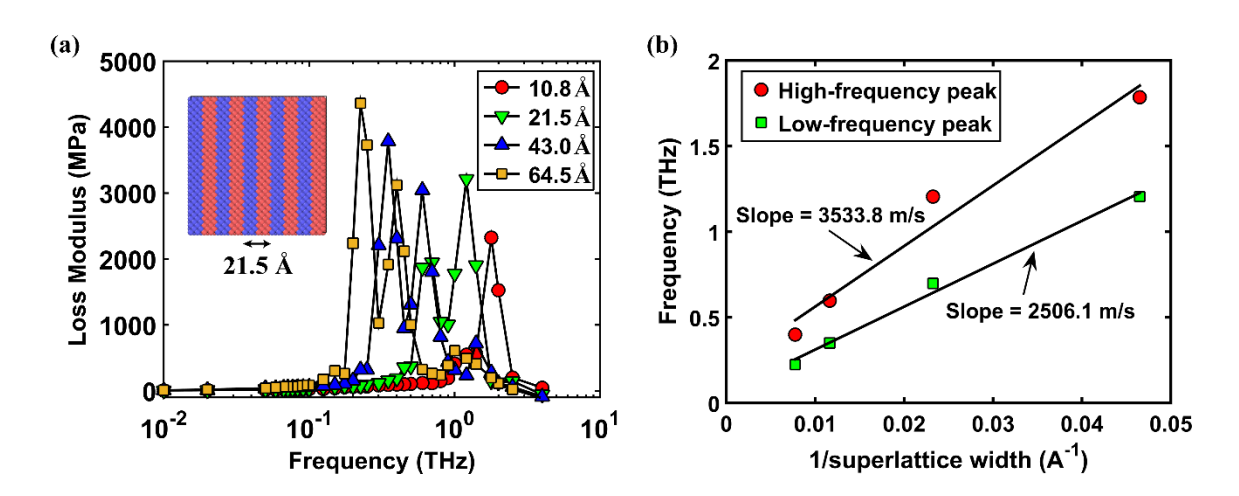


Figure 3.10: (a) Frequency-sweep simulations for superlattice structures composed of soft and stiff phases, for various widths of the superlattice spacing. (b) Variation of the two peak loss frequencies (the high and low-frequency peaks) as obtained in panel (a), with inverse of superlattice width.

As observed for the spherical inclusion composites, superlattice structures are also observed to exhibit high loss moduli at intermediate frequencies. Interestingly, we observe two pronounced peaks in the loss moduli for all sizes. We denote these as the "high-frequency" and "low-frequency" peaks just based on the frequency position. Two trends are clearly evident with respect to this characteristic damping. Firstly, as the superlattice period decreases, the low-frequency peak intensity decreases and the high-frequency peak increases. For the smallest structure (with a period of 4 unit cells), the low-frequency peak appears as a mere shoulder. This clearly shows that the low-frequency peak originates from the layering in superlattice, which disappears as the superlattice period diminishes (becomes more homogeneous). We suppose this is because of greater strains undergone by the soft phase when the superlattice period increases.

Secondly, one can observe the characteristic size-dependence for damping, in the sense that larger sizes shift the damping frequencies to lower values. We observe that both the high- and low-frequency peaks show this behavior. Figure 3.10(b) shows the variation of these two peak frequencies as a function of inverse superlattice width. We observe that the high-frequency peak has a slope of 3533.8 m/s, which is ~1.4 times larger than that of the low-frequency peak. It is possible that the two peaks relate to longitudinal and transverse vibrational modes characterized by the difference in speed of sound.

3.4 Summary and conclusions

Using non-equilibrium molecular dynamics shear simulations, we demonstrate high viscoelastic damping (manifested as large loss modulus, G'') in model crystalline composites with spherical inclusion of a stiff phase embedded in a softer matrix. These high losses are realized only for intermediate volume fractions (ϕ) of the stiff phase (0.2 < ϕ_{stiff} < 0.6) and at intermediate shear frequencies (0.3 < f < 1.5 THz) which are seen to overlap with the range of system frequencies.

In summary, we find that:

1. Viscoelastic damping has a strong dependence on the microstructure of the composite with homogeneous phases (purely soft or purely stiff) exhibiting negligibly small

loss moduli and intermediate volume fractions of the stiff phase exhibiting up to 25 times larger loss moduli than the homogeneous soft phase.

- 2. Viscoelastic damping in composites exhibits a strong shear frequency dependence. At intermediate shear frequencies, the loss modulus can increase by about two orders of magnitude. Closely associated with this frequency-dependence is the size-dependence of loss moduli. We observe that for a fixed volume fraction of the stiff phase, larger simulation cell lengths result in a linear reduction of frequency at which the peak loss modulus occurs.
- 3. We attribute the large loss moduli in composites to selectively large deformation of the soft phase. At intermediate volume fractions of the stiff phase, we observe confinement of large shear strains in the soft phase, resulting in mode-dependent Grüneisen parameters that are about 2 to 3 times larger than for homogenous soft and stiff phases respectively. The loss moduli can be up to 20 times larger than analytical upper bounds predicted by the variational theory of Hashin and Shtrikman.
- 4. We also observe high viscoelastic losses in model superlattice structures comprising of soft and stiff crystalline components that are dependent on the shear frequency and the superlattice width. In particular, we observe two peaks in the loss moduli during frequency-sweep simulations, with the low-frequency peak corresponding to the superlattice feature that diminishes as the superlattice width decreases (becomes more homogenous).

4. Frequency-dependent mechanisms for damping in alloys

In the previous chapter, we studied damping in model crystalline composites. Extending our analysis on damping in hard materials, we consider the role played by structure on damping. We perform oscillatory shear simulations to determine the loss modulus for three solids with identical interaction yet distinct structures: ordered, random and glassy alloys. The organization of this chapter is as follows: Section 4.1 introduces structure-property relations for frequency-dependent damping in hard materials. Sec. 4.2 describes simulation models used in this study and Sec. 4.3 contains detailed structural characterization for the three solids. Results are discussed in Sec. 4.4 and summary in Sec. 4.5.

4.1 Introduction

Structure has traditionally played a very important role in determining a host of material properties that can be exploited to engineer materials with novel applications. Alloys, including ordered and random alloys have been studied intensely for several decades [77], [78] and their crystal structure-property relations have been well understood in general. Equally important has been the study of non-crystalline materials (such as glasses) for a wide range of structural and other applications [79], [80]. The contrast in structure between the three classes of materials (ordered, random alloys, and glasses) confers diverse mechanical, thermal and optical properties [81].

Here, we will focus on mechanistic understanding of viscoelastic damping in alloys with various structures. Our work is motivated by the fact that frequency-dependent damping is an important materials characteristic, yet often overlooked for metal alloys. In the low frequency range, particularly in the case of soft materials, damping originates from structural relaxation, and naturally depends on the frequency [82], as typically demonstrated by dynamical mechanical analysis [83]. At the higher, up to GHz, frequencies large quality factors (low damping) are desired for micromechanical and nanomechanical resonators [39]–[41].

Portions of this chapter may appear as: R. Ranganathan, Y. Shi and P. Keblinski, "Frequency-dependent damping in alloys", unpublished.

Finally, in the THz range, which is relevant, for applications such as phononic interconnects [13], and high-frequency sound attenuation [42]–[44], damping arises from anharmonic phonon-phonon coupling [21], [84] and is in the so-called Akhiezer regime [85]. Another damping mechanisms is anelastic relaxation, which have been exploited in hydrogen-loaded bulk metallic alloys [86]–[88] to enhance the internal friction.

While structural effects on mechanical properties under constant strain or stress has been extensively studied with atomic-level simulations in crystalline materials and inorganic glasses [80], a characterization of viscoelastic damping properties by such simulations is limited. Here, we employ molecular dynamics to simulations to study viscoelasticity in materials representative of metal alloys described by the same interatomic potential, but with widely different structures.

4.2 Model structures and methodology

4.2.1 MD Model and structures

We employ the Lennard-Jones (LJ) potential to describe binary, equiatomic ordered, random and glassy alloys. The energy interaction parameter, ε and the length scale parameter, σ parametrize the interatomic energy, $E=4\varepsilon$ [$(\sigma/r)^{12}-(\sigma/r)^6$], similar to the potential used in chapter 3. The parameters used for the two components systems are: $\varepsilon_{II}=0.15$ eV and $\sigma_{II}=2.7$ Å, $\varepsilon_{22}=0.5$ ε_{II} , $\varepsilon_{I2}=1.5$ ε_{II} , $\sigma_{22}=0.91$ σ_{II} , and $\sigma_{I2}=0.95$ σ_{II} . The masses for the two species are made equal to 46 g/mol to simulate a system comparable to Ni-Nb 50-50 alloy [89], [90]. These parameters are inspired from the classic Kob-Anderson model for binary LJ glass [91], [92], with two notable differences – (a) our system is equiatomic, compared to a 80:20 atomic ratio in the original work and (b) the σ values are modified slightly, to yield stable ordered, random and glass structures for the same set of parameters. The original Kob-Anderson parametrization yields an unstable (against glass formation) random alloy phase.

The ordered structure consists of the two atom types placed in an FCC lattice in alternate basis positions. Random structure is generated from a pure FCC crystal (say, type "I" atoms) and randomly switching 50% of atoms to type 2. Glass is generated from the random phase by a melt-quench process involving heating from 300 K to 1500 K; equilibrating and quenching back to 300 K under zero hydrostatic pressure using a quench rate of 6.8 K/ps. The resultant glass structure shows no crystallization during a 11 ns constant energy and volume (NVE) simulation (see Sec. 4.3.1) and is characterized by pair correlation functions similar to the original Kob-Anderson glass [92].

Our standard simulation cell contains of 32,000 atoms in a cubic simulation cell (box length ~8.2 nm) with periodic boundary conditions applied along all three directions. Model structures were initially equilibrated at 300 K and at zero external pressure, before characterizing viscoelastic damping via non-equilibrium, oscillatory shear simulations in the NVE ensemble. All simulations were performed with a timestep of 0.44 fs using the LAMMPS simulation package [51].

4.2.2 Methodology

We follow the oscillatory shear methodology presented in chapter 2. Briefly, we apply a sinusoidal shear strain, $\gamma_{xy} = \gamma_o \sin(2\pi ft)$ at a shear frequency, f by tilting a face of the simulation cell with a maximum amplitude, γ_o of 2%. This strain is well below the elastic limit for the ordered, random and glass structures which were found to be approximately 13.2%, 9.9% and 4.2% respectively (see Sec. 4.3.3). Loss modulus is computed from the averaged stress-strain profiles (refer to chapter 2). By the end of the application of shear deformation, we observe only modest increase in temperature (maximum of ~60 K) about the starting temperature of 300 K (for comparison, the calculated melting point for ordered and random alloys is about 1100 K and the glass transition temperature calculated with a quench rate of 6.8 K/ps is 990 K; see Sec. 4.3.2). We are primarily interested in the dependence of loss modulus on the structure and shear frequency, and loss modulus is used synonymously with the damping capacity.

Sample high frequency ($f \sim 1$ THz) stress-strain data obtained from oscillatory shear simulations for all three structures are shown in Figure 4.1(a), where the stress shown is

averaged over 5 shear cycles. Atomic snapshots of a section of the simulation cell for each of the three structures are shown in Figure 4.1(b). To clearly depict the phase shift, the stress data are scaled to have the same amplitude as the strain. As observed from the figure, the glassy alloy exhibits the largest δ of 31°, random alloy has $\delta = 11^{\circ}$, while ordered structure shows negligible δ (=1°). The stress amplitude however, depends on the stiffness of the material, and as expected, shows an opposite trend, with values of 0.87 GPa, 1.3 GPa and 1.7 GPa observed for glass, random and ordered alloy structures respectively. This translates to a large loss modulus for glass (G'' = 0.45 GPa), appreciable modulus for random (G'' = 0.25 GPa) and negligible modulus (G'' = 0.03 GPa) for the ordered alloy.

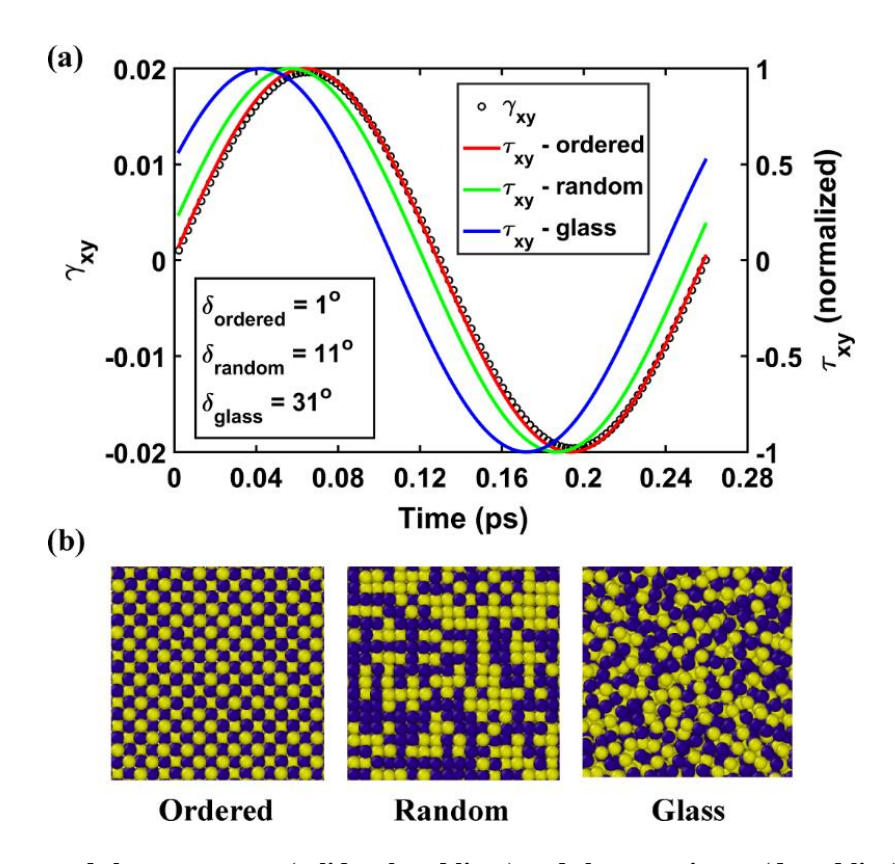


Figure 4.1: Averaged shear stress, τ_{xy} (solid, colored lines) and shear strain, γ_{xy} (dotted line) profiles for shear at frequency, $f \sim 3.86$ THz for ordered, random and glassy structures. Stress data for the three structures have been normalized to show the effect of phase shift (indicated) clearly. (b) Atomistic snapshots of the side view of a small section of system size (~3.6 nm cross-sectional length) for the three structures.

4.3 Characterization of model structures

In this section, we present a detailed characterization of the model structures obtained with the defined interaction parameters, including the glass transition temperature, melting points of ordered and random alloys and elastic properties of all three structures.

4.3.1 Structural characterization of glass

The original Kob-Andersen glass model [91] has been modified slightly to render stable phases of ordered, disordered and glassy systems with the same potential parameters. The new parameters for equiatomic glass containing two LJ atom types were described in Sec. 4.2.1. The original set of parameters yield an unstable random alloy phase (that becomes amorphous spontaneously). Moreover, we observe that the glass does not show any signs of crystallization at long time scales, as evidenced from pair correlation functions during a long NVE simulation of 11 ns, shown in Figure 4.2.

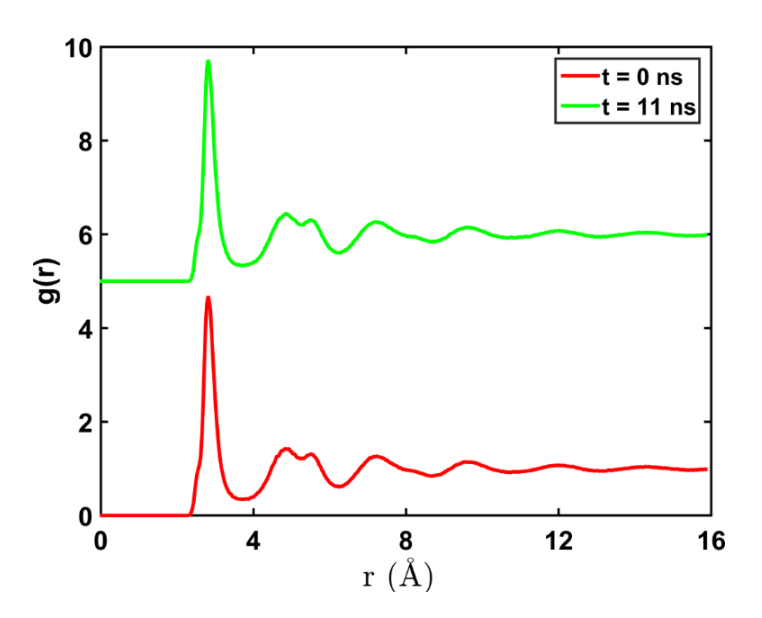


Figure 4.2: Pair correlation function for the glass model used in this work. Nearly identical plots at the beginning and end of a long NVE simulation (t = 11 ns) indicate that the glass is stable.

4.3.2 Melting points and glass transition temperature

The thermodynamic melting point for ordered and random alloys were estimated by gradually heating the solid phase in a slab geometry to mimic melting from a free surface. The solid phase was heated from T \sim 1 K to T \sim 2250 K in steps of \sim 20 K. At the end of each heating step, constant temperature equilibration was performed for about 20 ps. Shown in Figure 4.3(a) are the results for estimation of melting points. From the jump in potential energy, the melting points for ordered and random alloys are found to be in the range 1000-1200 K.

To calculate the glass transition temperature (T_g), we heat the original random alloy to 1500 K and equilibrate the melt. Following this, the melt is quenched to a temperature of 300 K under zero external pressure, with a quench rate of 6.8 K/ps as shown in Figure 4.3(b). T_g , as estimated from the intersection of tangents drawn from either ends of the volume-versus temperature profile is about 990 K.

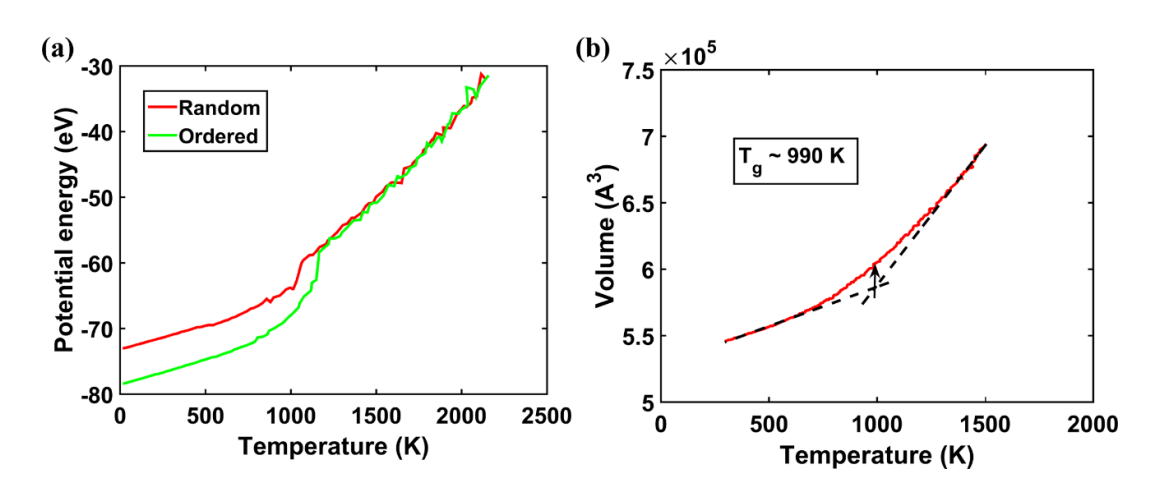


Figure 4.3: (a) Variation of potential energy with temperature during slow melting of ordered and random alloys. (b) Variation of volume with temperature during quenching of melt. Glass transition temperature is estimated to be 990 K.

4.3.3 Elastic limit for the ordered, random and glassy alloys

We estimate the extent of elastic behavior (the elastic limit) for all three structures under the application of steady state shear deformation. The normalized shear stress (τ_{xy}) and shear strain (γ_{xy}) are plotted in Figure 4.4 for a constant strain rate (= 10^{-3} ps⁻¹) shear deformation. The peak values of τ_{xy} for ordered, disordered and glass structures were approximately 12 GPa, 6.4 GPa and 1 GPa respectively. Glass is seen to exhibit significant plasticity, which is not of much concern for this work considering we apply strains (~2%) well below the elastic limit. The elastic limit was found to be approximately 13.2%, 9.9% and 4.2% for ordered, disordered and glass structures respectively.

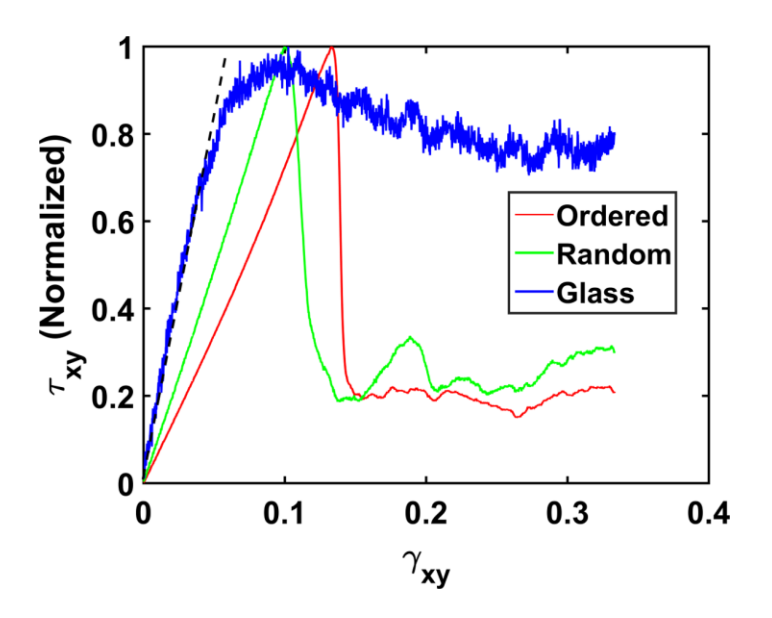


Figure 4.4: Shear-stress-shear strain plots for ordered, random and glass structures to determine the elastic limit.

4.4 Results and discussion

4.4.1 Frequency-dependence of damping

Oscillatory shear deformation has been performed over nearly five decades in frequency for all three structure. Figure 4.5(a) shows the results of *frequency-sweep* simulations. For random alloy and glass, shear stress was averaged not only over 5 cycles, but also over three independent structures for good statistics. For the ordered alloy, the averaging was performed over three orthogonal tilt systems. The first key observation is that there is a pronounced peak in damping in the random and glassy alloys in the high-frequency range, which is essentially not exhibited by the ordered alloy. Also, upon lowering of frequency, an approximate power-law behavior in the dependence of loss modulus on shear frequency is observed (see Figure 4.5(b)). Finally, in the low frequency range, loss modulus shows a constant power-law decay for ordered and random alloys, whereas in the glassy alloy, power-law scaling persists only in a limited frequency range spanning about two decades in frequency.

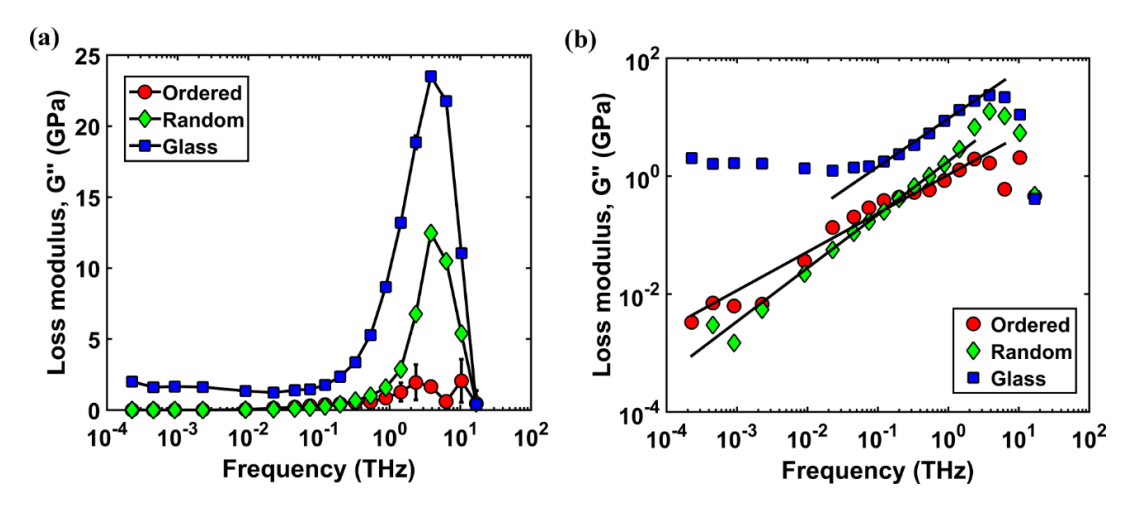


Figure 4.5: (a) Frequency-sweep simulations showing the variation of loss modulus for ordered, random and glass structures. (b) Same data as in panel (a) but in a log-log scale, depicting power-law scaling between loss modulus and frequency. Power-law scaling holds for two decades of frequency for glass, and more than three decades in frequency for random and ordered alloys.

4.4.1.1 Damping at high frequencies

In order to explain the mechanism for high-frequency damping in three structures, we first verify, by inspection, that the oscillatory deformation does not lead to any atomic rearrangements or defect formation for any shear frequency. Therefore, we argue that the damping exhibited by these structures originates from anharmonic vibrational coupling, akin to that observed previously for epitaxial composites (see Chapter 3, [57]). It is also likely that high frequency loss modulus peak in glasses has the same origin. To give more credence to this proposition, we compute the vibrational mode-dependent shear Grüneisen parameter, $\gamma_{12,i}$, which is a measure of the relative change in mode frequency, ω_i with respect to infinitesimal changes in shear strain, ε_{12} [43]. $\gamma_{12,i}$ is described according to the following equation:

$$\gamma_{12,i} = (1/\varepsilon_{12}) \,\partial\omega_i/\partial\varepsilon_{12} \tag{4.1}$$

Here, the indices I and I correspond to the component of shear stress/strain. Vibrational frequencies were computed by the method described in Sec. 2.3.1, for an undeformed, 864-atom structure (ordered, random and glass alloys) subjected to a small shear deformation. The mode-dependent Grüneisen parameters are plotted in Figure 4.6(a). We observe that γ_{12} are generally the largest for the glass structure across the whole frequency range and have noticeable values for the random alloy. By contrast, the ordered structure has negligible γ_{12} (more than two orders of magnitude lower than random alloy and glass). We also note that the range of vibrational frequencies (as shown by the vibrational density of states in Figure 4.6(b)) coincide well with the frequency range over which the peak in damping is observed, further signifying the primary reason for damping to be the anharmonicity in coupling of vibrational modes.

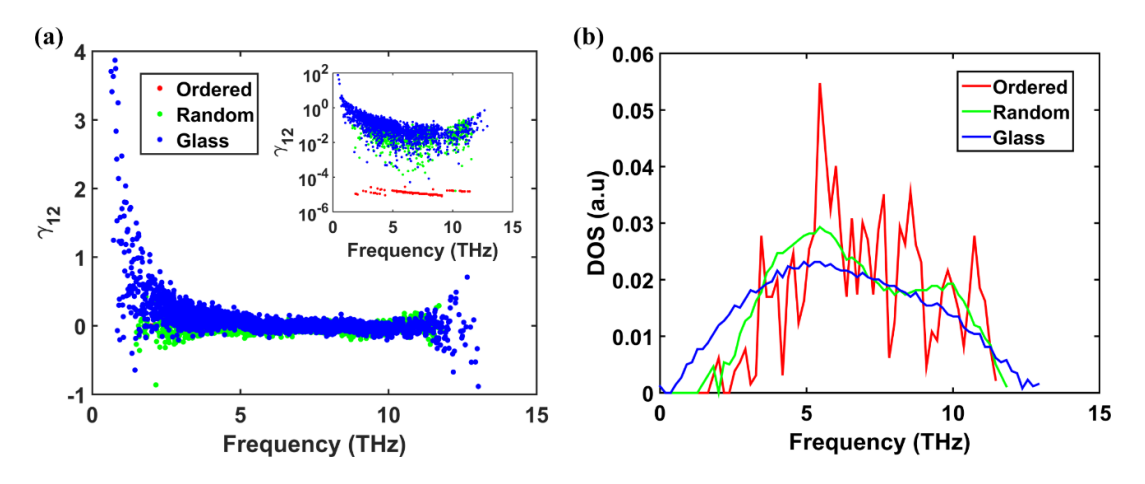


Figure 4.6: (a) Mode-dependent shear Grüneisen parameter (γ_{12}) for ordered, random and glass computed for a system size of 864 atoms (box size ~24 Å). Random alloy and glass have γ_{12} that are two to four orders of magnitude larger than ordered structure, as seen from the inset which shows the data plotted on a logarithmic scale. (b) Vibrational density of states for the three structures.

4.4.1.2 Damping at intermediate frequencies

Next, we focus on the dependence of damping on shear frequency, starting from the peak and going down in the frequency scale. We observe that the loss modulus (and the phase shift) can be well-described by a power-law behavior over different frequency windows for each of the three structures. Shown in Figure 4.5(b) are loss moduli for the three structures with power-law fits with respect to frequency, according to the equation $G'' = G''_{o}f^{n}$. For glass, we observe that power-law behavior exists only in a small frequency range (spanning 2 orders of magnitude), beyond which G'' becomes nearly constant. For ordered and random alloys, power-law scaling holds over nearly four decades in frequency. The exponents, n for ordered, random and glass alloys were found to be 0.65, 0.91 and 0.82 respectively.

It is well known that a large number of frequency-dependent responses in material property that follow some form of relaxation as a function of time, exhibit a power-law scaling. Notably, a large body of work on sound attenuation [93]–[96] and propagation of shock waves in viscoelastic materials [97] and damping in nanomechanical resonators [39]

show a power-law scaling with respect to frequency. The exponent, n for all three structures in this work are between 0 and 2, which is also what is observed for sound attenuation in a majority of materials.

4.4.1.3 Low-frequency damping in glass

Finally, we will focus on the intermediate and low-frequency damping in glass, as presented in Figure 4.5, and characterized by persistent, and even slightly increasing loss modulus with decreasing frequency. Such loss in glasses is associated with collective motion of atoms such as that associated with shear transformation zones and associated plastic deformation [49], [98]–[100]. Such local atomic motion is usually irreversible, involving pockets of local plastic behavior (so called soft-spots), which manifest as shear transformation zones during the onset of plastic deformation.

To detect and characterize such possible collective motion of atoms, we define deformation clusters as composed of atoms that are displaced by more than 1.6 Å (equal to shear amplitude) by the end of the 5-cycle deformation and any atom in the cluster has at least one "displaced" neighbor within a distance of 4.8 Å (corresponding to the first shell of nearest neighbors).

Figure 4.7 shows the distribution of soft-spot clusters for three frequencies (f = 0.45 GHz to 45 GHz) in the low frequency regime. Clusters are indexed with a cluster "number" (x-axis) according to the increasing order of cluster sizes. According to Figure 4.7, there is a clear trend of simultaneous increase in both cluster sizes and the number of clusters, with decreasing shear frequency. This frequency-dependent cluster size distribution could arise from two possible sources – either, (a) at lower shear frequencies, the mechanism of dissipation could be dominated solely by structural rearrangements, which leads to a frequency-dependent soft-spot distribution, or (b) the larger amount of physical time spent during deformation for a given number of cycles could lead to larger soft-spots at lower frequencies (an effect similar to aging in glasses [101], [102]).

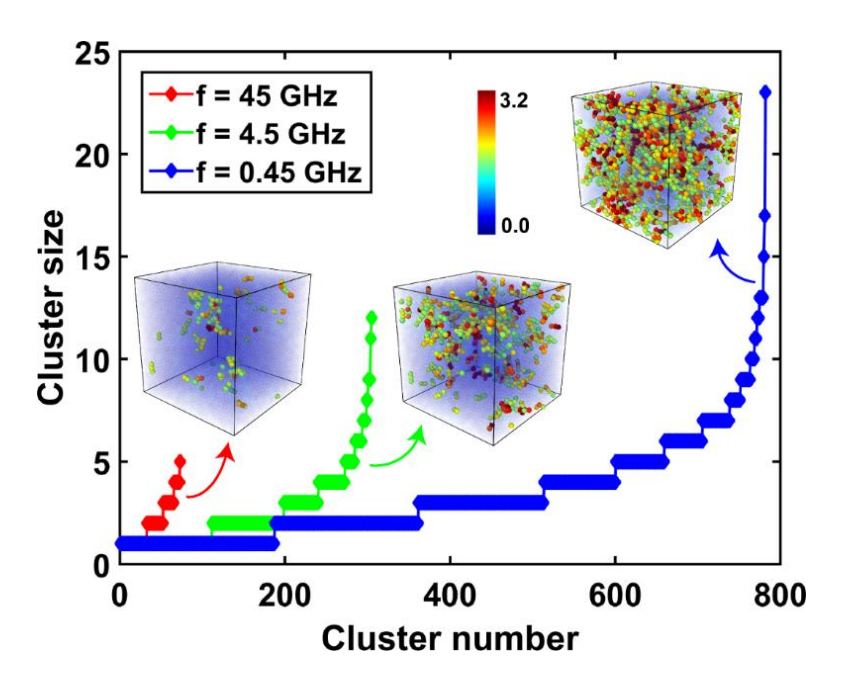


Figure 4.7: Evolution of cluster size distribution at the end of five cycles of shear of glass, for three shear frequencies in the low frequency regime. Cluster size (y-axis) is the number of atoms forming the soft-spot and the cluster number (x-axis) is just an index of each cluster sorted by ascending order of cluster sizes. Also shown are snapshots of atomic regions forming the clusters, color-coded according to their atomic displacement with respect to the initial, undeformed state. Snapshots are generated using the OVITO visualization tool [103].

To understand the reason behind frequency-dependent distribution of soft-spots more clearly, we perform oscillatory shear simulations at various frequencies where the total simulation time is kept constant. These simulations are performed under constant volume, constant temperature (NVT) conditions. Coupling to a thermostat (Nose-Hoover [70], [71] in this case) was necessitated by the need to prevent significant temperature rise during shear at high frequencies over long time-scales. The total time simulated is 11 ns, which corresponds to a total of 5 shear cycles at the lowest frequency ($f = 4.5 \times 10^{-4}$ THz) and over 100,000 cycles at the highest frequency (f = 10.3 THz).

Shown in Figure 4.8 are the cluster distribution characteristics in these NVT shear simulations. Panel (a) shows the distribution of cluster sizes sorted according to size, for a wide range of shear frequencies. We observe a clear trend for increasing cluster size and number of clusters as frequency is lowered. In some sense, the shear agitation activates different shear transformation zones, depending on the frequency of agitation.

Additionally, in Figure 4.8(a), we show cluster distribution for the "no-shear" case, where we ascertain atomic motion arising solely from aging, as a reference. Interestingly, the no-shear case exhibits cluster statistics intermediate to those characterizing low and high frequency shear. This is particularly apparent in Figure 4.8(b), where the average cluster size and total cluster volume is plotted as a function of frequency, for clusters larger than 4 atoms and data for no-shear case are represented as dashed lines. Data are averaged over five independent samples to ensure good statistics. We observe a sharp increase in both cluster size and cluster volume around 1 THz, followed by a weak frequency-dependence as frequency is lowered.

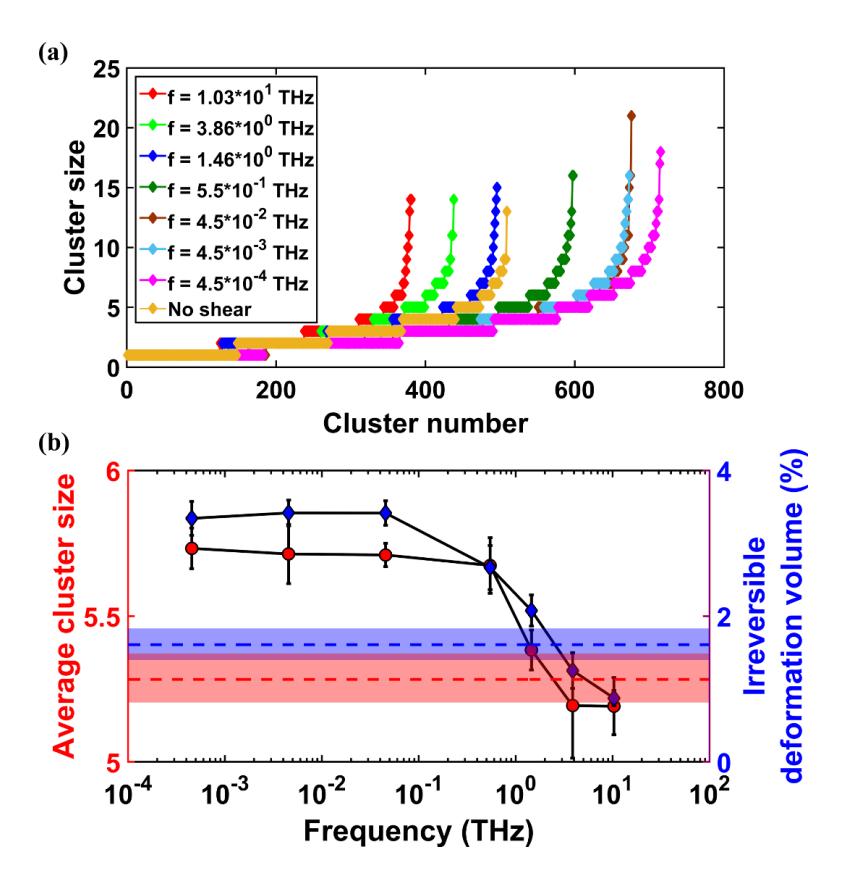


Figure 4.8: Evolution of cluster sizes for oscillatory shear simulations run for a constant time (about 11 ns) instead of constant number of cycles as shown in Figure 4.7. (a) Distribution of cluster sizes for various frequencies for a single glass sample. (b) Variation of average cluster size and percentage of atoms that contribute to irreversibly deformed clusters with frequency. The corresponding average size and deformed volume for the "no shear" case are indicated by dashed lines, with the range of error bars depicted by transparent colored bands.

It is interesting to note that the threshold frequency occurs in the range of the peak damping frequency. This shows that the two primary channels for damping, namely, vibrational anharmonicity and structural relaxation, operate at distinct frequency regimes.

4.4.1.4 Stress relaxation in glass

An effect concomitant with the low-frequency local deformation in glass is likely to be significant structural relaxation. A metric for probing structural relaxation (accompanying atomic motion) during low-frequency shear of glass, is the relaxation of shear stress from an initially sheared state. Shown in Figure 4.9 is the relaxation of normalized shear stress (τ_{xy}) from an initially deformed state (with shear strain of 2%) during an NVE simulation of 3.5 ns, for all three structures. As seen from the figure, glass exhibits significant stress relaxation (~56%) which is an indication of additional damping at low-frequencies, arising from atomic motion. Ordered and disordered structures maintain perfect crystallinity and do not show relaxation.

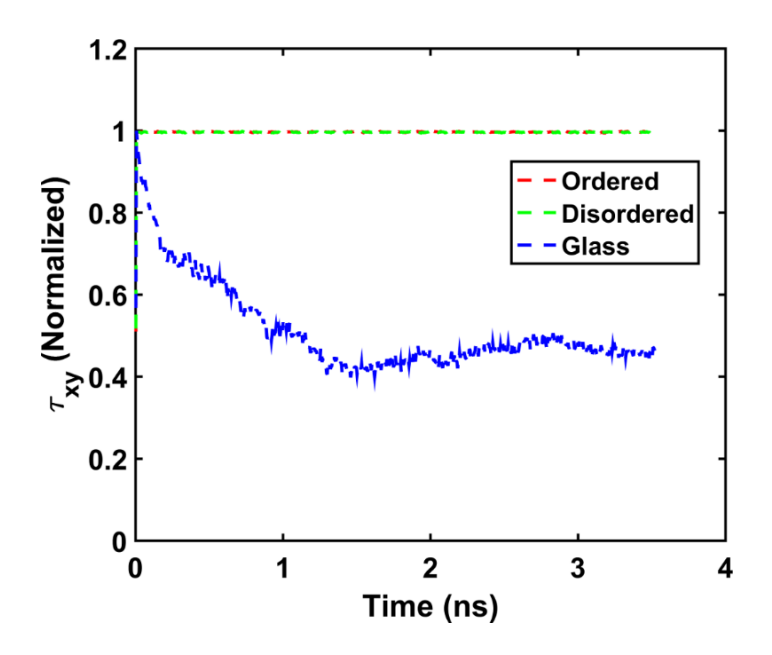


Figure 4.9: Relaxation of normalized shear stress, τ_{xy} starting from an initially stressed state, for the three systems considered (ordered, disordered and glass).

4.4.1.5 Comparison with constant shear-rate deformation

The results described in the previous sections strongly indicate that low frequency agitation of the glass structure enhances structural relaxation via local clusters that undergo irreversible deformation, while agitation at higher frequency suppresses this phenomenon. The nearly-invariant cluster size distribution with frequency describes the qualitative variation of loss modulus for glass in the low-frequency regime. Moreover, the clusters observed originate in a random manner and there is less than 10% overlap between atoms contributing to clusters observed at any two randomly chosen frequencies. Our proposition is that such a mechanism for enhanced local deformation at lower frequencies is a direct consequence of larger time per cycle for local atomic motion at lower frequencies, similar to the phenomenon in low-frequency fatigue of bulk metallic glass [100]. This is further corroborated via constant shear-rate simulations at a range of shear rates corresponding to those for the oscillatory deformation.

In addition to oscillatory shear deformations that show frequency-dependent activation of deformation cluster sizes and cluster volume, constant-rate shear deformation at a range of strain rates exhibit a time-dependent evolution of soft-spots. Figure 4.10 shows the fraction of deformed volume (soft-spots) as a function of time, for strain rates that correspond to the same set of rates during oscillatory shear deformations. Data are averaged over 5 independent samples for good statistics. The maximum shear strain at each rate is set equal to 0.1. A clear trend for larger rates (lower deformation time) suppressing cluster formation akin to oscillatory shear deformation is clearly evident.

Secondly, we observe that the deformation volume for all rates collapse on to the curve for "no shear" case and on to each other for low values of strain, and begin to deviate at larger strains. The approximate strain at deviation from the "no shear" curve for the four lowest strain rates is plotted in the inset in Figure 4.10 and shows the deviation sets in approximately at a small window of strain between 0.2 and 0.4%. This further ties well with the oscillatory shear damping results in that, the inverse relation between the time for formation of deformation clusters and strain rates gives rise to a nearly-invariant loss modulus below a certain threshold frequency.

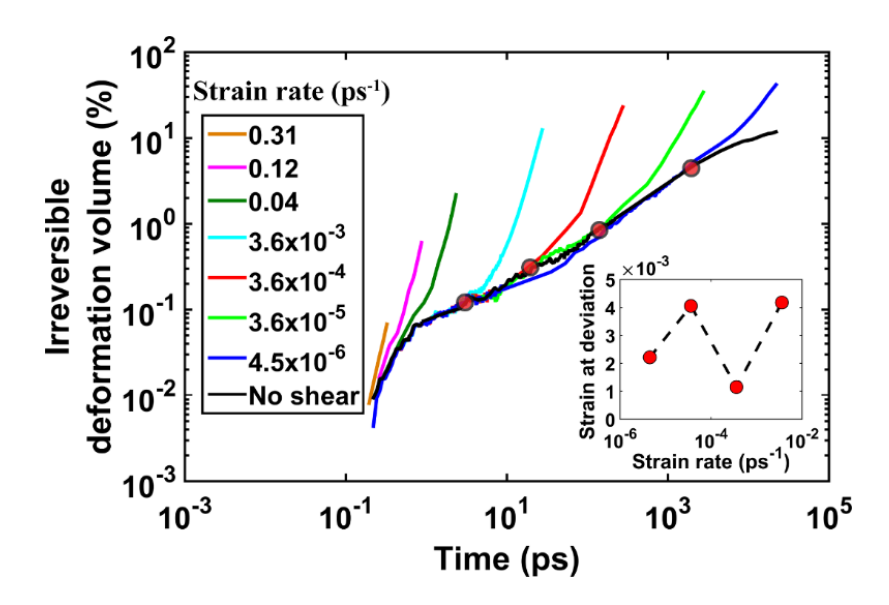


Figure 4.10: Variation of deformation volume as a function of time, for various strain rates during constant-rate shear deformation. The maximum shear strain for each case is 0.1. Also shown in black is the case for "no shear". The strain at which the four lowest frequencies depart from the curve for "no shear" (indicated by red circles) are plotted in the inset. Data are averaged over 5 independent samples.

4.5 Summary

In this chapter, we elucidated mechanisms of viscoelastic damping in three structures with stark contrast in structure – ordered, random and glassy alloys, using non-equilibrium oscillatory shear molecular dynamics simulations. Distinct differences in frequency-dependent damping characteristics were observed for these structures. Our key findings are:

1. At high frequency (of the order of THz), the large anharmonicity in coupling of vibrational modes as evidenced by large shear Grüneisen parameters, leads to a pronounced peak in damping for random alloy and glass, with glass exhibiting a much broader and taller peak.

- 2. For frequencies below the peak damping frequency, we show that the loss modulus and phase difference can be well-described by a power-law behavior, over a different frequency range in each of the three structures. Ordered and random alloys exhibit power-law scaling over nearly four decades in frequency, down to the lowest frequencies considered. Glass, on the other hand, shows this scaling behavior over about 2 decades in frequency, following which, it transitions into a nearly-constant damping regime with respect to frequency.
- 3. This finite damping at intermediate and low frequencies exhibited by glass arises from local irreversible deformation of atomic clusters (denoted as soft-spots). We show that the cluster size and volume fraction show a characteristic frequency-dependence. There appears to be a threshold frequency below which, there is an activation of soft-spots. We conclude that at high frequencies where anharmonic vibrational coupling is the dominant damping mechanism, cluster formation is naturally suppressed.

5. Commonalities in frequency-dependent viscoelastic damping in glasses

In this chapter, we use the non-equilibrium molecular dynamics oscillatory shear methodology to study frequency-dependent viscoelastic damping in a wide range of glasses. Section 5.1 gives an introduction on the history of development of various structural glasses and structure-property relations relevant for damping applications. This is followed by description of model structures in Sec 5.2 and results for various factors that influence the damping characteristics in the Cu-Zr bulk metallic glass (BMG) system in Sec 5.3. A critical comparison of damping in various glasses with a view to uncover commonalities in damping is presented in Sec 5.4 and finally, Sec 5.5 summarizes our findings.

5.1 Introduction

Although glasses have been used for a variety of applications for centuries, the discovery of bulk metallic glass (BMG) by Duwez and co-workers [104] and subsequent efforts in engineering processing techniques and compositional studies have led to a number of structural applications [79], [80], [105]. A crucial aspect in this development has been the progress in the study of structure-property relations in glasses [106]–[110], understanding of which has led to glasses with exceptional mechanical properties such as enhanced plasticity [111]–[113], strength [112], [114] and fracture toughness [115].

Glasses are also candidate materials for applications in mechanical damping. In this context, two predominant mechanisms for damping are relevant – (a) damping via anelastic relaxation and (b) viscoelastic damping. The former involves diffusion of species such as hydrogen trapped within glass, and has been used in tuning damping properties of hydrogen-loaded bulk metallic glasses [86]–[88]. The second mechanism forms the basis of this work and has its origin in atomic-level interactions and structural features that lead to an out-of-sync relation between stress and strain under cyclic deformation.

Portions of this chapter may appear as: R. Ranganathan, Y. Shi and P. Keblinski, "Commonalities in frequency-dependent viscoelastic damping in glasses", unpublished.

These mechanisms are strongly dependent on the applied shear frequency (or rate). Widely different mechanisms are usually at play while contributing to damping at different frequencies [46], [57], [116] and have been extensively studied for polymeric systems [117]. However, a mechanistic understanding of damping in inorganic glasses and possible avenues in which it can be tuned is currently lacking.

At low frequencies, glasses exhibit structural relaxation over long time-scales, with the extent of relaxation being determined by the frequency [82]. At larger frequencies (approaching GHz and THz), damping properties are important for applications such as phononic interconnects [13] and sound attenuation [42]–[44]. The role of anharmonic vibrational coupling in high-frequency damping of glasses needs to be explored.

Experimentally, direct measurement of viscoelastic damping is done via the dynamical mechanical analysis [83]. In this technique, cyclic loading in the form of an oscillatory torque is applied to probe the stress-strain response to determine the complex modulus. Forces are applied either mechanically (routinely employed for studying soft matter [117] and sometimes for hard materials [32], [118]) where typical frequencies are limited to a ~ 100s of Hz, or via electromagnetic forces [24], [36] to attain larger frequencies (~ 10⁴ Hz).

At even higher frequencies approaching vibrational frequencies (in the THz range), characterizing mechanical response becomes experimentally unattainable. However, two common experimental techniques that can be used to study mechanical relaxation at high frequencies via photon-phonon scattering processes include inelastic x-ray scattering (IXS) and Brillouin light scattering (BLS). IXS has been used extensively to measure sound attenuation coefficients [119]. Using BLS, one can typically measure elastic constants including shear modulus from phonon velocities and obtain the so called acoustic phonon damping parameter from the spectra [120]–[122]. However, extending this to quantify dynamic mechanical damping from these techniques is not straightforward. In this context, molecular-level simulations are extremely useful to study viscoelastic damping over a wide range of shear frequencies. In particular, molecular dynamics deformation studies have been used extensively [110] to study mechanical properties including tensile [123], [124] and compressive deformation [125], indentation [90] fatigue [100] and plastic deformation under shear [49], [126].

In this chapter, we extend the oscillatory shear molecular dynamics simulations previously employed to study frequency-dependent viscoelastic damping in crystalline composites (chapter 3) and binary alloys including glasses (chapter 4), to study mechanisms behind frequency-dependent viscoelastic damping in various model glasses.

5.2 Simulation methodology and model structures

Oscillatory shear simulations were employed to study viscoelastic damping in model glass structures. Our typical simulation protocol consists of oscillatory shear over 5 cycles under constant volume (NVE) condition to compute the averaged loss modulus, $G'' = G \sin(\delta)$. The temperature at the start of shear simulation is typically fixed at about 35% of the glass transition temperature (T_g). A consequence of the shear process is dissipation of heat that leads to an increase in temperature; in our simulations, we observe only modest temperature rise, to the extent of a few percent for an extended range of shear frequencies. As we shall show later, in a narrow region of frequencies in the high-frequency regime (of the order of a few THz), a pronounced peak in damping is observed, that could lead to a temperature increase by ~25% in some glasses. However, we note that this is still well below the T_g and hence, possible effects on softening effects due to shear are minimal. We also consider cases where we characterize damping for a constant amount of time as opposed to constant number of cycles, at different frequencies. In this case, the system is coupled to a Nose-Hoover thermostat [70], [71] to prevent high temperature rise over long time scales, especially at high shear frequencies.

Shear frequency is varied over 5 decades (ranging from 10s of MHz to 10s of THz) where we uncover disparate mechanisms for damping at high and low frequencies. Figure 5.1 shows sample stress-strain results averaged over 5 cycles of shear for the Cu-Zr BMG system at two shear frequencies (f = 2 THz and f = 0.02 THz), exhibiting markedly different δ and G''. Atomic snapshots at shear strains corresponding to zero, maximum and minimum shear strains are shown as insets (the tilt factors are exaggerated for clarity).

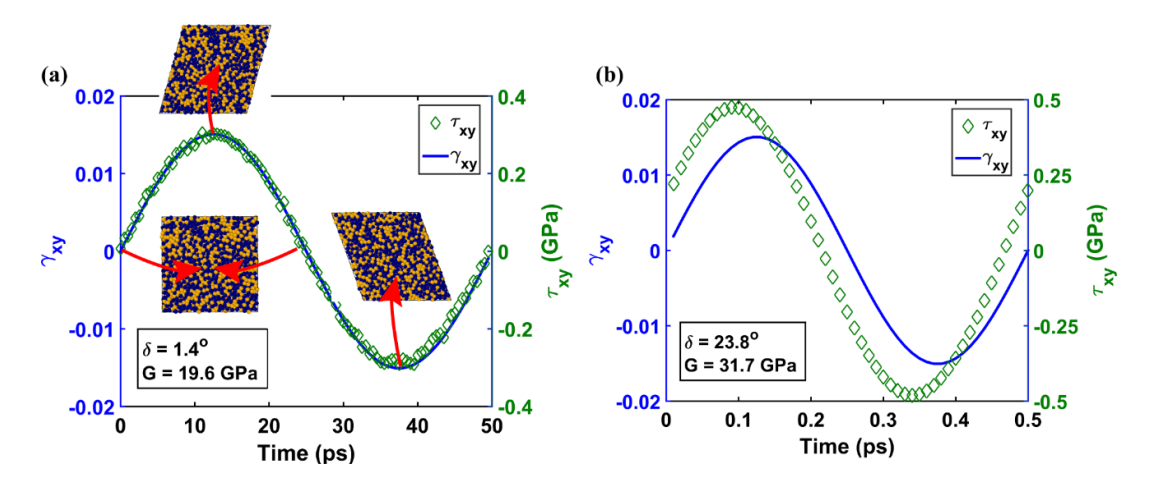


Figure 5.1: Typical stress-strain response for model Cu-Zr bulk-metallic glass at (a) f = 2 THz, showing a large phase difference, and correspondingly, high loss modulus, and (b) f = 0.02 THz, showing low phase difference and low loss modulus. The peak shear modulus is also noted.

5.2.1 Model structures

We study viscoelastic damping in five model glasses, namely, (a) Cu-Zr BMG [127], (b) Dzugutov glass [128], (c) amorphous silicon (a-Si), (d) Wahnström glass [129] and (e) amorphous silica. All the glasses have been studied extensively in literature and have been used as models for understanding structure-property relations in glasses and studying mechanical properties [110], [123], [130]–[132]. We generate the starting glass structures by quenching the melt under zero external pressure using the Nose-Hoover barostat [133]–[136]. For each structure, we allow at least 100 ps for equilibration at the molten state and then quench the melt with a rate Q. The values of Q usually attainable in computer simulations are orders of magnitude larger than in experiment and are typically in the range of 10^{10} to 10^{14} K/ps [127], [137]–[140]. For the BMG system, which forms our baseline for a study on various factors affecting the damping characteristics, we additionally employ various quench rates to study the effect of quench rate on damping as described in Sec. 5.3.1 and Sec. 5.3.2.

For each glass, the choice of force-field describing the interaction energy, the timestep, the quench rate, the T_g , the system size and a few mechanical properties relevant for characterizing damping are listed in Table 5.1. T_g is estimated from the change in slope of volume as a function of temperature during the quench, with the quench rates Q indicated. We use periodic boundary conditions along all three axes to simulate bulk properties. The final structures are metastable glasses characterized by well-defined pair correlation functions consistent with literature. All simulations were performed with using the LAMMPS simulation package [51].

Table 5.1: Simulation details and material properties for the glass models studied

Model/system	Cu-Zr BMG	Dzugutov*	a-Si	Wahnström**	Silica
Potential	EAM [127]	Dzugutov [128]	Tersoff [141]	LJ [129]	BKS [142], with Wolf summation [143] (electrostatics)
Time step (fs)	2	10.8	0.5	0.46	1.6
T _g (K)	815	418	1100	1000	2430
Quench rate (Q, K/s)	8.5x10 ¹¹	1.83x10 ¹¹	$3x10^{13}$	8.26x10 ¹²	9.8x10 ¹²
Shear temperature (K)	300	174	540	274	900
Shear modulus (G, GPa)	18.38	3.34	34.1	20.13	35.3
Elastic limit	4.9%	5.9%	12.9%	6.56%	14.2%
Applied strain (oscillatory shear)	1.5%	1.81%	3.95%	1.99%	4.36%
System size (# atoms)	16,384	27,000	27,000	32,000	24,000

*For the Dzugutov glass, the fundamental length and time scale correspond to $\sigma = 3.4$ Å and $t_o = 2.16$ ps [144] and we set the energy parameter $\varepsilon = 0.1$ eV to scale to physically relevant scales. **For the Wahnström glass, these constants correspond to $\sigma_{22} = 2.7$ Å, $t_o = 0.46$ ps and $\varepsilon_{22} = 0.16$ eV that correspond to a model 50-50 Ni-Nb bulk metallic glass [89], [90].

5.3 Damping in BMG

In this section, we focus on viscoelastic damping in the 1:1 atomic ratio Cu-Zr BMG system, with an emphasis on understanding the key factors that affect damping. These include the effect of quench rate used in generating the glass, the interplay between quench rate and cycle-dependent damping, the effect of shear amplitude and finally, the shear temperature. For each case, we perform "frequency-sweep" oscillatory shear simulations over multiple decades in frequency.

5.3.1 Frequency-dependent loss moduli

Frequency-sweep simulations to study the frequency dependence of loss moduli (G'') were carried out for BMG quenched at multiple quench rates. Figure 5.2 shows the variation of G'' with frequency at T=300 K. We observe a characteristic peak in damping in the high-frequency regime (of the order of a few THz), as previously demonstrated in the model Lennard-Jones glass described in chapter 4. As we shall show in detail later (Sec. 5.4.1), the origin of this peak lies in the anharmonic coupling between various vibrational modes of the glass. Interestingly, we observe that the peak amplitude does not depend on the quench rate, while the intermediate and low-frequency regimes show a strong quench rate dependence. The likely explanation for this observation is that the degree of anharmonic coupling (as characterized by mode-dependent Grüneisen parameter) is rather insensitive to the quench rate. In other words, the shear frequency in this regime is large enough to overwhelm differences in damping due to rate of structural changes imposed by the quench rate.

With decreasing frequency, damping decreases initially following an approximate power-law scaling with frequency, followed by nearly frequency-independent damping. However, the extent of damping in the intermediate and low frequencies (extending down to 50 MHz) shows a strong dependence on quench rate – larger quench rate exhibits larger damping (seen more clearly in inset of Figure 5.2). Finite damping in glasses at low frequencies is a consequence of long time-scale structural relaxation and associated local

deformation as already discussed in chapter 4. Similar persistent damping in the BMG system, combined with the dependence on quench rate strongly indicate that larger quench rates lead to more metastable glasses with shallower energy minima, consequences of which are greater structural relaxation and enhanced damping.

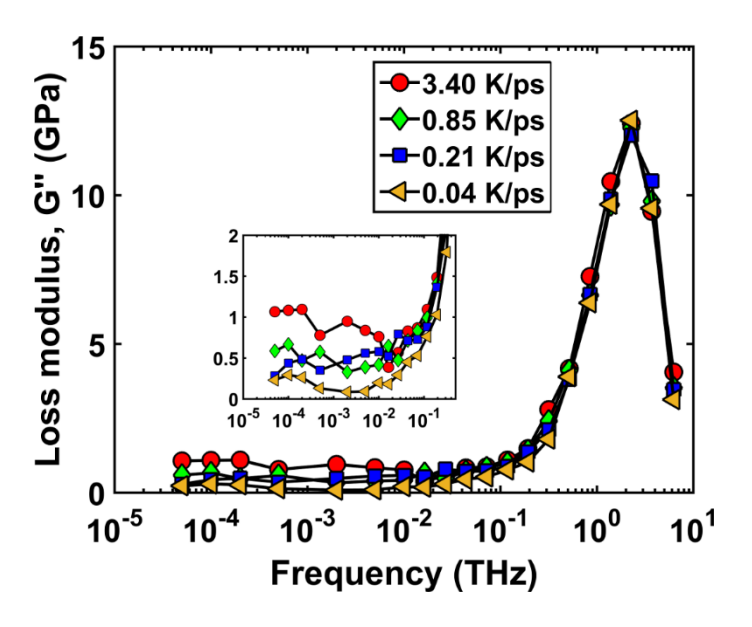


Figure 5.2: Frequency-sweep simulations depicting the variation of loss modulus with shear frequency for the Cu-Zr BMG system. Response for four different quench rates are shown. The characteristic peak in the high-frequency regime overlap for all quench rates. Low-frequency damping is affected by the quench rate, with larger quench rates resulting in larger damping. Inset shows the portion of the low-frequency regime magnified.

5.3.2 Dependence of damping on number of shear cycles

In our oscillatory shear simulations, a primary concern is the variation of calculated loss moduli with the number of shear cycles. This is particularly of interest for glasses due to their metastability. It is expected that atomic rearrangements with multiple cycles of shear could result in damping that could potentially be dependent on the number of shear cycles, N_{cycles} . We ideally desire a structure that does not exhibit significant cycle-dependent damping, in order to keep our simulation times tractable, especially at low frequencies.

To examine this effect, we study the dependence of loss modulus on N_{cycles} for the four quench rates described in the previous section.

Shown in Figure 5.3 are the results for damping at two frequencies, f = 0.5 THz and 0.5 GHz, over multiple shear cycles. We perform these simulations at constant temperature (NVT) of T = 300 K to prevent abnormal structural rearrangements due to temperature rise. We observe that the fastest quench rate (Q = 3.4 K/ps), being the most metastable, results in damping that varies strongly with N_{cycles} , especially in the initial stages.

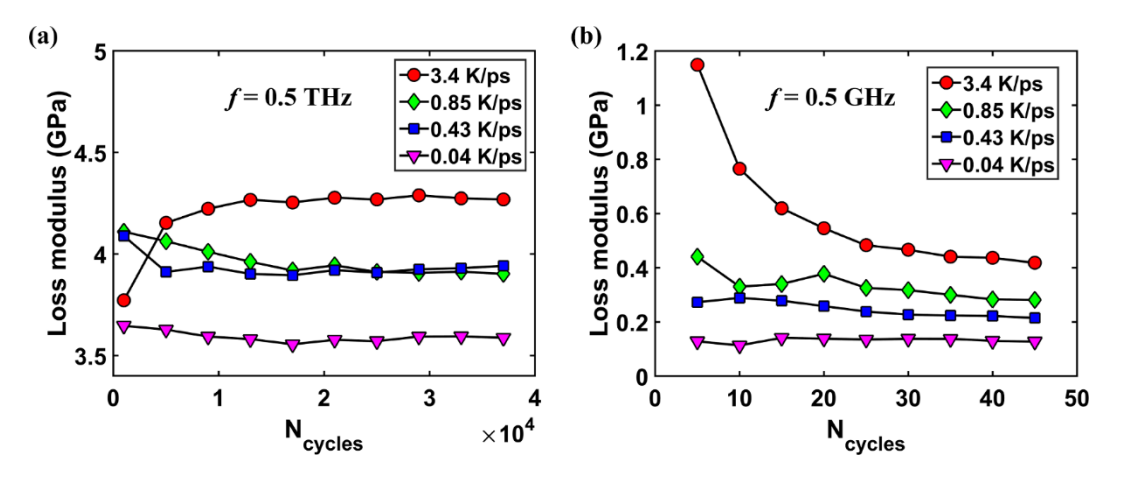


Figure 5.3: Effect of aging on the computed loss modulus for glasses quenched at various rates. Aging in glass leads to estimated properties that are dependent on the number of shear cycles; this is effect is probed by varying the number of shear cycles (N_{cycles}) for each quench rate. Shown in (a) and (b) are data for two widely different shear frequencies (f = 0.5 THz and f = 0.5 GHz respectively). Simulations performed under NVT conditions at a temperature of 300 K. The quench rate used for the bulk of the analysis pertaining to the BMG, namely Q = 0.85 K/ps shows fairly cycle-independent damping.

For glasses quenched with Q=0.85 K/ps and lower, we observe fairly cycle-independent damping. We note that such cycle-independent damping is also exhibited at other frequencies and we just show two frequencies here for illustrative purposes. For all our further analyses, we use the structure quenched at Q=0.85 K/ps.

5.3.3 Effect of shear amplitude

Under oscillatory shear deformation, the extent of shear amplitude determines the nature of viscoelastic response in the material. Typical viscoelastic materials exhibit a "linear" viscoelasticity up to certain amplitude, beyond which the response becomes "non-linear". The linearity in this context refers to the dynamical shear modulus (either G' or G'') being invariant with respect to the shear amplitude. This is a routine analysis in the field of dynamical shear experiments, especially in the field of soft matter such as polymer composites [117] where, the strain amplitude determines whether the shear falls under the so-called Small Amplitude Oscillatory Shear (SAOS) or Large Amplitude Oscillatory Shear (LAOS) regime. SAOS corresponds to a linear viscoelastic response while LAOS gives rise to non-linearity [117].

In our simulations, we check for linearity in viscoelastic response by monitoring the dependence of G'' on the shear amplitude. Very low strain amplitudes result in poor signal to noise ratio for the estimation of G'', especially at low frequencies. Figure 5.4 shows the variation of G'' with strain amplitude for four frequencies separated by an order of magnitude from each other. Simulations are performed at 300 K under NVE conditions. As seen from the figure, non-linearity in the response begins to set in at shear strains, $\gamma_{xy} > -0.04$, which is also close to the elastic limit for this system (refer to Table 5.1). We thus choose a value of $\gamma_{xy} = 0.015$ (or 1.5%) in all our shear simulations in the BMG system to ensure good signal-to-noise ratio and to simultaneously operate within the linear viscoelastic regime.

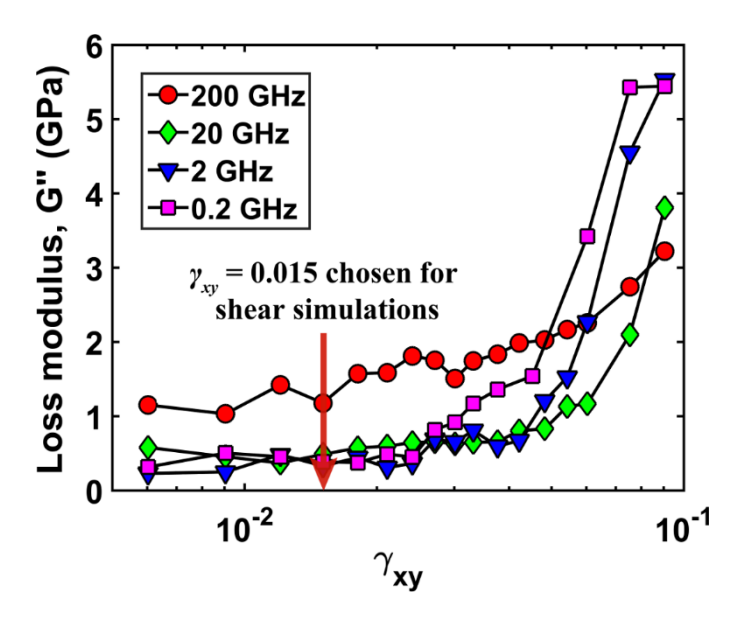


Figure 5.4: Effect of shear strain amplitude on viscoelastic response in BMG. Loss modulus is estimated for four different shear frequencies spanning four orders of magnitude. Significant non-linearity in the response is observed at strain amplitudes, γ_{xy} larger than about 0.04 (or 4%).

5.3.4 Effect of shear temperature

The predominant role played by temperature in viscoelastic response is softening of the material, leading to more viscous character. We quantify this effect via *frequency-sweep* simulations at various temperatures. Figure 5.5 shows the variation of loss modulus with frequency for temperatures ranging from 30 K to 800 K. We note that the T_g for the glass is ~815 K. We observe that the high-frequency peak is almost invariant with respect to temperature. This is not surprising since this corresponds to frequencies in the range of thermal vibrations, where the damping mechanism is due to anharmonic coupling of vibrational modes (see Sec. 5.4.1 for discussion on the role of vibrational modes). It has been shown that the Grüneisen parameter [73], which is a measure of the anharmonicity in coupling of modes, is only weakly dependent on temperature for oxides [145], [146] and we suppose that is the case for our system as well. The softening at higher temperatures lowers the high-frequency modulus marginally.

Upon lowering frequency however, we observe a marked difference in damping. This is a consequence of a larger viscous character at higher temperatures, with associated increase in the phase shift. At 800 K (very close to the T_g), we observe that at the lowest frequency ($f = 5 \times 10^{-4}$ THz), the loss modulus begins to drop with frequency; here, although the phase shift increases with lowering frequency, the shear stress begins to drop as well (due to softening).

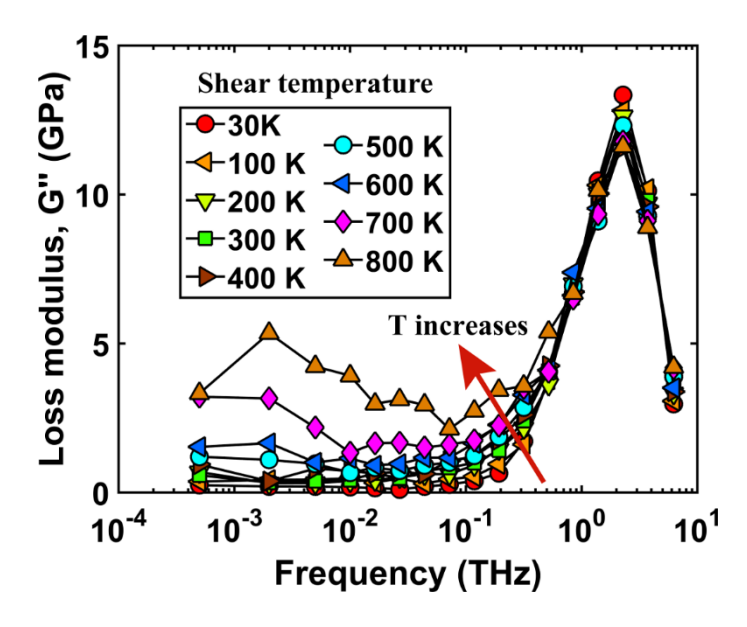


Figure 5.5: Frequency-sweep simulations to study the effect of shear temperature on damping in BMG. The maximum temperature (800 K) is just below the T_g for the BMG, which is ~815 K.

5.4 Commonality in damping mechanisms in glasses

The frequency-dependent damping characteristics in the BMG system, namely, the high-frequency peak (in the THz regime) and persistent damping in the low-frequency regime was also observed for the model binary glass discussed in chapter 4. This observation leads us to ask the following question – "are the characteristics of viscoelastic damping in glasses more universal in nature and can be understood mechanistically for a wide variety of inorganic glasses?". With this goal in mind, we extend our work to study damping in four other glasses – (a) Dzugutov glass, (b) amorphous silicon (a-Si), (c) the

Wahnström glass and (d) amorphous silica. We perform oscillatory shear deformation simulations at frequencies similar to the case of the BMG system, to look for typical characteristics in the frequency-dependent damping.

Shown in Table 5.1 is the list of simulation details, the potential used for describing interactions and various system properties relevant for this work, for all the glass models. We note that we consider both unary (the Dzugutov glass and a-Si) and binary glasses (Wahnström and amorphous silica), in addition to the BMG glass discussed so far, which forms the baseline for our comparison. The two most important factors to be considered while comparing the damping properties between various glasses are the elastic limit and the glass transition temperature (T_g). The former affects the linearity in viscoelastic response (as discussed in Sec. 5.3.3) and the latter determines the relative scaling between the temperature of shear and T_g , around which significant softening occurs (see Sec. 5.3.4). Thus, to maintain similar shear conditions across all glasses, we set the shear strain and temperature for the BMG system as the baseline and scale the strain and temperature of the remaining four glasses based on their individual elastic limits and T_g . The scaling is such that the same ratio for {strain / elastic limit} and {temperature / T_g } is used for all the glasses. These values are also given in Table 5.1

Figure 5.6 shows the comprehensive damping data from *frequency-sweep* simulations for all the five glasses. The loss modulus is shown normalized by the maximum loss modulus of each glass, to capture qualitative trends in damping across all glasses. As seen from the figure, a striking commonality in the damping characteristics is observed – firstly, in the high-frequency regime (ranging from \sim 0.1 THz to 10s of THz), all glasses show a pronounced peak in damping. With decreasing frequency starting from the peak, G'' decreases as an approximate power law over an intermediate frequency window (refer to chapter 4) for all glasses. Lastly, with further reduction in frequency, a persistent (weakly increasing) damping is observed in all glasses, extending into the MHz regime. The extent of damping in the low frequency limit (as shown clearly in the magnified portion in inset) is however dependent on the nature of glass – stiffer glasses such as silica and a-Si exhibit comparatively lower normalized G''. We note however, that the absolute magnitudes for silica and a-Si are larger than the other glasses, owing to a higher shear modulus. The mechanisms behind the damping characteristics are discussed in the following sections.

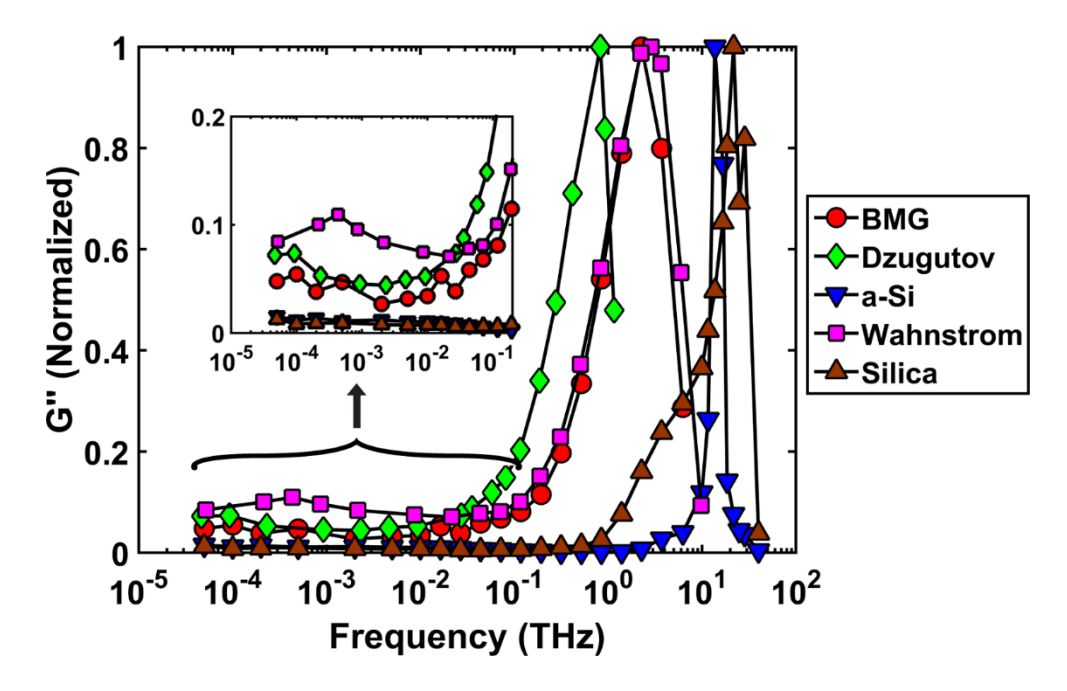


Figure 5.6: Frequency-sweep simulations for the five glass structures considered in this work. For each glass, we show the dependence of loss modulus (normalized by the maximum in G'') as a function of shear frequency. All glasses show a characteristic peak in the high-frequency regime and a nearly-invariant, finite damping in the low-frequency regime (See inset for the magnified portion of the low-frequency regime). Stiffer glasses such as a-Si and Silica exhibit larger absolute G'' in the high-frequency regime and a smaller, albeit non-vanishing normalized G'' in the low-frequency regime.

5.4.1 Role of vibrational coupling in damping

We have previously shown that enhanced damping at frequencies in the range of natural vibrational frequencies of the material is a direct consequence of large anharmonicity in the coupling between vibrational modes in glass (Chapter 4, Sec 1.3.1.1). The predominant vibrational modes in glasses, denoted as "diffusons", lack a well-defined wave vector and polarization [43] as opposed to propagating, wavy, "phonons" in crystalline structures. The peak in damping is most likely a result of the large anharmonicity in the coupling between vibrational modes. To check for correlation between the peak frequency for each glass (as obtained in Figure 5.6) and the corresponding vibrational frequencies, we plot

the peak frequency and the average vibrational frequency in Figure 5.7. Average vibrational frequency is obtained from computing the vibrational density of states from Fourier transform of the velocity autocorrelation function [147]. As seen from the figure, there exists a strong correlation between the two, signifying that damping in the THz regime essentially stems from anharmonic coupling of vibrational modes.

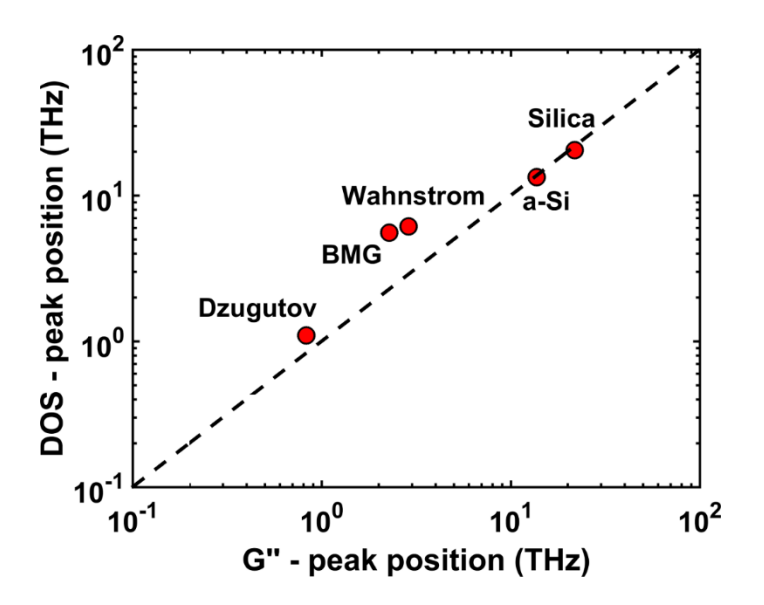


Figure 5.7: Correlation between the average frequency obtained from vibrational Density of states (DOS) for each glass, and the peak position in the frequency-dependent loss modulus as obtained in Figure 5.6.

5.4.2 Low-frequency damping and structural relaxation

We have previously shown in chapter 4 that damping in glasses in the low-frequency regime arises from a collective motion of atoms that contribute to local, irreversible plastic deformation. This mechanism is suppressed at frequencies corresponding to the high-frequency peak (in the THz range of vibrational frequencies) and leads to the persistent damping in the low-frequency regime. The formation of local deformation clusters, the so-called "soft-spots" are typically associated with shear transformation zones and eventual plastic deformation [49], [98]–[100].

Here, we study the evolution of such soft-spots or clusters as function of shear frequency, for all the glasses and the results are shown in Figure 5.8. These simulations are performed under constant temperature (NVT) conditions, where the total time for shear deformation is fixed (compared to constant number of shear cycles as shown in Figure 5.6). The total simulation time is fixed at 50 ns. The criterion for an atom to contribute to a cluster is that it should have a displacement at least equal to shear amplitude and should have at least one other displaced neighbor within a cutoff distance equal to the first shell of nearest neighbors. This cutoff corresponds to the first minimum in the pair correlation function, g(r). We observe that a-Si and silica exhibit negligible cluster formation with this criterion, hence, the displacement amplitude is reduced to half the shear amplitude for these two cases.

Figure 5.8 shows the formation of both average cluster size and percentage of atoms that contribute to the clusters (the irreversibly deformed volume). For all glasses, we observe a decrease in cluster sizes for increasing frequency. Similarly, the volume of cluster atoms (panel b) shows a decreasing trend with increasing frequency. One exception here is the a-Si glass, which shows an increase in cluster volume (at 10 THz), albeit consisting of smaller cluster size compared to lower frequencies. This frequency-dependent cluster formation is, in fact, further accentuated for the case of constant number of cycles (as depicted in Figure 5.6). We argue that the larger amount of time available for nucleation and growth of clusters at lower frequencies leads to a nearly-constant or even slightly increasing damping with decreasing frequency. A similar phenomenon for "viscous flow units" was observed by Wang et. al [19] during cyclic deformation of metallic glasses, albeit at high temperatures required for their activation. This low-frequency damping mechanism is a common feature in all glasses, but the extent of damping depends on the ease of formation of clusters, which in turn depends on the intermolecular forces at the atomic scale. We thus show that oscillatory shear deformation at low frequencies serve as a powerful probe for quantifying the ease of local atomic motion and the associated structural relaxation in glasses.

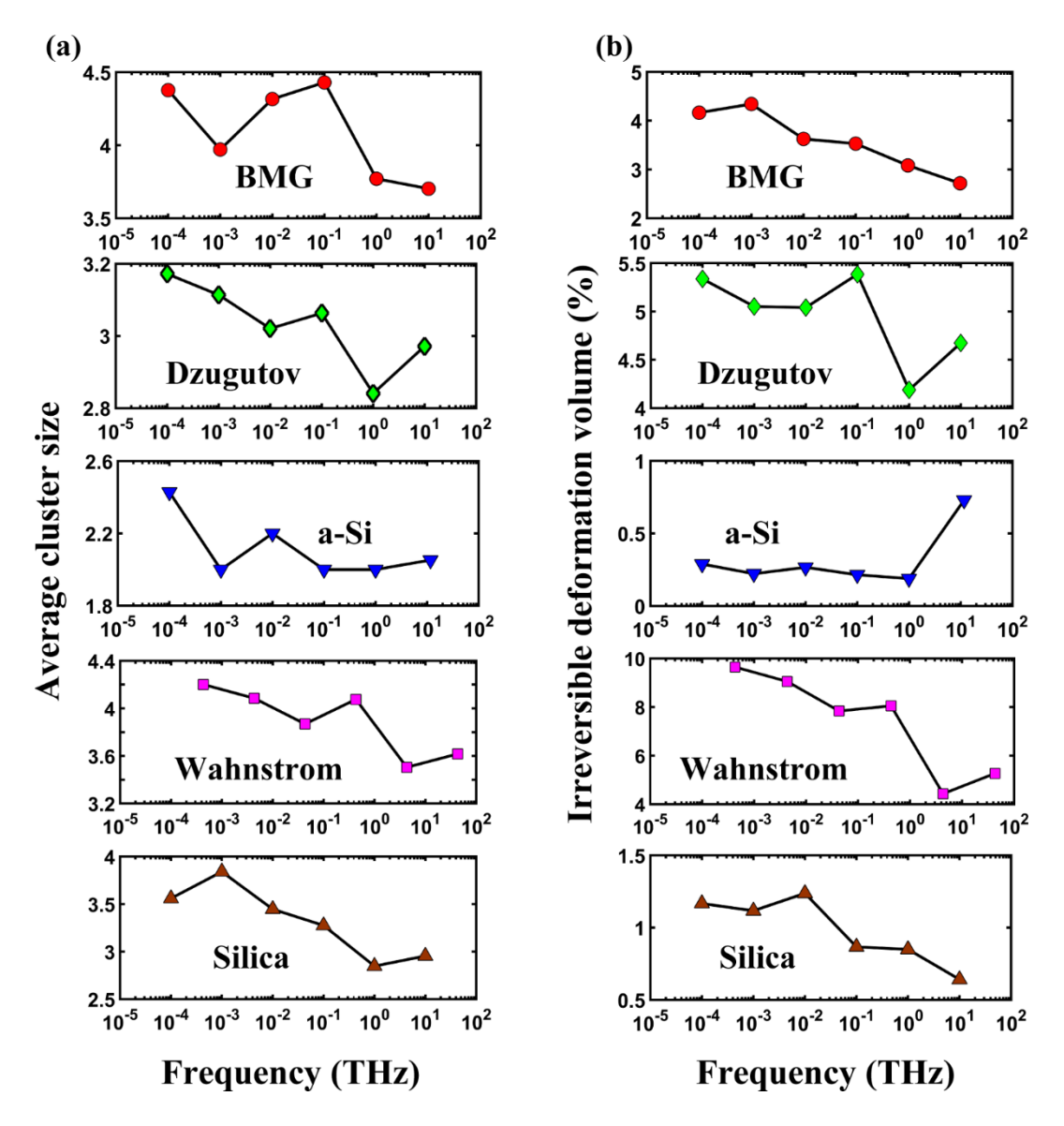


Figure 5.8: Characterization of clusters ("soft spots") formed during constant-time oscillatory shear simulations for various glasses, as a function of shear frequency. The total simulation time at each frequency, for each glass is 50 ns. (a) Average cluster sizes at the end of 50 ns of oscillatory shear. (b) The total volume fraction of irreversibly deformed clusters at the end of shear. The general trend of increasing cluster size and volume with decreasing frequency is evident.

5.5 Summary and Conclusions

Using non-equilibrium molecular dynamics oscillatory shear simulations, we have studied viscoelastic damping extensively in a model Cu-Zr bulk metallic glass (BMG) and show a striking commonality in damping characteristics for various glasses. The two important characteristics in the dependence of damping (as characterized by the loss modulus, G'') on shear frequency are (a) the presence of a well-defined peak in the high-frequency (THz) regime and (b) persistent, nearly-constant damping in the intermediate and low frequency regime. We show that the quench rate plays an important role in damping, especially at low frequencies – larger quench rates (glass at shallower energy minima) lead to a greater degree of local deformation, leading to larger damping. Closely associated with this is the time-dependent loss modulus for glass quenched at large quench rates – faster quenched glass exhibit moduli that vary with the number of shear cycles owing to greater metastability. The two other key factors are shear amplitude and shear temperature – shear amplitudes near and beyond the elastic limit exhibit non-linear viscoelastic response and larger shear temperatures result in larger loss moduli in the low-frequency limit.

We show a clear correlation for the peak frequency (in the THz range) in damping response with the average vibrational frequency of glass, signifying that high-frequency damping stems from the large anharmonicity in coupling of vibrational modes. At intermediate and low frequencies (reaching up to 50 MHz), we show that persistent damping in all glasses is a result of long time-scale local, irreversible deformation. From this study, we demonstrate that oscillatory shear deformation serves as a powerful probe for furthering mechanistic understanding behind damping, and particularly in glasses, to quantifying the degree of local atomic motion and associated stress relaxation at low frequencies.

6. Summary, perspectives and future work

Viscoelastic damping of materials has garnered significant attention over the years, with major implications for a wide range of structural applications. A large body of work has focused on soft matter such as polymers and polymer composites, which are potential materials for large damping, owing to the inherent nature of viscous inter-molecular interactions. Hard materials such as inorganic alloys and glasses have hitherto been relatively unexplored for damping applications due to their predominantly low loss modulus [148]. In this work, we demonstrated exceptional damping in a range of inorganic solids using non-equilibrium molecular dynamics simulations. Novel atomistic mechanisms responsible for damping in a wide range of frequencies have been uncovered for crystalline composites, superlattices, ordered and random alloys, and various glasses. The following sections summarize our key findings, provide relevance of these results for viscoelastic damping applications, and define scope for future work.

6.1 Summary

This thesis has addressed the need for atomic-level simulations to gain mechanistic understanding of viscoelastic damping in hard inorganic solids. We used molecular dynamics oscillatory shear simulations to study viscoelastic damping in three classes of inorganic solids: (a) crystalline composites, (b) ordered and random alloys and (c) glasses. We observed disparate frequency dependence for these structures, over frequencies spanning three to five decades (MHz to THz). In addition to computing the complex shear modulus of materials, we uncovered novel atomistic mechanisms for damping. A detailed overview of the shear deformation methodology was presented in chapter 2.

In chapter 3, we considered high-frequency damping in crystalline composites consisting of a stiff spherical inclusion in a soft matrix. We showed that exceptional damping

Portions of this chapter may appear as: W. Peng, R. Ranganathan, P. Akcora, R. Ozisik and P. Keblinski, "Atomistic mechanisms for stiffening in polymer nanocomposites", unpublished.

(up to 20 times larger than theoretical bounds) could be attained for intermediate volume fractions (ϕ) of the stiff phase (0.2 < ϕ_{stiff} < 0.6). With respect to shear frequency, a characteristic peak in damping is observed at relatively high frequencies (0.3 < f < 1.5 THz).

We showed that this frequency range has a strong overlap with the range of natural vibrational mode frequencies (phonon frequencies). Moreover, mode-dependent Grüneisen parameters that measure the anharmonocity in the coupling of phonon modes were observed to be about 2 to 3 times larger for the composite structure compared to homogeneous phases. High-frequency damping in composites is thus shown to originate from vibrational anharmonicity.

Additionally, damping in these crystalline composites can be tuned by modifying the microstructure, inclusion fraction, and elastic properties (stiffness) of the components. In general, an increase in the inhomogeneity of deformation due to the composite microstructure leads to an enhancement in damping. Characteristics of damping observed for these crystalline composites are also exhibited by superlattice structures comprising soft and stiff crystalline components. We conclude that heterogeneous structures with a large stiffness contrast between the component phases show promise as potential candidates for high-frequency damping applications.

We extended our analysis to structures with a marked difference in their crystallinity; ordered, random, and glassy alloys, in chapter 4. We demonstrated distinct frequency-dependent damping mechanisms for these structures modeled with a binary Lennard-Jones type potential. At high frequencies (of the order of THz), anharmonic coupling between vibrational modes result in large damping in glass and appreciable damping in the random alloy, with a pronounced peak in loss modulus for both structures.

At frequencies below the peak damping frequency, the dependence of the loss modulus with frequency is well-described by a power law. The crystalline structures (ordered and random alloys) show this power law scaling for over 4 decades in frequency. In glass, this scaling is seen to exist only for about 2 decades in frequency, below which, we observe finite, nearly-constant damping for all frequencies.

Persistent damping exhibited by glass is a unique feature arising from local deformation of atomic clusters (soft-spots), over long time scales. We showed that the cluster size and volume fraction show a characteristic frequency-dependence. There appears to

be a threshold frequency below which, soft-spots are activated. We conclude that at high frequencies where anharmonic vibrational coupling is the dominant damping mechanism, cluster formation is naturally suppressed.

The characteristics of damping observed in the binary glass motivated us to probe if this phenomenon is universal for all glasses. With this goal, viscoelasticity in five glass structures (Cu-Zr bulk metallic glass, Dzugutov glass, amorphous silicon, Wahnström glass, and amorphous silica) — modeled with various interaction potentials, were studied in chapter 5. A striking commonality is indeed observed in the frequency-dependent damping — a peak in the high-frequency regime, corresponding to the average vibrational frequency, is exhibited by all glasses. At intermediate and low frequencies, persistent, nearly-invariant damping is exhibited by all glasses, akin to that observed in the glass studied in chapter 4.

A detailed analysis of the factors responsible for damping in the bulk metallic glass system showed that the quench rate for generating glass, shear amplitude, and shear temperature play important roles in damping. Glass quenched with higher quench rates (corresponding to shallower energy minima) lead to larger damping and exhibit moduli that depend on the number of shear cycles. Shear amplitudes near and beyond the elastic limit exhibit a non-linear viscoelastic response. Larger shear temperatures result in larger loss moduli in the low-frequency limit.

We thus conclude that oscillatory shear deformation simulations over shear frequencies spanning several decades serve as a powerful probe to elucidate atomistic mechanisms for damping in hard inorganic materials. Theoretical understanding gained in this work would help design novel materials for high-frequency damping applications.

6.2 Perspectives and future work

The atomistic mechanisms for damping uncovered in this work provide tremendous scope for further analysis, especially in describing the quantitative dependence of damping on various system properties accurately.

Damping at high frequencies (of the order of THz) has been shown to arise from anharmonic coupling of vibrational modes, as corroborated by mode-dependent Grüneisen

parameters. In addition to vibrational anharmonicity, the density of vibrational states should also play an important role in describing damping quantitatively. Further simulations and analysis of the density of states, coupled with the Grüneisen parameters is expected to capture the quantitative dependence.

Recently, Ding et. al [98] have demonstrated that the shear transformation zones responsible for propagation of plastic deformation in glasses have a strong correlation with the quasi-localized low-frequency vibrational modes. These modes, for the Cu-Zr bulk metallic glass was shown to correspond to local polyhedral clusters that have unfavorable coordination and as a result, have low energy barriers for rearrangement under the application of shear. It will be interesting to observe if a similar phenomenon is at play during the oscillatory shear simulations considered in this work.

Viscoelasticity studies have been performed on soft matter for several decades. The oscillatory shear methodology employed in this thesis has a far-reaching potential in its application to study novel microstructures not only in the field of hard materials, but also of soft matter such as polymer melts/blends, networks, and nanocomposites. Molecular-level simulations and models have been employed extensively to study rheology and associated relaxation dynamics [20], [26], [28]–[30], [149], [150], and are ideally suited for capturing atomistic mechanisms responsible for the same.

We have used the shear methodology developed in this thesis to study viscoelasticity in a variety of soft matter such as polymer blends with differing crosslink density, and in silicon nanoparticle-filled phenolic resin nanocomposites. One such study to understand atomistic mechanisms for stiffening in two-phase polymer nanocomposite systems is presented briefly in the following section.

6.2.1 Stiffening in polymer nanocomposites

Recently, Akcora et. al. [151] have observed reversible thermal stiffening in a nano-composite system composed of silica nanoparticles adsorbed with poly(methyl methacrylate) (PMMA) and dispersed in poly(ethylene oxide) (PEO) matrix. Soft materials typically soften upon heating owing to changes in volume; however, this PMMA-PEO-silica nanocomposite remarkably stiffened upon heating. Moreover, this was a reversible

process, with stiffening and softening observed over multiple heating-cooling cycles. The primary reason responsible for this behavior was attributed to the contrast in chain dynamics with temperature. PMMA and PEO have widely different glass transition temperatures (T_g) of 135 °C and -65 °C respectively. At temperatures below T_g of PMMA, i.e., when the PMMA phase is "glassy", there is very little interaction between the adsorbed PMMA chains and the matrix PEO chains. However, at temperatures above the T_g of PMMA, the chains become mobile and couple dynamically with PEO. This enhanced interaction is thought to cause the observed enhancement in the elastic modulus [151].

Motivated by this work, and to verify the role of temperature-dependent interactions in enhancing stiffness in heterogeneous nanocomposites, we proposed a coarse-grained model for describing interactions between the two types of polymer chains (say type "A" describing the low- T_g phase and type "B" corresponding to the high- T_g phase) and the nanoparticle.

Briefly, a spherical nanoparticle in face centered cubic (FCC) crystal structure is modeled via finitely extensible nonlinear elastic (FENE) bonds [152]:

$$U_{FENE} = -\frac{k}{2} R_0^2 ln \left[1 - \left(\frac{r}{R_0} \right)^2 \right]$$
 (6.1)

where, r is the distance between consecutive beads, $R_0 = 1.5\sigma_0$ is the largest length of the FENE bonds, $k = 30\epsilon_0/\sigma_0^2$ is the spring constant. Adjacent beads of the polymer chains have the same bonded interactions as well. Additionally, polymer beads interact via the nonbonded pair-wise Lennard Jones interaction that is cut off and shifted at distances larger than $r = 2.5 \sigma_0$:

$$U_{Shifted LJ} = \begin{cases} 4\varepsilon \left[\left(\frac{\sigma_0}{r} \right)^{12} - \left(\frac{\sigma_0}{r} \right)^6 + 4.08 \times 10^{-3} \right] r < 2.5\sigma_0 \\ r \ge 2.5\sigma_0 \end{cases}$$
 (6.2)

To create the phase with high T_g , we add 3-body angle interactions and 4-body dihedral interactions to every 3 or 4 adjacent beads respectively. This results in the high and low- T_g phases with T_g of approximately 1.4 and 0.4 (in reduced units) respectively, thereby serving as a good surrogate system for the PMMA-PEO system described earlier. Both polymeric phases have a chain length of 50 beads, with the ratio of high to low- T_g phases

being 1:9. We tether the high- T_g phase to the nanoparticle to control the chain configurations precisely.

We create the two distinct configurations that mimic those corresponding to high and low temperatures. The high-temperature configuration corresponds to a "stretched" state, where the high- T_g chains are stretched out and interact with the low- T_g chains. The low-temperature configuration corresponds to a "collapsed" state, where the high- T_g chains have collapsed on the nanoparticle and are essentially frozen. These configurations are created ad-hoc, with increased attraction between high- T_g phase and nanoparticle for the collapsed state and normal interactions for the stretched state. Once the collapsed state is equilibrated for sufficiently long time, we switch all interactions to correspond to those in the stretched state.

We then equilibrate the structures at constant pressure and temperature of T=0.5 (reduced units) and perform oscillatory shear simulations to measure the storage modulus for the two configurations. Figure 6.1 shows the *frequency-sweep* simulation results for stretched and collapsed configurations, and additionally, for the pure low- T_g phase for reference. Also shown in the figure are atomistic snapshots for the two states.

As seen from the figure, the pure low- T_g polymer exhibits the lowest stiffness, owing to fully flexible chains. The collapsed state of the nanocomposite system shows an enhancement in stiffness due to reinforcement from the stiff nanoparticle and the surrounding high- T_g phase. However, a clear indication of even greater reinforcement is observed for the stretched case. This clearly shows that increased interaction between the two phases in the form of entanglements and slowing down of dynamics of the low- T_g phase are indeed responsible for the observed stiffening, confirming the hypothesis proposed for stiffening in the PMMA-PEO-silica nanocomposite.

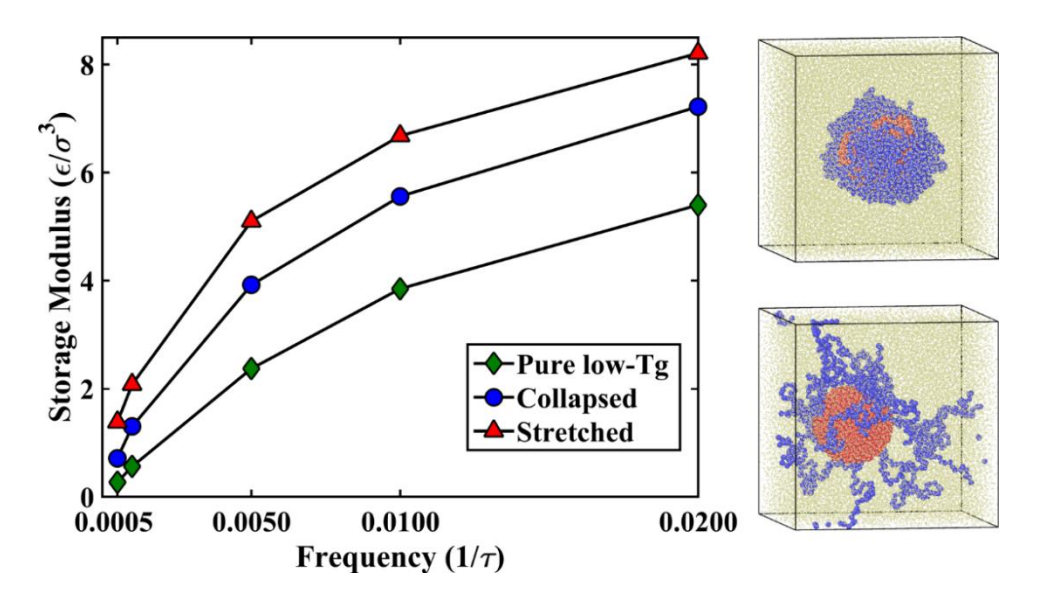


Figure 6.1: Variation of storage modulus with shear frequency for "collapsed" and "stretched" states for the nanocomposite system. Also shown for reference, is the modulus for the pure low- T_g polymer.

Through detailed analyses of several composite systems including hard materials and polymer composites, this thesis has demonstrated the efficacy of molecular-level shear simulations in understanding atomistic mechanisms responsible for viscoelastic damping. Indeed, a variety of novel microstructures and composite systems are yet to explored for engineering viscoelasticity; this thesis has attempted to address this need.

REFERENCES

- [1] I. Newton, *The Principia: Mathematical principles of natural philosophy: A new translation*. University of California Press, 1999.
- [2] E. C. Bingham, Fluidity and plasticity, I. McGraw-Hill Book Company, Inc., 1922.
- [3] H. A. Barnes, J. F. Hutton, and K. Walters, *An introduction to rheology*. Elsevier, 1989.
- [4] M. Doi and S. F. Edwards, *The Theory of Polymer Dynamics*. Oxford University Press, 1986.
- [5] J. D. Ferry, Viscoelastic Properties of Polymers. John Wiley & Sons, 1980.
- [6] M. D. Rao, "Recent applications of viscoelastic damping for noise control in automobiles and commercial airplanes," *J. Sound Vib.*, vol. 262, no. 3, pp. 457–474, 2003.
- [7] B. Samali and K. C. S. Kwok, "Use of viscoelastic dampers in reducing wind- and earthquake-induced motion of building structures," *Eng. Struct.*, vol. 17, no. 9, pp. 639–654, 1995.
- [8] W. Y. Jung and A. J. Aref, "A combined honeycomb and solid viscoelastic material for structural damping applications," *Mech. Mater.*, vol. 35, no. 8, pp. 831–844, 2003.
- [9] P. Katiyar and A. Kumar, "A study of damping characteristics of alumina-filled epoxy nano-composites," vol. 8689, p. 86891M, 2013.
- [10] R. D. Adams and M. R. Maheri, "Damping in advanced polymer-matrix composites," *J. Alloys Compd.*, vol. 355, no. 1–2, pp. 126–130, 2003.
- [11] R. Chandra, S. P. Singh, and K. Gupta, "Damping studies in fiber-reinforced composites a review," *Compos. Struct.*, vol. 46, no. 1, pp. 41–51, 1999.
- [12] R. Schaller, "Metal matrix composites, a smart choice for high damping materials," *J. Alloys Compd.*, vol. 355, no. 1–2, pp. 131–135, 2003.
- [13] Z. Tang, N. A. Kotov, S. Magonov, and B. Ozturk, "Nanostructured artificial nacre.," *Nat. Mater.*, vol. 2, no. 6, pp. 413–418, 2003.
- [14] L. J. Lee, C. Zeng, X. Cao, X. Han, J. Shen, and G. Xu, "Polymer nanocomposite

- foams," Compos. Sci. Technol., vol. 65, no. 15–16 SPEC. ISS., pp. 2344–2363, 2005.
- [15] S. Mitra, S. Cook, V. Svrcek, R. A. Blackley, W. Zhou, J. Kovac, U. Cvelbar, and D. Mariotti, "Improved optoelectronic properties of silicon nanocrystals/polymer nanocomposites by microplasma-induced liquid chemistry," *J. Phys. Chem. C*, vol. 117, no. 44, pp. 23198–23207, 2013.
- [16] R. S. Lakes, Viscoelastic materials. Cambridge University Press, 2009.
- [17] E. Riande, R. Diaz-Calleja, M. G. Prolongo, R. M. Masegosa, and C. Salom, *Polymer viscoelasticity: stress and strain in practice*. Marcel Dekker, New York, 2000.
- [18] R. H. Ewoldt, a. E. Hosoi, and G. H. McKinley, "New measures for characterizing nonlinear viscoelasticity in large amplitude oscillatory shear," *J. Rheol. (N. Y. N. Y).*, vol. 52, no. 6, p. 1427, 2008.
- [19] Z. Wang, P. Wen, L. S. Huo, H. Y. Bai, and W. H. Wang, "Signature of viscous flow units in apparent elastic regime of metallic glasses," *Appl. Phys. Lett.*, vol. 101, no. 12, 2012.
- [20] J. G. Hernández Cifre, S. Hess, and M. Kröger, "Linear viscoelastic behavior of unentangled polymer melts via non-equilibrium molecular dynamics," *Macromol. Theory Simulations*, vol. 13, no. 9, pp. 748–753, 2004.
- [21] K. Kunal and N. R. Aluru, "Akhiezer damping in nanostructures," *Phys. Rev. B Condens. Matter Mater. Phys.*, vol. 84, no. 24, pp. 1–8, 2011.
- [22] P. C. Painter and M. M. Coleman, *Essentials of polymer science and engineering*. DEStech Publications, 2008.
- [23] W. Philippoff, "Vibrational Measurements with Large Amplitudes," *Trans. Soc. Rheol.*, vol. 10, no. 1, pp. 317–334, 1966.
- [24] C. P. Chen, "Apparatus for Determining the Viscoelastic Properties of Materials Over Ten Decades of Frequency and Time," *J. Rheol. (N. Y. N. Y).*, vol. 33, no. 8, p. 1231, 1989.
- [25] R. S. Lakes, J. Quackenbush, E. M. Program, and M. S. Program, "Viscoelastic behaviour in indium tin alloys over a wide range of frequency and time," *Mater. Sci.*, vol. 232, no. 3, pp. 227–232, 1996.

- [26] T. Kairn, P. J. Daivis, I. Ivanov, and S. N. Bhattacharya, "Molecular-dynamics simulation of model polymer nanocomposite rheology and comparison with experiment," *J. Chem. Phys.*, vol. 123, no. 19, 2005.
- [27] K. Hyun, S. H. Kim, K. H. Ahn, and S. J. Lee, "Large amplitude oscillatory shear as a way to classify the complex fluids," *J. Nonnewton. Fluid Mech.*, vol. 107, pp. 51–65, 2002.
- [28] M. Kroger, W. Loose, and S. Hess, "Rheology and structural changes of polymer melts via nonequilibrium molecular dynamics," *J. Rheol. (N. Y. N. Y).*, vol. 37, no. 6, pp. 1057–1079, 1993.
- [29] M. Kröger, "Simple models for complex nonequilibrium fluids," *Phys. Rep.*, vol. 390, no. 6, pp. 453–551, 2004.
- [30] V. S. Volkov and G. V Vinogradov, "Relaxational interactions and viscoelasticity of polymer melts," *J. Nonnewton. Fluid Mech.*, vol. 25, pp. 261–275, 1987.
- [31] R. Lakes, "High damping composite materials: effect of structural hierarchy," *J. Compos. Mater.*, vol. 36, no. 03, pp. 287–297, 2002.
- [32] S. G. Ma, P. K. Liaw, M. C. Gao, J. W. Qiao, Z. H. Wang, and Y. Zhang, "Damping behavior of AlxCoCrFeNi high-entropy alloys by a dynamic mechanical analyzer," *J. Alloys Compd.*, vol. 604, pp. 331–339, 2014.
- [33] S. Muthusamy, S. Wang, and D. D. L. Chung, "Unprecedented vibration damping with high values of loss modulus and loss tangent, exhibited by cement-matrix graphite network composite," *Carbon N. Y.*, vol. 48, no. 5, pp. 1457–1464, 2010.
- [34] N. Srikanth, C. H. Gaofeng, and M. Gupta, "Enhanced damping of a magnesium alloy by addition of copper," *J. Alloys Compd.*, vol. 352, no. 1–2, pp. 106–110, 2003.
- [35] C. S. Wojnar, J.-B. le Graverend, and D. M. Kochmann, "Broadband control of the viscoelasticity of ferroelectrics via domain switching," *Appl. Phys. Lett.*, vol. 105, no. 16, p. 162912, 2014.
- [36] T. Jaglinski, D. Kochmann, D. Stone, and R. S. Lakes, "Composite materials with viscoelastic stiffness greater than diamond.," *Science*, vol. 315, no. 5812, pp. 620–622, 2007.
- [37] R. S. Lakes, "Extreme damping in composite materials with a negative stiffness

- phase," Phys. Rev. Lett., vol. 86, no. 13, pp. 2897–2900, 2001.
- [38] R. S. Lakes, T. Lee, a Bersie, and Y. C. Wang, "Extreme damping in composite materials with negative-stiffness inclusions.," *Nature*, vol. 410, no. 6828, pp. 565–567, 2001.
- [39] Q. Unterreithmeier, T. Faust, and J. P. Kotthaus, "Damping of nanomechanical resonators," *Phys. Rev. Lett.*, vol. 105, no. 7, pp. 1–4, 2010.
- [40] R. Lifshitz and M. L. Roukes, "Thermoelastic damping in micro- and nanomechanical systems," *Phys. Rev. B Condens. Matter Mater. Phys.*, vol. 61, no. 8, pp. 5600–5609, 2000.
- [41] X. Sun, K. Y. Fong, C. Xiong, W. H. P. Pernice, and H. X. Tang, "GHz optomechanical resonators with high mechanical Q factor in air," *Opt. Express*, vol. 19, no. 22, p. 22316, 2011.
- [42] C. Tomaras, B. Schmid, and W. Schirmacher, "Anharmonic elasticity theory for sound attenuation in disordered solids with fluctuating elastic constants," *Phys. Rev. B Condens. Matter Mater. Phys.*, vol. 81, no. 10, pp. 1–5, 2010.
- [43] J. Fabian and P. B. Allen, "Theory of sound attenuation in glasses: The role of thermal vibrations," *Phys. Rev. Lett.*, vol. 82, no. 7, p. 8, 1999.
- [44] H. R. Schober, "Quasi-localized vibrations and phonon damping in glasses," *J. Non. Cryst. Solids*, vol. 357, no. 2, pp. 501–505, 2011.
- [45] K. P. Menard, Dynamic Mechanical Analysis: A Practical Introduction, Second Edition. CRC Press, 2008.
- [46] R. S. Lakes and J. Quackenbusch, "Viscoelastic behavior in indium tin alloys over a wide range of frequency and time," *Philos. Mag. Lett.*, vol. 74, pp. 227–238, 1996.
- [47] M. P. Allen and D. J. Tildesley, *Computer Simulation of Liquids*. Oxford University Press, New York, 1987.
- [48] D. C. Rapaport, *The Art of Molecular Dynamics Simulation*. Cambridge University Press, 2004.
- [49] F. Shimizu, S. Ogata, and J. Li, "Theory of Shear Banding in Metallic Glasses and Molecular Dynamics Calculations," *Mater. Trans.*, vol. 48, no. 11, pp. 2923–2927, 2007.
- [50] A. P. Thompson, S. J. Plimpton, and W. Mattson, "General formulation of pressure

- and stress tensor for arbitrary many-body interaction potentials under periodic boundary conditions," *J. Chem. Phys.*, vol. 131, no. 15, pp. 1–6, 2009.
- [51] S. Plimpton, "Fast Parallel Algorithms for Short-Range Molecular Dynamics," *J. Comput. Phys.*, vol. 117, pp. 1–19, 1995.
- [52] B. Allen and J. L. Feldman, "Thermal conductivity of disordered harmonic solids," *Phys. Rev. B*, vol. 48, no. 17, pp. 581–588, 1993.
- [53] J. L. Feldman, M. D. Kluge, B. Allen, and F. Wooten, "Thermal conductivity and localization in glasses: Numerical study of a model of amorphous silicon," *Phys. Rev. B*, vol. 48, no. 17, pp. 12589 12602, 1993.
- [54] A. Bodapati, P. Schelling, S. Phillpot, and P. Keblinski, "Vibrations and thermal transport in nanocrystalline silicon," *Phys. Rev. B*, vol. 74, no. 24, pp. 1–11, Dec. 2006.
- [55] N. W. Ashcroft and D. N. Mermin, Solid State Physics. 1976.
- [56] S. Shenogin and R. Ozisik, "See http://xenoview.mat.rpi.edu," *See xenoview.mat.rpi.edu*, 2007.
- [57] R. Ranganathan, R. Ozisik, and P. Keblinski, "Viscoelastic damping in crystalline composites: A molecular dynamics study," *Compos. Part B Eng.*, vol. 93, pp. 273–279, 2016.
- [58] B. Benchekchou, M. Coni, H. V. C. Howarth, and R. G. White, "Some aspects of vibration damping improvement in composite materials," *Compos. Part B Eng.*, vol. 8368, no. 29b, pp. 809–817, 1998.
- [59] A. Treviso, B. Van Genechten, D. Mundo, and M. Tournour, "Damping in composite materials: Properties and models," *Compos. Part B Eng.*, vol. 78, pp. 144–152, 2015.
- [60] S. Sharafi and G. Li, "Multiscale Modeling of Vibration Damping Response of Shape Memory Polymer Fibers," *Compos. Part B Eng.*, vol. 91, pp. 306–314, 2016.
- [61] J. Feng and Z. Guo, "Temperature-frequency-dependent mechanical properties model of epoxy resin and its composites," *Compos. Part B Eng.*, vol. 85, pp. 161–169, 2016.
- [62] Z. Hashin and S. Shtrikman, "A variational approach to the theory of the elastic behaviour of multiphase materials," *J. Mech. Phys. Solids*, vol. 11, no. 2, pp. 127–

- 140, 1963.
- [63] Z. Hashin, "Complex moduli of viscoelastic composites—I. General theory and application to particulate composites," *Int. J. Solids Struct.*, vol. 6, no. 5, pp. 539–552, 1970.
- [64] J.-M. Berthelot, M. Assarar, Y. Sefrani, and A. El Mahi, "Damping analysis of composite materials and structures," *Compos. Struct.*, vol. 85, no. 3, pp. 189–204, 2008.
- [65] J. Meaud, T. Sain, G. M. Hulbert, and A. M. Waas, "Analysis and optimal design of layered composites with high stiffness and high damping," *Int. J. Solids Struct.*, vol. 50, no. 9, pp. 1342–1353, 2013.
- [66] H. J. Kim, C. C. Swan, and R. S. Lakes, "Computational studies on high-stiffness, high-damping SiC-InSn particulate reinforced composites," *Int. J. Solids Struct.*, vol. 39, no. 23, pp. 5799–5812, 2002.
- [67] K. Attipou, S. Nezamabadi, E. M. Daya, and H. Zahrouni, "A multiscale approach for the vibration analysis of heterogeneous materials: Application to passive damping," *J. Sound Vib.*, vol. 332, no. 4, pp. 725–739, 2013.
- [68] X. Huang, S. Zhou, G. Sun, G. Li, and Y. M. Xie, "Topology optimization for microstructures of viscoelastic composite materials," *Comput. Methods Appl. Mech. Eng.*, vol. 283, pp. 503–516, 2015.
- [69] J. Hansen and L. Verlet, "Phase transition of the Lennard-Jones system," *Physical Review A*, vol. 184, no. 1. pp. 151–161, 1969.
- [70] S. Nose, "A unified formulation of the constant temperature molecular dynamics methods," *J. Chem. Phys.*, vol. 81, no. 1, pp. 511–519, 1984.
- [71] W. G. Hoover, "Canonical dynamics: Equilibrium phase-space distributions," *Phys. Rev. A*, vol. 31, no. 3, pp. 1695–1697, 1985.
- [72] S. Nose and F. Yonezawa, "Isothermal-isobaric computer simulations of melting and crystallization of a Lennard-Jones system," *J. Chem. Phys.*, vol. 84, no. 3, pp. 1803–1814, 1986.
- [73] E. Gruneisen, *Handbook of Physics*, vol. 10, no. 1. 1926.
- [74] J. Krautkramer and H. Krautkramer, *Ultrasonic Testing of Materials*. 1990.
- [75] N. S. Stoloff and R. G. Davies, "The mechanical properties of ordered alloys,"

- Prog. Mater. Sci., vol. 13, pp. 1–84, Jan. 1968.
- [76] S. A. Skirlo and M. J. Demkowicz, "Viscoelasticity of stepped interfaces," *Appl. Phys. Lett.*, vol. 103, no. 17, p. 171908, 2013.
- [77] N. F. Mott and H. Jones, *The theory of the properties of metals and alloys*, vol. Dover Publ. 1958.
- [78] F. C. Nix and W. Shockley, "Order-disorder transformation in alloys," *Rev. Mod. Phys.*, vol. 10, pp. 1–72, 1938.
- [79] M. F. Ashby and A. L. Greer, "Metallic glasses as structural materials," *Scr. Mater.*, vol. 54, no. 3, pp. 321–326, 2006.
- [80] C. A. Schuh, T. C. Hufnagel, and U. Ramamurty, "Mechanical behavior of amorphous alloys," *Acta Mater.*, vol. 55, no. 12, pp. 4067–4109, 2007.
- [81] W. D. Callister, Fundamentals of Materials Science and Engineering: An Interactive E. Text. 2001.
- [82] H. M. Wyss, K. Miyazaki, J. Mattsson, Z. Hu, D. R. Reichman, and D. A. Weitz, "Strain-Rate Frequency Superposition: A Rheological Probe of Structural Relaxation in Soft Materials," *Phys. Rev. Lett.*, vol. 98, no. 23, p. 238303, 2007.
- [83] W. H. Wang, "The elastic properties, elastic models and elastic perspectives of metallic glasses," *Prog. Mater. Sci.*, vol. 57, no. 3, pp. 487–656, 2012.
- [84] S. S. Iyer and R. N. Candler, "Mode- and Direction-Dependent Mechanical Energy Dissipation in Single-Crystal Resonators due to Anharmonic Phonon-Phonon Scattering," *Phys. Rev. Appl.*, vol. 5, no. 3, p. 034002, 2016.
- [85] A. Akhiezer, "On the absorption of sound in solids," *J. Phys. USSR*, vol. 1, p. 277, 1939.
- [86] M. Hasegawa, S. Yamaura, H. Kato, K. Amiya, N. Nishiyama, and A. Inoue, "Damping properties of hydrogen-absorbed rod metallic glasses," *J. Alloys Compd.*, vol. 355, no. 1–2, pp. 37–41, 2003.
- [87] H.-R. Sinning, "Mechanical Damping by Intercrystalline Diffusion of Hydrogen in Metallic Polycrystals," *Phys. Rev. Lett.*, vol. 85, no. 15, pp. 3201–3204, 2000.
- [88] T. Yagi, T. Imai, R. Tamura, and S. Takeuchi, "Internal friction of hydrogen-doped metallic glasses of high glass forming ability," *Mater. Sci. Eng. A*, vol. 370, no. 1–2, pp. 264–267, 2004.

- [89] S. Steeb and P. Lamparter, "Structure of binary metallic glasses," *J. Non. Cryst. Solids*, vol. 156, pp. 24–33, 1993.
- [90] Y. Shi and M. L. Falk, "Stress-induced structural transformation and shear banding during simulated nanoindentation of a metallic glass," *Acta Mater.*, vol. 55, no. 13, pp. 4317–4324, 2007.
- [91] W. Kob and H. C. Andersen, "Scaling behavior in the β-relaxation regime of a supercooled Lennard-Jones mixture," *Phys. Rev. Lett.*, vol. 73, no. 10, pp. 1376–1379, 1994.
- [92] W. Kob and H. C. Andersen, "Testing mode-coupling theory for a supercooled binary Lennard-Jones mixture. II. Intermediate scattering function and dynamic susceptibility," *Phys. Rev. E*, vol. 52, no. 4, pp. 4134–4153, 1995.
- [93] T. L. Szabo, "Time domain domain wave equations for lossy media obeying a frequency power law," *J. Acoust. Soc. Am.*, vol. 96, no. 1, pp. 491–500, 1994.
- [94] S. P. Näsholm and S. Holm, "Linking multiple relaxation, power-law attenuation, and fractional wave equations.," *J. Acoust. Soc. Am.*, vol. 130, no. 5, pp. 3038–45, 2011.
- [95] T. Pritz, "Frequency power law of material damping," *Appl. Acoust.*, vol. 65, no. 11, pp. 1027–1036, 2004.
- [96] P. He, "Simulation of ultrasound pulse propagation in lossy media obeying a frequency power law," *IEEE Trans. Ultrason. Ferroelectr. Freq. Control*, vol. 45, no. 1, pp. 114–125, 1998.
- [97] R. Rusovici, D. J. Inman, G. A. Lesieutre, M. Ahmadian, H. H. Cudney, H. H. Robertshaw, and W. R. Saunders, "Modeling of Shock Wave Propagation and Attenuation in Viscoelastic Structures," no. April, 1999.
- [98] J. Ding, S. Patinet, M. L. Falk, Y. Cheng, and E. Ma, "Soft spots and their structural signature in a metallic glass," *Proc. Natl. Acad. Sci.*, vol. 111, no. 39, pp. 14052–14056, 2014.
- [99] J. D. Ju, D. Jang, A. Nwankpa, and M. Atzmon, "An atomically quantized hierarchy of shear transformation zones in a metallic glass," *J. Appl. Phys.*, vol. 109, no. 5, 2011.
- [100] Z. D. Sha, S. X. Qu, Z. S. Liu, T. J. Wang, and H. Gao, "Cyclic Deformation in

- Metallic Glasses," Nano Lett., vol. 15, no. 10, pp. 7010–7015, 2015.
- [101] H. Miyagawa and Y. Hiwatari, "Molecular-dynamics study of binary soft-sphere glasses: Quench-rate effects and aging effects," *Phys. Rev. A*, vol. 40, no. 10, pp. 6007–6013, 1989.
- [102] W. Kob and J.-L. Barrat, "Aging Effects in a Lennard-Jones Glass," *Phys. Rev. Lett.*, vol. 78, no. 24, p. 9, 1997.
- [103] A. Stukowski, "Visualization and analysis of atomistic simulation data with OVITO—the Open Visualization Tool," *Model. Simul. Mater. Sci. Eng.*, vol. 18, no. 1, p. 015012, 2009.
- [104] W. Klement, R. H. Willens, and P. Duwez, "Non-crystalline Structure in Solidified Gold–Silicon Alloys," *Nature*, vol. 187, no. 4740, pp. 869–870, 1960.
- [105] M. Telford, "The case for bulk metallic glass," *Mater. Today*, vol. 7, no. 3, pp. 36–43, 2004.
- [106] J. P. K. Doye, D. J. Wales, F. H. M. Zetterling, and M. Dzugutov, "The favored cluster structures of model glass formers," *J. Chem. Phys.*, vol. 118, no. 6, pp. 2792–2799, 2003.
- [107] Y. Q. Cheng, H. W. Sheng, and E. Ma, "Relationship between structure, dynamics, and mechanical properties in metallic glass-forming alloys," *Phys. Rev. B Condens. Matter Mater. Phys.*, vol. 78, no. 1, pp. 1–7, 2008.
- [108] E. Ma, "Tuning order in disorder," Nat. Mater., vol. 14, no. 6, pp. 547–552, 2015.
- [109] D. B. Miracle, "A structural model for metallic glasses," *Nat Mater*, vol. 3, no. 10, pp. 697–702, 2004.
- [110] Y. Q. Cheng and E. Ma, "Atomic-level structure and structure-property relationship in metallic glasses," *Prog. Mater. Sci.*, vol. 56, no. 4, pp. 379–473, 2011.
- [111] K. F. Yao and C. Q. Zhang, "Fe-based bulk metallic glass with high plasticity," *Appl. Phys. Lett.*, vol. 90, no. 6, pp. 2005–2008, 2007.
- [112] H. Ma, J. Xu, and E. Ma, "Mg-based bulk metallic glass composites with plasticity and high strength," *Appl. Phys. Lett.*, vol. 83, no. 14, pp. 2793–2795, 2003.
- [113] J. Schroers and W. L. Johnson, "Ductile bulk metallic glass," *Phys. Rev. Lett.*, vol. 93, no. 25, pp. 20–23, 2004.
- [114] A. Inoue, "High Strength Bulk Amorphous Alloys with Low Critical Cooling

- Rates.PDF," Materials Transactions, JIM, vol. 36, no. 7. pp. 866–875, 1995.
- [115] C. J. Gilbert and R. O. Ritchie, "Fracture toughness and fatigue-crack propagation in a Zr Ti Ni Cu Be bulk metallic glass," *Appl. Phys.*, vol. 71, no. July, pp. 476–478, 1997.
- [116] T. Lee, R. S. Lakes, and A. Lal, "Resonant ultrasound spectroscopy for measurement of mechanical damping: Comparison with broadband viscoelastic spectroscopy," *Rev. Sci. Instrum.*, vol. 71, no. 7, pp. 2855–2861, 2000.
- [117] K. Hyun, M. Wilhelm, C. O. Klein, K. S. Cho, J. G. Nam, K. H. Ahn, S. J. Lee, R. H. Ewoldt, and G. H. McKinley, "A review of nonlinear oscillatory shear tests: Analysis and application of large amplitude oscillatory shear (LAOS)," *Prog. Polym. Sci.*, vol. 36, no. 12, pp. 1697–1753, Dec. 2011.
- [118] M. Lee, Y. Li, Y. Feng, and C. Carter, "Study of frequency dependence modulus of bulk amorphous alloys around the glass transition by dynamic mechanical analysis," *Intermetallics*, vol. 10, no. 11–12, pp. 1061–1064, 2002.
- [119] G. Ruocco and F. Sette, "High-frequency vibrational dynamics in glasses," *J. Phys. Condens. Matter*, vol. 13, no. 41, pp. 9141–9164, 2001.
- [120] D. Heiman, D. S. Hamilton, and R. W. Hellwarth, "Brillouin scattering measurements on optical glasses," *Phys. Rev. B*, vol. 19, no. 12, pp. 6583–6592, 1979.
- [121] J. Kieffer, "Mechanical degradation and viscous dissipation in B2O3," *Phys. Rev. B*, vol. 50, no. 1, pp. 17–29, 1994.
- [122] J. E. Masnik, J. Kieffer, and J. D. Bass, "The complex mechanical modulus as a structural probe: The case of alkali borate liquids and glasses," *J. Chem. Phys.*, vol. 103, no. 23, p. 9907, 1995.
- [123] F. Yuan and L. Huang, "Molecular dynamics simulation of amorphous silica under uniaxial tension: From bulk to nanowire," *J. Non. Cryst. Solids*, vol. 358, no. 24, pp. 3481–3487, 2012.
- [124] Y. Shi, J. Luo, F. Yuan, and L. Huang, "Intrinsic ductility of glassy solids," *Appl. Phys. Lett.*, vol. 104, no. 25, 2014.
- [125] F. Delogu, "Molecular dynamics study of size effects in the compression of metallic glass nanowires," *Phys. Rev. B*, vol. 79, no. December 2008, pp. 1–12, 2009.

- [126] M. Zink, K. Samwer, W. L. Johnson, and S. G. Mayr, "Plastic deformation of metallic glasses: Size of shear transformation zones from molecular dynamics simulations," *Phys. Rev. B Condens. Matter Mater. Phys.*, vol. 73, no. 17, pp. 2–4, 2006.
- [127] Y. Q. Cheng, E. Ma, and H. W. Sheng, "Atomic Level Structure in Multicomponent Bulk Metallic Glass," *Phys. Rev. Lett.*, vol. 102, no. 24, p. 245501, 2009.
- [128] M. Dzugutov, "Glass formation in a simple monoatomic liquid with icosahedral inherent local order," *Phys. Rev. A*, vol. 46, no. 6, pp. 2984–2987, 1992.
- [129] G. Wahnström, "Molecular-dynamics study of a supercooled two-component Lennard-Jones system," *Phys. Rev. A*, vol. 44, no. 6, pp. 3752–3764, 1991.
- [130] F. Albano, N. Lacevic, M. L. Falk, and S. C. Glotzer, "Relating metallic glass mechanical properties to liquid structure," *Mater. Sci. Eng. A*, vol. 375–377, no. 1–2 SPEC. ISS., pp. 671–674, 2004.
- [131] J. Tersoff, "Empirical interatomic potential for silicon with improved elastic properties," *Phys. Rev. B*, vol. 38, no. 14, pp. 9902–9905, 1988.
- [132] Y. Shi and M. L. Falk, "Atomic-scale simulations of strain localization in three-dimensional model amorphous solids," *Phys. Rev. B Condens. Matter Mater. Phys.*, vol. 73, no. 21, pp. 1–10, 2006.
- [133] M. E. Tuckerman, J. Alejandre, R. López-Rendón, A. L. Jochim, and G. J. Martyna, "A Liouville-operator derived measure-preserving integrator for molecular dynamics simulations in the isothermal–isobaric ensemble," *J. Phys. A. Math. Gen.*, vol. 39, no. 19, pp. 5629–5651, 2006.
- [134] M. Parrinello and A. Rahman, "Polymorphic transitions in single crystals: A new molecular dynamics method," *J. Appl. Phys.*, vol. 52, no. 12, pp. 7182–7190, 1981.
- [135] G. J. Martyna, D. J. Tobias, and M. L. Klein, "Constant pressure molecular dynamics algorithms," *J. Chem. Phys.*, vol. 101, no. September, p. 4177, 1994.
- [136] W. Shinoda, M. Shiga, and M. Mikami, "Rapid estimation of elastic constants by molecular dynamics simulation under constant stress," *Phys. Rev. B Condens. Matter Mater. Phys.*, vol. 69, no. 13, pp. 16–18, 2004.
- [137] H. Sheng, J. He, and E. Ma, "Molecular dynamics simulation studies of atomic-level structures in rapidly quenched Ag-Cu nonequilibrium alloys," *Phys. Rev. B*,

- vol. 65, no. 18, pp. 1–10, 2002.
- [138] K. Vollmayr, W. Kob, and K. Binder, "Cooling-rate effects in amorphous silica: A computer-simulation study," *Phys. Rev. B*, vol. 54, no. 22, pp. 15808–15827, 1996.
- [139] S. Munetoh, T. Motooka, K. Moriguchi, and A. Shintani, "Interatomic potential for Si-O systems using Tersoff parameterization," *Comput. Mater. Sci.*, vol. 39, no. 2, pp. 334–339, 2007.
- [140] L. Zhang, Y. Q. Cheng, A. J. Cao, J. Xu, and E. Ma, "Bulk metallic glasses with large plasticity: Composition design from the structural perspective," *Acta Mater.*, vol. 57, no. 4, pp. 1154–1164, 2009.
- [141] J. Tersoff, "Modeling solid-state chemistry: Interatomic potentials for multicomponent systems," *Phys. Rev. B*, vol. 39, no. 8, pp. 5566–5568, 1989.
- [142] B. W. H. van Beest, G. J. Kramer, and R. A. van Santen, "Force Fields for Silicas and Aluminophosphates Based on Ab Initio Calculations," *Phys. Rev. Lett.*, vol. 64, p. 1955, 1990.
- [143] D. Wolf, P. Keblinski, S. R. Phillpot, and J. Eggebrecht, "Exact method for the simulation of Coulombic systems by spherically truncated, pairwise r(-1) summation," *J. Chem. Phys.*, vol. 110, no. 17, pp. 8254–8282, 1999.
- [144] M. Elenius, T. Oppelstrup, and M. Dzugutov, "Evidence for a simple monatomic ideal glass former: The thermodynamic glass transition from a stable liquid phase," *J. Chem. Phys.*, vol. 133, no. 17, 2010.
- [145] O. L. Anderson, "Derivation of Wachtman's equation for the temperature dependence of elastic moduli of oxide compounds," *Phys. Rev.*, vol. 144, no. 2, pp. 553–557, 1966.
- [146] K. Govers, S. Lemehov, M. Hou, and M. Verwerft, "Comparison of interatomic potentials for UO₂. Part II: Molecular dynamics simulations," *J. Nucl. Mater.*, vol. 376, no. 1, pp. 66–77, 2008.
- [147] M. P. Allen and D. J. Tildesley, *Computer Simulation of Liquids*. Clarendon Press, 1987.
- [148] C. P. Chen, R. S. Lakes, E. M. Program, M. S. Program, and J. M. Science, "Analysis of high loss viscoelastic composites Voigt composite," *Most*, no. 1987, 1993.

- [149] S. Sen, S. Sen, S. Kumar, S. Kumar, P. Keblinski, and P. Keblinski, "Viscoelastic Properties of Polymer Melts from Equilibrium Molecular Dynamics Simulations," *Macromolecules*, vol. 38, no. 0, pp. 650–653, 2005.
- [150] M. Vladkov and J. L. Barrat, "Linear and nonlinear viscoelasticity of a model unentangled polymer melt: Molecular dynamics and rouse modes analysis," *Macromol. Theory Simulations*, vol. 15, no. 3, pp. 252–262, 2006.
- [151] E. Senses, A. Isherwood, and P. Akcora, "Reversible Thermal Stiffening in Polymer Nanocomposites.," *ACS Appl. Mater. Interfaces*, vol. 7, no. 27, pp. 14682–14689, 2015.
- [152] K. Kremer and G. S. Grest, "Dynamics of entangled linear polymer melts: A molecular-dynamics simulation," *J. Chem. Phys.*, vol. 1990, no. 8, pp. 5057–5086, 1990.